

Investigation of Fatigue Uncertainty and Correlation to Geometrical Weld Features

OLE S. HERMANSEN & RASMUS SØRENSEN

DESIGN OF MECHANICAL SYSTEMS

AALBORG UNIVERSITY

JUNE 1ST 2023

MASTER'S THESIS





AALBORG UNIVERSITY
STUDENT REPORT

Study Board of Mechanics and Physics

Fibigerstræde 16
DK - 9220 Aalborg Øst
Tlf. 99 40 85 32
snmp@mp.aau.dk
www.mp.aau.dk

Title:

Investigation of Fatigue
Uncertainty and Correlation to
Geometrical Weld Features

Semester:

4th Semester

Semester theme:

Master's Thesis

Project period:

February 2023 - June 2023

ECTS:

30

Supervisor:

Jan Schjødt-Thomsen
Jens Henrik Andreassen

Project group:

Group 4

Participants:

Ole Skjerninge Hermansen
Rasmus Sørensen

Number of pages: 82

Total number of pages: 88

Finished: 01-06-2023

Synopsis:

Current fatigue assessment of welded joints is based on fatigue curves in which several effects known to influence the fatigue strength, such as the weld geometry, residual stresses, and material variations are included. The present work aims to investigate the influence of including the weld geometry, as obtained by laser scanning, on uncertainty in fatigue assessment.

The investigation involves 33 butt welds in S690 and 32 butt welds in S960, subjected to low cycle fatigue. Laser scanning is conducted on each specimen to construct a finite element model incorporating the actual weld geometry. Various fatigue indicators are explored to assess their effectiveness in reducing fatigue uncertainty, combined with a nonlocal model to account for the stress distribution. Using a Weibull distribution based on the weakest-link theory, the performance of the fatigue indicators in reducing uncertainty is evaluated.

The highly stressed volume nonlocal model with maximum principal stress exhibited the lowest uncertainty, with scatter indices of 3.69 for S690 and 3.63 for S960, compared to higher values of 5.11 and 8.42 for the nominal stress approach, respectively. These findings demonstrate the influence of weld geometry on uncertainty in fatigue assessment of butt welded joints.

The study also reveals a relationship between the local stress and weld toe radius, demonstrating an exponential stress-raising effect as the weld toe radius decreases. However, the influence of other geometric weld features on local stress could not be explicitly distinguished due to a lack of clear correlation.

By signing this document, each member of the group confirms participation on equal terms in the process of writing the project. Thus, each member of the group is responsible for all the contents in the project.

Preface

This report serves as the master's thesis for the Design of Mechanical Systems master's programme at Aalborg University. The report is developed by Ole S. Hermansen and Rasmus Sørensen, group 4, during the spring of 2023.

The authors gratefully acknowledge Liftra for their support in providing office space and financial aid in the manufacturing of test specimens. Special thanks is also extended to Ph.D. fellow Anders F. Mikkelsen for valuable discussions and guidance regarding the acquisition and processing of laser scan data.

The numerical procedures presented in this report have been carried out using the following software: MATLAB, ANSYS, SpaceClaim, and MeshLab.

The report uses the Harvard method for references, where sources are specified as (Last name, Year). Tables, figures, and sections are referred to as chapter number followed by the number in the chapter. Equations follow the same numbering system, but are referred to with parentheses.

Abstract

Dette kandidatspeciale er udført som den afsluttende del af kandidatuddannelsen, Design af Mekaniske Systemer ved Det Ingeniør- og Naturvidenskabelige Fakultet på Aalborg Universitet.

Projektet omhandler den statistiske usikkerhed, der observeres når svejste emner udmattelsestestes. Formålet med projektet er at undersøge, om det er muligt at reducere denne usikkerhed ved at inkludere den faktiske svejsegeometri i numeriske modeller. Hertil undersøges en række forskellige udmattelsesindikatorer med henblik på at finde den største reduktion af usikkerhed. Udmattelsesindikatorerne er undersøgt i kombination med både *local* og *nonlocal* modeller, hvortil de *nonlocal* modeller kan medtage spændingsgradienterne nær svejsetåen. Der tages udgangspunkt i *weakest-link* metoden, der understøtter den statistiske tilgang. Metoden tager udgangspunkt i Weibullfordelingen. Derudover ønskes det også undersøgt, om en sammenhæng mellem de svejsegeometriske mål og den resulterende strukturelle respons kan etableres, med henblik på at etablere et sammenhæng mellem geometriske mål og udmattelsesstyrke.

Simuleringer og eksperimentelt arbejde tager udgangspunkt i en række svejste prøveemner fremstillet i henholdsvis stål S690 og S960. Prøveemnerne er fremstillet som stumpsøm. Testemnerne er i forbindelse med forfatterens 3. semester blevet udmattelsestestet og de tilhørende eksperimentelle resultater kendes derved.

Inden udmattelsestesten blev prøveemnernes svejsegeometri målt med laserscanningsteknologi, som danner en 3D punktsky af den scannede svejsning. Gennem en behandlingsproces omdannes de rå punktskyfiler til CAD-modeller, der kan benyttes i det kommercielle program ANSYS til at løse de numeriske modeller. Dette muliggøre anvendelsen af en række forskellige udmattelsesindikatorer til at reducere den statistiske spredning sammenlignet med den nominelle spænding, som i almindelighed anvendes.

Baseret på den numeriske behandling af de eksperimentelle forsøg, konkluderes det at den maksimale hovedspænding med en *highly stressed volume* model giver den største reduktion i statistisk usikkerhed. Metoden opnåede et spredningsindeks på 3.69 for S690 og 3.63 for S960, mens den nominelle spændingstilgang resulterede i højere værdier på henholdsvis 5.11 og 8.42. Disse resultater fremhæver den betydelige indflydelse af svejsegeometrien på usikkerheden i forbindelse med udmattelsesvurdering af stumpsøm.

Sammenhængen mellem udmattelsesstyrke og geometri undersøges ved at iagttage variationen af denne maksimale hovedspænding henover svejsegeometrien på de numeriske simuleringer. Derved kan de geometriske størrelser fra laserscanninen kobles til den strukturelle respons for hvert prøveemne.

Der er fundet en eksponentiel sammenhæng mellem den lokale spænding og dens tilhørende rundingsradius, hvori en mindskende rundingsradius medfører stigning i den lokale spænding. Der kan ikke etableres en relation for de resterende undersøgte geometriske størrelser.

Nomenclature

Abbreviations

εN	Strain-Life
CAD	Computer aided design
COV	Coefficient of variation
FEM	Finite element method
FOV	Field of view
MLE	Maximum likelihood estimation
NURBS	Non-uniform rational B-spline
POI	Point of interest
SN	Stress-Life

Symbols

α	Weld toe angle
$\bar{\sigma}$	Effective stress
\bar{x}	Arithmetic mean
β	Weibull shape parameter
$\Delta\sigma$	Stress range
γ_{max}	Maximum shear strain
κ	Highly-loaded-region exponent, Curvature
λ	Weibull scale parameter
ν	Poisson's ratio
ν'	Effective Poisson's ratio

ω_0	Cutoff frequency
$\sigma_1, \sigma_2, \sigma_3$	Principal stress
σ_{AMP}	Absolute maximum principal stress
σ_{eq}	Equivalent stress
σ_H	Hydrostatic stress
σ_{nom}	Nominal stress
σ'_y	Cyclic yield strength
τ_{max}	Maximum shear stress
θ	Weibull location parameter, Auxiliary angle
$\varepsilon_1, \varepsilon_2, \varepsilon_3$	Principal strain
ε_{AMP}	Absolute maximum principal strain
$\varepsilon_{eq,e}$	Equivalent elastic strain
$\varepsilon_{eq,p}$	Equivalent plastic strain
$\varepsilon_{eq,tot}$	Equivalent total strain
ε_{nom}	Nominal strain
A	Basquin slope
A_0	Reference area
A_{90}	Highly loaded area
B	Basquin intersection
b	Weld width, Roller distance
c	Arc length
E	Young's modulus

F	Force	R_{eL}	Lower yield strength
h	Excess weld height	S_{ut}	Ultimate tensile strength
I	Second moment of area	std	Standard deviation
k	Undercut	T	Tangent vector
K'	Cyclic material strength	t	Thickness
L	Length	T_N	Scatter index
N	Lifetime	V_0	Reference volume
n	Normal vector	V_{90}	Highly loaded volume
n'	Cyclic strain hardening exponent	w	Strain energy density, Width
r	Weld toe radius	x, y, z	Cartesian coordinate
R^2	Coefficient of determination	Y	Lemaitre criterion
R_{eH}	Upper yield strength		

Contents

Preface	v
Abstract	vii
Chapter 1 Introduction	1
1.1 Purpose	1
1.2 Current Contributions	2
1.3 Summary of ' <i>Investigation of Low Cycle Fatigue Lifetime Assessment in Butt Weld of High Strength Steels</i> '	3
Chapter 2 Theoretical Background	5
2.1 Established Methods	5
2.2 Normal Distribution	7
2.3 Weibull Distribution	8
2.4 Measurement of Uncertainty	12
2.5 Fatigue Indicators	15
2.6 Geometrical Weld Features	18
2.7 Problem Statement	21
Chapter 3 Experimental Methods	23
3.1 Specimens	23
3.2 Laser Scanning	24
3.3 Tensile Test	25
3.4 Fatigue	26
Chapter 4 Processing and Construction of Solids	27
4.1 Reverse Engineering Method	27
4.2 Trimming	27
4.3 Repairing Defects	29
4.4 Filtering	30
4.5 Surface Construction	32
4.6 Solid Construction	35
4.7 Compensation of Nominal Differences	36
Chapter 5 Finite Element Modelling of Laser Scans	37

5.1	Boundary Conditions and Setup	37
5.2	Material Model	38
5.3	Local Mesh Convergence Study	39
5.4	Global Mesh Convergence Study	40
5.5	Post-processing of Finite Element Analysis	42
Chapter 6	Results of Uncertainty Study	47
6.1	Baseline	47
6.2	Uncertainty Results of Fatigue Indicators	52
Chapter 7	Discussion of Results	59
7.1	Evaluation of Data Handling Approach	59
7.2	Evaluation of Local and Nonlocal Models	60
7.3	Recommendation for Scatter Reduction	61
Chapter 8	Geometrical Weld Measurements	67
8.1	Determination of Geometrical Features	67
8.2	Distribution of Weld Features	72
Chapter 9	Correlation of Strength and Geometry	75
9.1	Local Variation	75
9.2	Comparison of Local Stress and Geometrical Features	77
Chapter 10	Conclusion	79
Chapter 11	Future Work	81
Bibliography		83

1 Introduction

This project will examine the weld geometry's influence on the fatigue uncertainty for butt welded joints by explicitly incorporating the weld geometry in a finite element analysis and establish what, if any, geometrical measurements influence the uncertainty. The project is an extension of the experimental work conducted by the authors' 9th semester project. This chapter will detail the purpose of this report and present the current contributions that have formed the basis of knowledge. Additionally, the authors' 9th semester project will be summarised to inform the reader of the empirical results which forms the basis of this work.

1.1 Purpose

Current fatigue assessment of welded joints, as presented by Hobbacher (2016), is based on fatigue curves in which several effects known to influence the fatigue strength, such as the weld geometry, residual stresses, and material variations are included. These factors contribute to the significant scatter observed in welded details and introduce a high level of uncertainty compared to machined components. Consequently, any modeling approach relying on such data is also characterised by significant statistical variance, which limits its effectiveness in accurately predicting fatigue life.

With advances in 3D laser scanning technology and computational power, it has become possible to model actual weld geometries. The present work aims to investigate the influence of including the weld geometry, as obtained by laser scanning, on uncertainty in fatigue assessment. The assessment of uncertainty will be conducted for eight different fatigue indicators, and applied to both local and nonlocal models. To account for the uncertainty due to geometrical weld features, a probabilistic model is applied to understand the scatter. An investigation into the effects of the geometrical features and their specific influence on the fatigue indicators is warranted to document any relation between the two. Establishing a potential link will enable the assessment of fatigue performance based on geometrical measurements.

1.2 Current Contributions

Hou (2007) was the first to investigate the effects of weld geometry using a laser scanned model of the real weld geometry and found that the major crack location was correlated with plasticity of the weld toe. Since then, numerous authors have employed the approach of using 3D scanning to obtain models of the local weld geometry.

Schork et al. (2018) established the distribution of weld geometry measurements by laser scanning and their influence on the fatigue strength for different joints. No correlation between the weld toe radius and angle to the crack initiation site was found.

Stenberg et al. (2018) assessed the fatigue life of laser scanned fillet welds of structural and high-strength structural steel, and found that the fatigue performance was not only influenced by the weld geometry parameter but also the difference in material.

Lang and Lener (2016), Niederwanger et al. (2020), and Hultgren et al. (2022) applied the concept of the *weakest-link theory* by Weibull (1951) to further reduce scatter in fatigue results for welded joints.

Lang and Lener (2016) reduced scatter of welded fatigue data when combining the laser scanned geometry with a probabilistic model.

Niederwanger et al. (2020) found that no improvement in fatigue scatter was obtained when considering the local weld geometry in comparison to an idealised weld geometry for linear elastically loaded welded cruciform joints.

Hultgren et al. (2022) found a reduction in the variation of fatigue scatter when modelling the local geometry and established that the local stress at the weld toe is highly influenced by the surrounding geometry.

Both Niederwanger et al. (2020) and Hultgren et al. (2022) also applied the concept of a highly stressed region to include the effects of the stress gradients at the weld toe.

Stenberg et al. (2012) studied the available methods of evaluating the geometrical features of a weld and determined the sensitive nature of the manual processes. An algorithm for obtaining the geometrical measurements based on laser scanning was proposed and studied for T-joints.

Schubnell et al. (2019) presents a round-robin study of different digital methods for computing the weld toe radius and weld toe angle for both T- and butt joints based on laser scan data. Both manual and algorithmic methods were investigated, and a fully automated algorithm is proposed.

Renken et al. (2021) presents an algorithm for obtaining the weld toe radius and performs a statistical evaluation of each weld feature for a fillet weld. Recommendations for the resolution of the laser scanning setup is also provided.

1.3 Summary of 'Investigation of Low Cycle Fatigue Lifetime Assessment in Butt Weld of High Strength Steels'

This project is an extension of the experimental work conducted by the authors' 9th semester project. The purpose of the project was to investigate if butt welded joints of different high strength steels, structural steels S690 and S960, would have a similar fatigue strength in low cycle fatigue.

The experimental work consisted of monotonic tensile testing of the base material, laser scanning of each welded specimen, and stress-based fully reversed fatigue testing in a four-point bending fixture. A total of 33 specimens of S690 and 32 specimens of S960 were subject to fatigue testing, producing the SN curve shown in Figure 1.1.

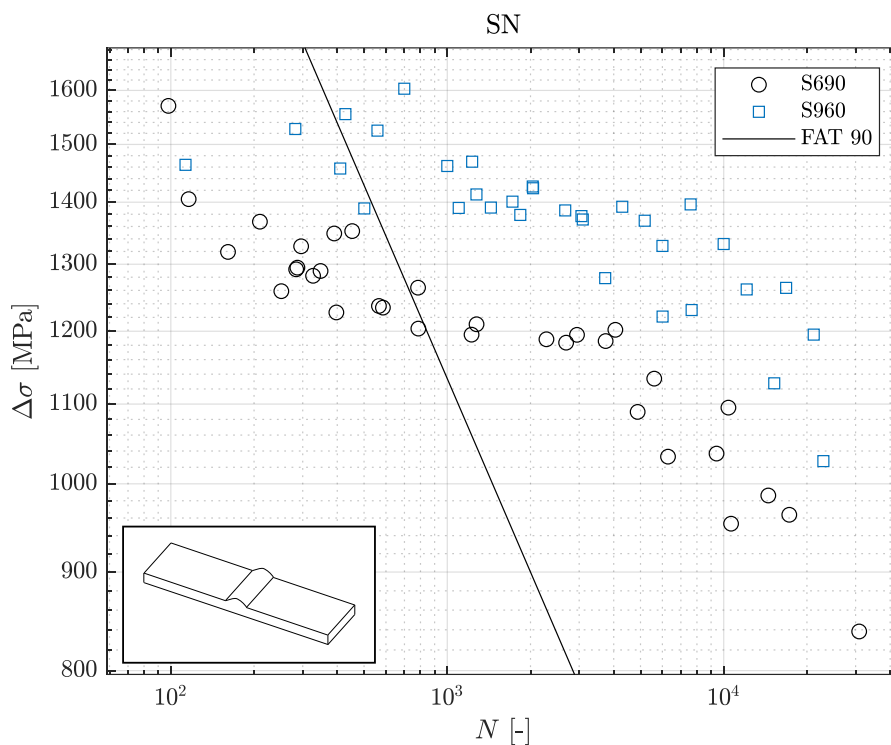


Figure 1.1. SN curve for the nominal stress range for S690 and S960 based on the experimental work by Hermansen and Sørensen (2022) and an appropriate selected FAT curve for butt welds. (The cyclic material model and method for calculating the nominal stress range is described in Chapter 5)

As seen in Figure 1.1, a distinct separation of the data is reported. The specimens manufactured in S960 generally exhibit a greater fatigue strength compared to that of the S690. Additionally, the slopes of both data sets display a greater slope in comparison to the slope of $m = 3$ for FAT curves. Both of these points are inconsistent with Hobbacher (2016, Ch. 3.2).

2 Theoretical Background

This chapter will serve as a baseline for the methods and theory applied. Section 2.1 examines the background for fatigue assessment based on FAT curves. An introduction to the principle of the weakest-link method is also given. Section 2.2 detail the normal distribution and its properties when applied to fatigue data. Section 2.3 details the Weibull distribution and its properties in conjunction with its implementation in fatigue modeling. Section 2.4 presents the methods for measuring the uncertainty of fatigue. This is used as a measure of the quality of the fatigue indicator. Section 2.5 introduces relevant fatigue indicators that are to be used to predict fatigue failure. The fatigue factors are either stress-, strain-, or energy-based. Section 2.6 presents the geometrical features of a weld and methods for evaluating said features.

2.1 Established Methods

Methods for assessing high cycle fatigue life of welded joints are well established. Three commonly used methods are the nominal, hot-spot, and effective notch stress methods. The nominal approach assumes a nominal geometry of the specimen and calculates nominal stresses analytically. The hot-spot methods uses the principles of the nominal approach, but applied for a finite element model, and establishes the nominal stress components by stress linearization (Niemi, 2003, Ch. 1.1). This method allows for the modelling of an idealised weld geometry. The effective notch stress methods models an idealised weld geometry, including the weld toe radius, and computes the maximum stress at the weld toe (Fricke and Maddox, 2008, Ch. 3.3). (Hobbacher, 2016, Ch. 2.2)

Common for all three methods, is the evaluation of fatigue life based on the relevant FAT curve (Hobbacher, 2016, Ch. 3.2-3.4). FAT curves are established based on experimental data of welded components where the fatigue strength is calculated based on a nominal approach (ECCS, 2018) (Hobbacher, 2016, Ch. 3.2). These FAT curves are obtained for high cycle fatigue. However, DNVGL-RP-C203 (2016, F.1) states that in the case of low cycle fatigue $N < 10000$, the FAT curves "*may be linearly extrapolated to fewer cycles*". DNVGL-RP-C203 (2016) is applicable for offshore steel structures, but the principle of extrapolation is used in the following. Thus, FAT curves are applied for welded components in low cycle fatigue applications. As such, the underlying basis for the FAT curves will be detailed for the commonly applied methods.

Several effects are known to influence the fatigue strength of welded joints. These effects include the material variation, weld geometry, and residual stresses (Hobbacher, 2016, Ch. 3.2) (Stephens et al., 2001, Ch. 13). All effects are included in the construction of the FAT curve (Hobbacher, 2016, Ch. 3.2). This will inherently introduce a large degree of scatter in the experimental data.

When fitting empirical data for the construction of FAT curves, two fundamental assumptions are made. Firstly, the data in a $\log_{10}(N)$ vs $\log_{10}(S)$ (SN) is assumed to follow a linear $\log_{10} - \log_{10}$ relation as given by Equation (2.1), also known as the Basquin equation. Secondly, a normal distribution, with input $\log_{10}(N)$, is assumed. The corresponding confidence interval for the fatigue strength is evaluated at $N = 2 \times 10^6$ under the assumption that the distribution is independent of applied stress range as illustrated in Figure 2.1. (ECCS, 2018, Ch. 5.2)

$$\log_{10}(N) = A \log_{10}(S) + B \quad (2.1)$$

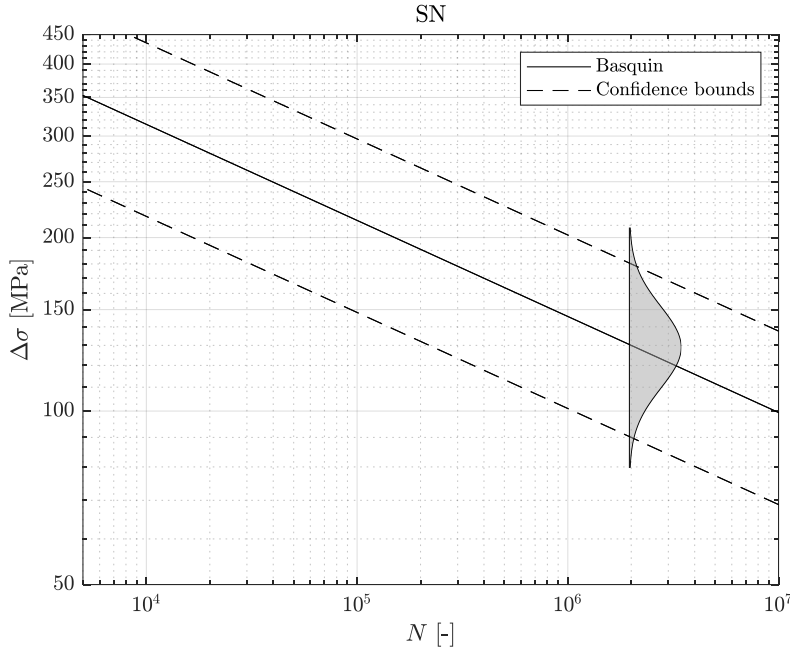


Figure 2.1. Illustrative FAT 90 curve and normal distribution for the fatigue strength.

Using these assumptions, the basis for stress-based fatigue evaluation is formed. However, there may be drawbacks in this approach. Firstly, when observing empirical results, the stress level influences the scatter. At high stress levels the scatter is lower whereas for lower stress levels the scatter increases (Stephens et al., 2001, Sec. 13.2.1).

Secondly, weld fatigue data does not necessarily have to follow a normal distribution. The resulting fatigue strength distribution is a product of the distribution of the different effects which influence the fatigue strength. As such, it would be fair to assume the fatigue strength distribution approaches a normal distribution based on the concepts of the central

limit theorem (O'Connor and Kleyner, 2012, Ch. 2.6.1). However, such a distribution has its limits, primarily in its inherent symmetry.

In the work by Weibull (1951) the concept of *weakest-link theory* was first introduced. This theory is based on the concept that the single weakest link in a chain, will cause failure of the entire chain. Analogous to this, the idea of failure sites in welded joints is introduced. The number of failure sites increases with increasing load and failure happens when the weakest site reaches a critical value. In the implementation, the failure sites are assumed to be mutually independent. In his work, Weibull (1951) demonstrated the applicability of the Weibull distribution for the fatigue life of a steel component. Similar to Niederwanger et al. (2020); Hultgren et al. (2022), this work will apply the Weibull distribution for the fatigue data.

Normal or Weibull Distribution

It is crucial to acknowledge that the process of choosing the *correct* distribution is no trivial task. It should be recognised that empirical data may not conform to any theoretical distribution. This work will not consider what distribution is the appropriate to select for the underlying data, but instead only consider the result of applying the aforementioned normal and Weibull distributions.

2.2 Normal Distribution

The probability density function of a normal distribution is given by Equation (2.2). (O'Connor and Kleyner, 2012, Ch. 2.6.1)

$$f(x) = \frac{1}{\sigma (2\pi)^{1/2}} e^{\left(-\frac{1}{2} \left(\frac{x-\mu}{\sigma}\right)^2\right)} \quad \text{for } -\infty < x < \infty \quad (2.2)$$

A normal distribution consists of two parameter: (O'Connor and Kleyner, 2012, Ch. 2.6.1)

σ = Scale parameter, equal to the standard deviation.

μ = Location parameter, defines the mean.

The normal distribution is a symmetrical distribution centered about its mean value. The distribution is thus not able to capture any non-symmetrical data, such as skewed or heavy tailed data. (O'Connor and Kleyner, 2012, Ch. 2.6.1)

When applied to fatigue data, the limits of the input x is nonphysical in the case of fatigue strength or life due to its negative lower bound. The input considered, is thus evaluated using \log_{10} first, such as $x = \log_{10}(N)$. This results in limits of $0 \leq \log_{10}(N) < \infty$ for fatigue life. (ECCS, 2018, Ch. 5)

2.3 Weibull Distribution

The Weibull probability density function is given by Equation (2.3) and the cumulative density function is given by Equation (2.4) (Weibull, 1951).

$$f(x) = \frac{\beta}{\lambda} \left(\frac{x - \theta}{\lambda} \right)^{\beta-1} e^{-\left(\frac{x - \theta}{\lambda} \right)^\beta} \quad \text{for } x \geq 0 \quad (2.3)$$

$$F(x) = 1 - e^{-\left(\frac{x - \theta}{\lambda} \right)^\beta} \quad \text{for } x \geq 0 \quad (2.4)$$

Equations (2.3) and (2.4) consists of three parameter, hence the name *three parameter Weibull distribution*, where: (O'Connor and Kleyner, 2012, Ch. 3.4)

β = Shape parameter (Weibull slope or modulus), slope of the failure line on a Weibull probability plot.

λ = Scale parameter (characteristic life or strength), is the value at which 63.2% of specimens will fail.

θ = Location parameter (expected minimum life or strength), defines the start location of Equations (2.3) and (2.4).

The Weibull distribution has the added benefit of being able to represent different data distributions as shown in Figure 2.2. (O'Connor and Kleyner, 2012, Ch. 2.6.6) (Rinne, 2009, Ch. 3.2)

- $\beta = 1$, becomes an exponential distribution.
- $\beta = 2, \lambda = 1$, becomes a Rayleigh distribution.
- $\beta = 3.5$, approximates a normal distribution.

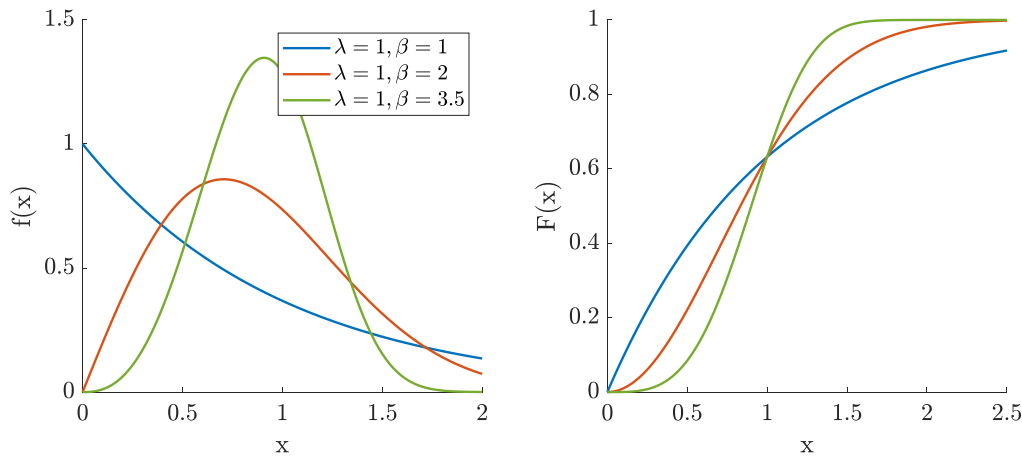


Figure 2.2. Weibull distribution representing other distributions.

Fatigue Strength vs Fatigue Life

The physical interpretation of λ and θ are depended on the input of x (O'Connor and Kleyner, 2012, Ch. 3.4). In the case of fatigue strength, both parameters are related to

the strength of the specimens. θ will thus provide an endurance limit for the strength, i.e. no fatigue failure below θ .

A similar interpretation can be established for fatigue life, where applied cycles below θ would not cause failure. However, a fatigue data set with no run-outs using a three parameter Weibull, is able to obtain a θ greater than the lowest measured fatigue strength/life, thus becoming nonphysical. This limits the distribution to a *two parameter Weibull distribution*, i.e. $\theta = 0$ in Equations (2.3) and (2.4). In the remainder of this work, a fatigue life approach is applied, thus the input x is lifetime $\log_{10}(N)$.

2.3.1 Determination of Fatigue-Life Distribution

In order to collectively examine the fatigue-life distribution of fatigue tests conducted at several different stress levels, the data must be converted to a common stress level (Weibull, 1961, Ch. 9.2-9.3). This is obtained through the connecting link of stress and lifetime - the assumed SN model. Several model exists for modelling the SN curve (Caiza and Ummenhofer, 2011), however, in this work the Basquin equation, presented in Equation (2.1), will be considered.

By fitting the Basquin equation and obtaining the slope, the observed data can be *collapsed* to a common fatigue strength as illustrated in Figure 2.3. In the case of a common fatigue strength, no consensus is known to the authors¹. Niederwanger et al. (2020) considers the median stress value while Li et al. (2018) considers the maximum stress value. The value of the common fatigue strength will influences the resulting Weibull distribution. A median value is chosen as it deemed most representative of the data set as it is insensitive to extreme values.

It should be noted that the assumption of collapsing the data to a shared fatigue strength, is necessary due to the single input x for the probability distribution function. However, as shown by Sinclair and Dolan (1953), the distribution for components subjected to fatigue is not independent of the applied stress. In such cases, a distribution which inputs both the strength and lifetime is required. However, such distribution is not be considered in this work.

2.3.2 Weibull Parameter Estimation

The two most common techniques for obtaining the Weibull parameters are rank regression (least squares) and Maximum Likelihood Estimation (MLE). Applying both methods will not necessarily produce the same results. O'Connor and Kleyner (2012, Ch. 3.5) recommends the use of MLE for large data sets and when data is censored, while recommending the least squares approach for smaller data set (less than 30). In this work, a least squares approach is applied as the result of the fit can be measured through the goodness-of-fit.

¹In the case of a common fatigue life, a lifetime of $N = 2 \times 10^6$ as mentioned in Section 2.1 should be selected as illustrated by Hultgren et al. (2022).

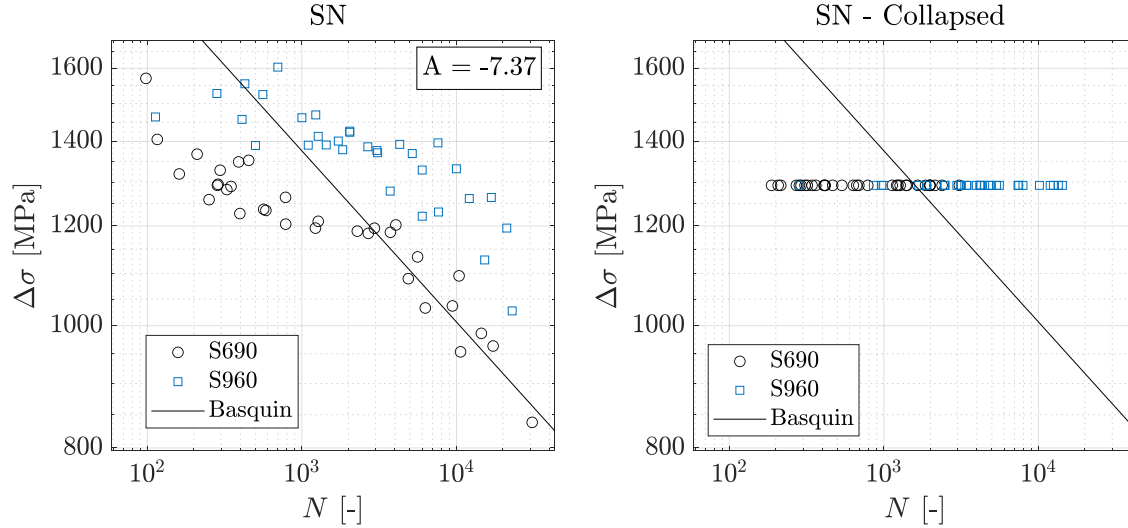


Figure 2.3. SN curve with Basquin fit and data collapsed at median strength for a nominal stress approach.

To apply the least squares approach, the cumulative distribution is to be rewritten to a linear space. Equation (2.4) can be rewritten to Equation (2.5).

$$\frac{1}{1 - F(x)} = e^{\left(\frac{x - \theta}{\lambda}\right)^\beta} \quad (2.5)$$

By taking twice the natural logarithm of Equation (2.5), the equation becomes Equation (2.6).

$$\ln\left(\ln\left(\frac{1}{1 - F(x)}\right)\right) = \beta \ln(x - \theta) - \beta \ln(\lambda) \quad (2.6)$$

Equation (2.6) has the linear form $y = \beta x + b$, where

$$\begin{aligned} x &= \ln(x - \theta) \\ y &= \ln\left(\ln\left(\frac{1}{1 - F(x)}\right)\right) = \ln\left(\ln(S(x)^{-1})\right) \\ b &= -\beta \ln(\lambda) \end{aligned}$$

In order to solve the system, an estimator for the survival rate $S(x) = 1 - F(x)$ is needed. The Kaplan-Meier estimator is chosen due to its popularity and is calculated based on Equation (2.7), where n is the total number of data points, and i is the current evaluated failure point. (Rinne, 2009, Ch. 9.3.2.1)

$$S_i = \frac{n - i}{n - i + 1} S_{i-1}, \quad S_0 = 1, \quad \text{for } i = 1..n \quad (2.7)$$

By minimising the least squares, as shown by Equation (2.8), of Equation (2.6), the parameters for the Weibull distribution are obtained.

$$\min \sum_{i=1}^n (y_i - y(x_i))^2 \quad (2.8)$$

Figure 2.4 shows the result of a fitting procedure described for the data shown in Figure 2.3.

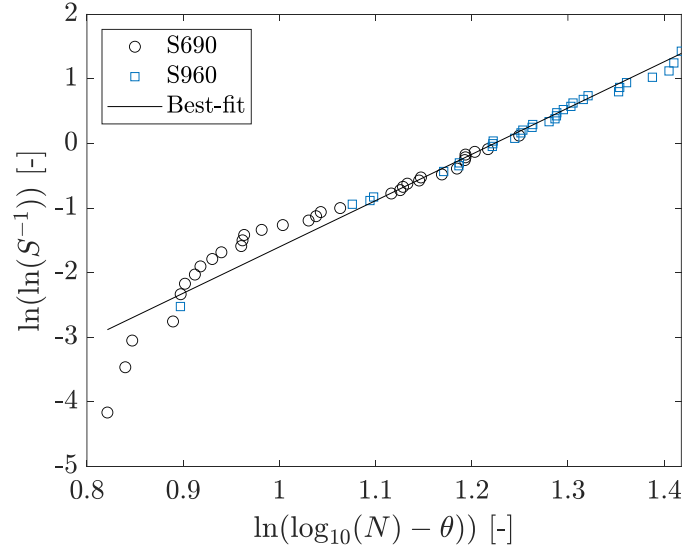


Figure 2.4. Linear fit for obtaining the Weibull parameters for the nominal stress.

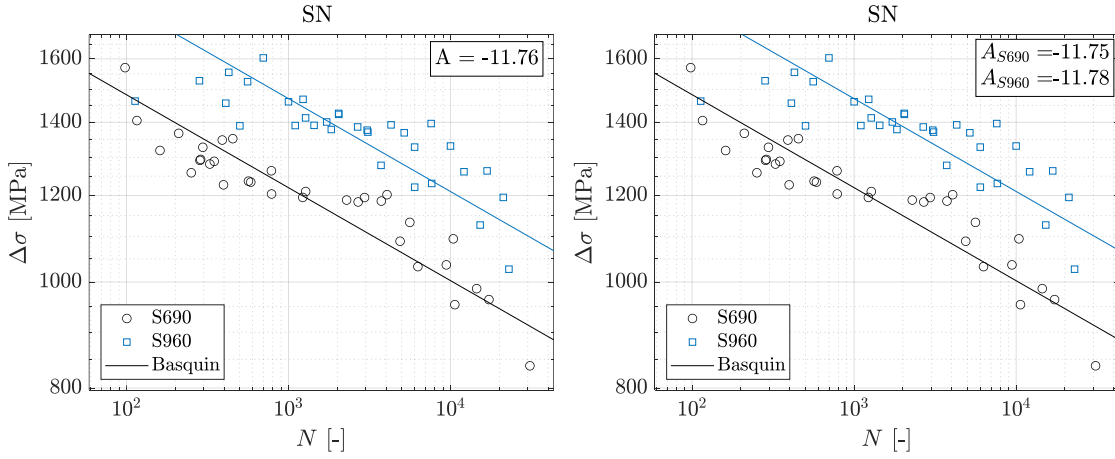
2.3.3 Failure Probability for Two Data Sets

When designing welded joints, based on Hobbacher (2016, Ch. 3.2), no distinction is made for the tensile strength of the base material. Following this approach, the two data sets, fatigue life for S690 and S960, should be considered as a combined data set as shown in Figure 2.3, i.e. resulting in a single set of Basquin and Weibull parameters.

However, as shown in Figure 1.1, a clear distinction between S690 and S960 is apparent for the nominal stress approach. This figure suggests an offset between the two data sets such that the difference in material is included in the model. Based on this, another approach is defined wherein the data sets for S690 and S960 are treated separately, however they are forced to share an identical Basquin slope A in the \log_{10} - \log_{10} system, and also share an identical Weibull slope β as presented in Li et al. (2018). This corresponds to a shift in FAT class as prescribed in Hobbacher (2016). This is shown in Figure 2.5a where the Basquin fit for both S690 and S960 have an identical slope, but different intersections B .

Lastly, it is logical to consider the data sets of S690 and S960 as completely separate sets, sharing no identical properties. This allows the difference in material to be explicitly modelled. This approach should yield the best possible fit for each data set as no restrictions are imposed. In Figure 2.5b the two data sets are complete separate, thus a unique A and B value for each data set.

By comparing the slope of Figures 2.3 and 2.5, it would suggest for the nominal stress approach, that the two data sets should have an identical slope but different intersections. Similarly, this can be extended for the distribution of the given data set, allowing for distribution with identical slope β or unique slopes. How the data is handled, and which approach is most applicable, depends on the fatigue indicator being investigated. Figure 2.6 illustrates the different combination considered for the two data sets.



(a) Identical Basquin slope. (b) Completely separate Basquin slopes.

Figure 2.5. Basquin fit with different data handling approaches.

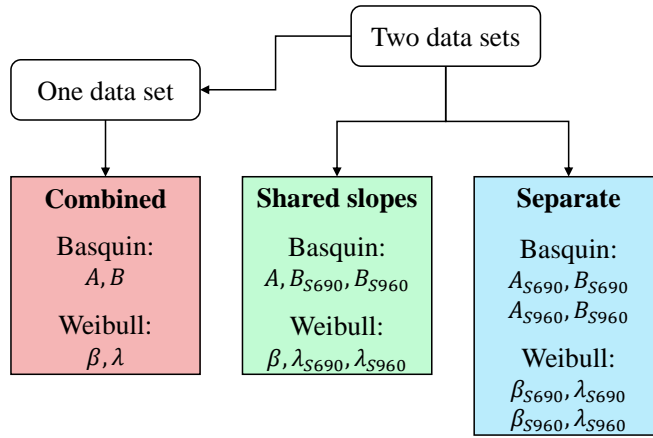


Figure 2.6. Approach for data set handling and the resulting Basquin and Weibull parameters.

2.4 Measurement of Uncertainty

In order to evaluate whether the uncertainty of a given fatigue indicator reduces the uncertainty, compared to the nominal approach, the fatigue indicator’s correlative capability is examined through a set of measurements. In this work, this is established by its scatter index, standard deviation, coefficient of determination for the Basquin fit, and the Weibull slope.

Scatter Index

The scatter index T_N , or scatter range index, is defined as the ratio of the 10-90% quantiles. The life time value at 10% and 90% quantiles are obtained by evaluating the cumulative distribution considered as illustrated in Figure 2.7 and Equation (2.9). Thus, it is a measure of dispersion of the data.

$$T_N = \frac{T_{N,90\%}}{T_{N,10\%}} \tag{2.9}$$

The quantiles at which the scatter index is evaluated are naturally influenced by the shape of the distribution. If a heavy-tailed Weibull distribution, such as the case of $\beta = 1$ in Figure 2.2 is considered, the resulting scatter index becomes sensitive to small changes in β . No standard values for the quantiles are known to the authors. Lang and Lener (2016) applies a 5-95% quantile range, while Niederwanger et al. (2020) applies a 10-90% quantile range. In this work, the evaluation of the scatter index is limited to a 10-90% quantile range.

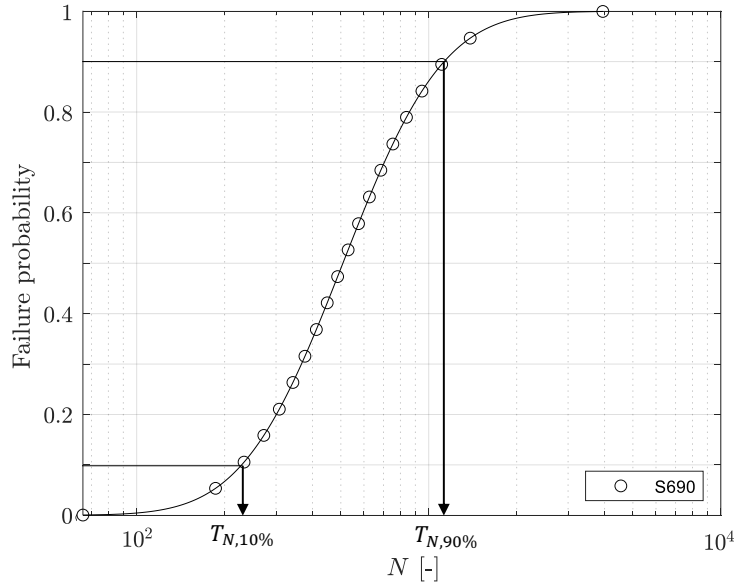


Figure 2.7. Evaluation of scatter index for a normal distribution.

Standard Deviation

Similar to the scatter index, the standard deviation *std* is also a measure of the data's dispersion. Numerically, it can be obtained by solving the cumulative distribution function n number of times equidistantly distributed in the interval 0 to 1 and obtaining the corresponding life time N_i (Niederwanger et al., 2020). The standard deviation is then calculated by Equation (2.10)² (Stephens et al., 2001, Ch. 13.1).

$$std = \sqrt{\frac{1}{n-1} \sum_{i=1}^n |N_i - \bar{N}|^2} \quad (2.10)$$

When each data set obtains a unique distribution, refer to Figure 2.6, a shifted standard distribution can be obtained by shifting the N_i vector to a common mean value for each data set (Niederwanger et al., 2020). Figure 2.8 illustrates the numerical evaluation for obtaining N_i and shifting the standard deviation of each data set to a common mean value.

²The equation has converged for $n = 1000$.

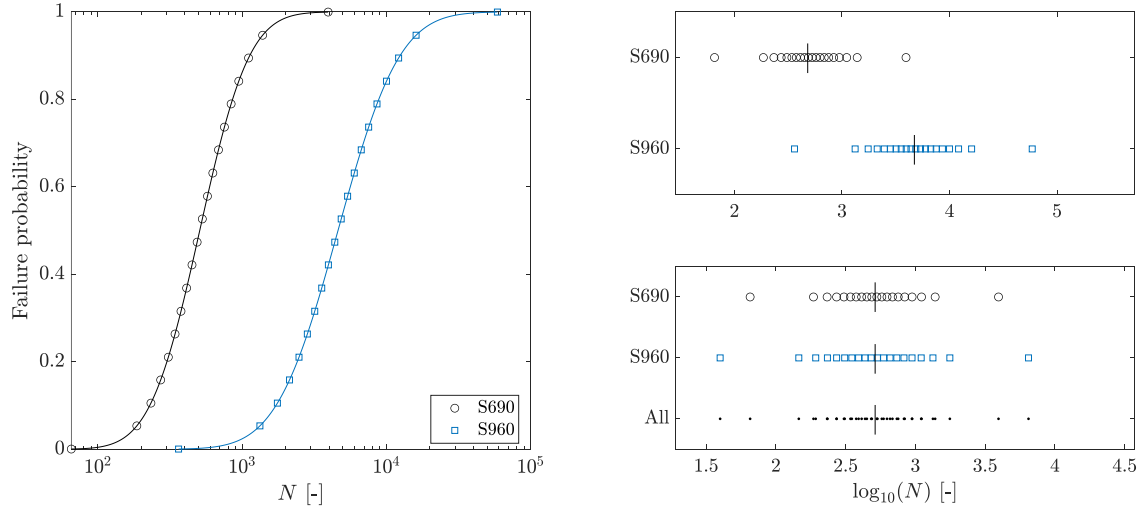


Figure 2.8. Illustrative demonstration of the numerical calculation of the standard deviation for $n = 20$.

Coefficient of Determination

The coefficient of determination R^2 is a measure of the variation for a regression model f_i and its corresponding data y_i . Its value varies between 0 and 1, where a value of 1 indicates that the model explains the data, thus no variation. The R^2 is calculated by Equation (2.11). (Ross, 2004, Ch. 9.5)

$$R^2 = 1 - \frac{SS_R}{S_{YY}} \quad (2.11)$$

Where:

$$SS_R = \sum_{i=1}^n (y_i - f_i)^2$$

$$S_{YY} = \sum_{i=1}^n (y_i - \bar{y}_i)^2$$

The R^2 is calculated for the Basquin equation shown in Equation (2.1) and the Weibull distribution in a linear space Equation (2.6). The R^2 for the Basquin fit is thus also a measure of the uncertainty, while the R^2 for the Weibull fit is a measure of the goodness-of-fit for the distribution itself.

Weibull Slope

When evaluating the Weibull distribution in a linear space, as shown by Equation (2.6), it becomes apparent that Weibull slope β is a measure of the scatter of the data. If the scatter is the large, the subsequent Weibull slope will be small, or if the scatter is small, the Weibull slope is large. The Weibull slope is thus also a measure of the uncertainty of the data. (Wallin, 1984)

2.5 Fatigue Indicators

Several different fatigue indicators will be considered for examining their performance for reducing uncertainty compared to the nominal approach. These fatigue indicators are a mix of more-or-less well known predictors for modelling the fatigue phenomenon. Stress-, strain-, and energy-based criteria are investigated.

Equivalent Stress

Equivalent stress σ_{eq} is a well established failure criteria for mild steel. The criteria is calculated by Equation (2.12) based on the three principal stresses σ_1, σ_2 , and σ_3 . (Stephens et al., 2001, Ch. 10.3.1)

$$\sigma_{eq} = \sqrt{\frac{1}{2} \left((\sigma_1 - \sigma_2)^2 + (\sigma_2 - \sigma_3)^2 + (\sigma_3 - \sigma_1)^2 \right)} \quad (2.12)$$

Maximum Principal Stress

The maximum principal stress criteria is found to work better for steel with a more brittle behaviour. The criteria can be expanded using the absolute maximum principal stress σ_{AMP} which is evaluated by Equation (2.13). (Stephens et al., 2001, Ch. 10.3.1)

$$\sigma_{AMP} = \max(|\sigma_1|, |\sigma_2|, |\sigma_3|) \quad (2.13)$$

Maximum Shear Stress

A more conservative criteria than the equivalent and principal stress approach, is the maximum shear stress τ_{max} . The maximum shear is evaluated by the principal stresses as given in Equation (2.14). (Stephens et al., 2001, Ch. 10.3.1)

$$\tau_{max} = \frac{\sigma_1 - \sigma_3}{2} \quad (2.14)$$

Total Equivalent Strain

Analogous to the three presented stress approaches, similar strain methods can be deployed. The total equivalent strain $\varepsilon_{eq,tot}$ to be calculated on the three principal strains $\varepsilon_1, \varepsilon_2$ and ε_3 . The method used for calculating the total equivalent strain is given by ANSYS (2023a, p. 2096-2097) and differs from the methods presented in Stephens et al. (2001, Ch. 10.4.1) as it separates the equivalent strain into an elastic and plastic component as shown in Equations (2.15) and (2.16). For the elastic component, ν' is the material Poisson's ratio, while it is fixed at 0.5 for the plastic component. The total equivalent strain is the sum of the two components.

$$\varepsilon_{eq,e} = \frac{1}{1 + \nu'} \sqrt{\frac{1}{2} \left((\varepsilon_{e,1} - \varepsilon_{e,2})^2 + (\varepsilon_{e,2} - \varepsilon_{e,3})^2 + (\varepsilon_{e,3} - \varepsilon_{e,1})^2 \right)} \quad (2.15)$$

$$\varepsilon_{eq,p} = \frac{1}{1 + \nu'} \sqrt{\frac{1}{2} \left((\varepsilon_{p,1} - \varepsilon_{p,2})^2 + (\varepsilon_{p,2} - \varepsilon_{p,3})^2 + (\varepsilon_{p,3} - \varepsilon_{p,1})^2 \right)} \quad (2.16)$$

$$\varepsilon_{eq,tot} = \varepsilon_{eq,e} + \varepsilon_{eq,p} \quad (2.17)$$

Maximum Principal Strain

The maximum principal strain ε_{AMP} is evaluated identical to its stress equivalent by the use of Equation (2.18). (Stephens et al., 2001, Ch. 10.4.1)

$$\varepsilon_{AMP} = \max(|\varepsilon_1|, |\varepsilon_2|, |\varepsilon_3|) \quad (2.18)$$

Maximum Shear Strain

The maximum shear strain γ_{max} is calculated by evaluating the principal stresses and the Poisson's ratio as shown in Equation (2.19). (Stephens et al., 2001, Ch. 10.4.1)

$$\gamma_{max} = \frac{\varepsilon_1 - \varepsilon_3}{1 + \nu} \quad (2.19)$$

Lemaitre Criterion

Lemaitre (1996, p. 11-15, 95-97) introduced the Lemaitre damage criterion as a way to incorporate progressive damage into a mesomechanical approach using stress triaxiality. The approach is expanded to an estimate of the strain energy density release rate and is shown in Equation (2.20).

$$Y = \frac{\sigma_{eq}^2}{2E} R_v \quad (2.20)$$

$$R_v = \frac{2}{3} (1 + \nu) + 3 (1 - 2\nu) \left(\frac{\sigma_H}{\sigma_{eq}} \right)^2 \quad (2.21)$$

Where σ_H is the hydrostatic stress and σ_{eq} is the equivalent stress.

Strain Energy Density

Strain energy density is a measure of the strain energy per unit volume. As a fatigue indicator it captures the effect of plasticity as an increase in the strain energy stored both as elastic and inelastic energy (Stephens et al., 2001, p. 329). For elastic loading, the strain energy density is Equation (2.22).

$$w = \frac{1}{2} \sigma_{eq} \varepsilon_{eq,tot} \quad (2.22)$$

For elastic-plastic strains, the strain energy density is evaluated by numerical integration of the stress-strain curve, as shown in Figure 2.9.

2.5.1 Local and Nonlocal Models

When evaluating the above-mentioned fatigue indicators, different models can be considered, mainly local and nonlocal. A local model, commonly referred to as peak, refers to evaluating the maximum value of the fatigue indicator considered. An example of this is the effective notch stress approach which evaluates the maximum principal stress.

It is acknowledged in literature that the fatigue life of a component depends not just on the maximum stress value, but also on the stress distribution in the surrounding space of

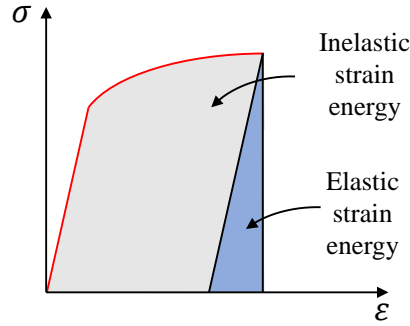


Figure 2.9. Separation of elastic and inelastic strain energy.

that maximum stress point (Kuguel, 1960b; Sonsino and Fischer, 2005; Kaffenberger and Vormwald, 2012). Small stress gradients surrounding the maximum stress value, can result in large volumes where stress values are close to the maximum stress value. On the other hand, high stress gradients can cause the highly stress volume to be localised around the maximum stress value.

Several methods are available to incorporate the effects of the stress gradient, as shown in the works by Kuguel (1960a), Bruder et al. (2008), and Härkegård and Halleraker (2010). In the following, the method of the *highly stressed volume* introduced by Kuguel (1960a) is applied. The method calculates an effective stress $\bar{\sigma}$ by considering the volume V_{90} which is subjected to 90% of the maximum value of the stress $\sigma_{a,max}$ in relation to a reference volume V_0 , as shown in Equation (2.23) (Härkegård and Halleraker, 2010). Note that different percentages may be defined for the highly stressed volume. A higher percentage means that only the very local stress gradients in the vicinity of the maximum peak are included. The size of the reference volume V_0 can be selected arbitrarily as it simply scales the resulting effective stress.

$$\bar{\sigma} = \sigma_{max} \left(\frac{V_{90}}{V_0} \right)^\kappa \quad (2.23)$$

The highly stressed volume and reference volume are related with exponent κ , which is determined by minimising the coefficient of variation COV given by Equation (2.24), the relative standard deviation, for an entire data as illustrated in Figure 2.10.

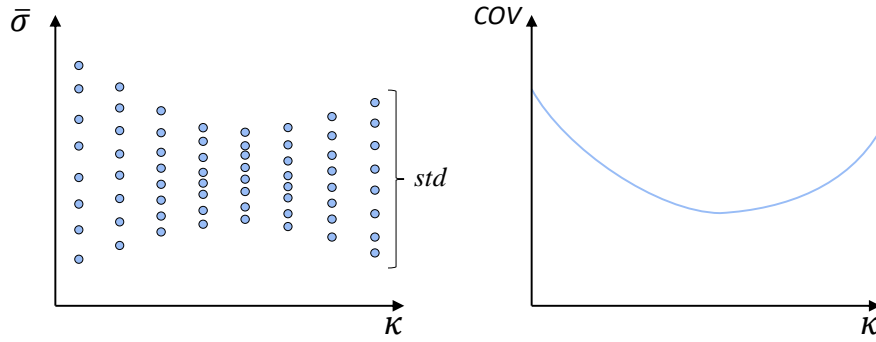
$$\text{COV} = \frac{std}{\bar{x}} \quad (2.24)$$

Similar to a highly stressed volume, the method is also applied for a highly stressed area by simply substituting A_{90} and A_0 into Equation (2.23). Though these methods relates to a highly-stressed-volume and -area, they are applied for all fatigue indicators presented in Section 2.5.

2.5.2 Stress Range vs Stress Amplitude

For welded components, the previously mentioned methods, nominal, hot-spot, and effective notch stress, all compute the stress range by Equation (2.25).

$$\Delta\sigma = \sigma_{max} - \sigma_{min} \quad (2.25)$$



(a) Effective stress $\bar{\sigma}$ for data set at different exponent κ values. (b) Minimisation of coefficient of variation for finding the exponent κ .

Figure 2.10. Illustrative procedure for obtaining exponent κ for a data set.

Applying the concept of the stress range for the fatigue indicators in Section 2.5, will for several of the indicators presented produce a range equal to zero. This can be remedied by evaluating the sign of the fatigue indicator, such as in the case of the equivalent stress, thus a stress range is obtained. However, this is not the case for Lemaitre Criterion. For a fully reversed load case, the stress amplitude σ_a is half the stress range. The consequence of evaluating the amplitude load for a fully reversed load case instead of the load range, is *only* that the intersection B of the Basquin equation differs. The remainder of this work will evaluate the amplitude loading, due to the fully reversed load case, such that all fatigue indicators can be applied.

2.6 Geometrical Weld Features

To investigate correlations between the fatigue indicators, or the corresponding lifetime, the geometrical features of weld must be quantified. The geometrical features are limited to the external measurements of imperfect shape and dimensions shown in Figure 2.11.

To obtain a magnitude of the allowable geometrical imperfections, the weld quality class based on DS/EN-ISO-5817 (2023) is highlighted. DS/EN-ISO-5817 (2023) is commonly used in conjunction with Hobbacher (2016) and DNVGL-OS-C401 (2017) for joints loaded in fatigue. The weld classes vary from **D** to **B**, with **B** being the highest weld quality class. When applying DS/EN-ISO-5817 (2023) for fatigue, the weld classes are expanded upon for the relevant FAT strength. As shown in Table 2.1, weld class **B** can both be applied for FAT 90 and 125 depending on the geometrical measurements.

2.6.1 Measurement of Weld Features

To investigate correlations between the fatigue indicators and the geometrical features of each weld as obtained by laser scanning, it is necessary to establish methods with which these geometrical features can accurately be identified and extracted from the laser scans. No consensus on the *correct* identification of weld features based on digital data in the form of standards, known to the authors, has been established. The features that are most

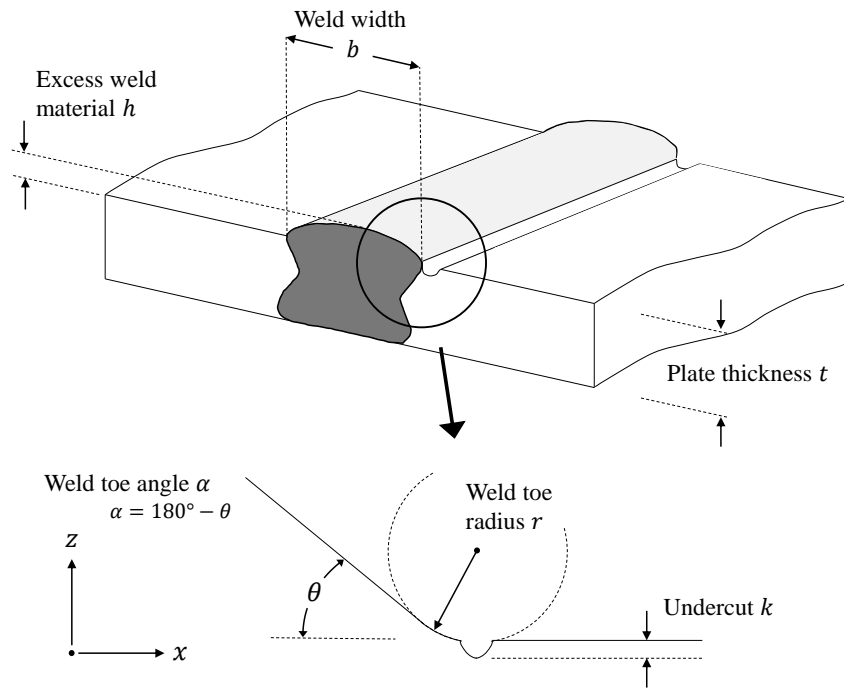


Figure 2.11. Quality of weld defined by weld measurements of butt welded joint. (Adapted from Schork et al. (2018))

troublesome to correctly obtain from laser scan data are the weld toe radius r and the weld toe angle α . Currently, various methods are employed in the literature to determine these geometrical features. However, literature specifically addressing butt welds is limited. The following presents a study of the relevant literature within the field.

Stenberg et al. (2012)

Stenberg et al. (2012), are to the authors knowledge, the first to present an algorithm for obtaining the weld toe radius and angle for a T-joint. The weld toe radius is obtained by applying a least square fit for a circle at the weld toe, and selecting the smallest calculated radius. The weld toe angle is obtained by considering the radius and the arc length c . The principle of the method is shown in Figure 2.12. Stenberg et al. (2012) did not consider the presence of undercuts.

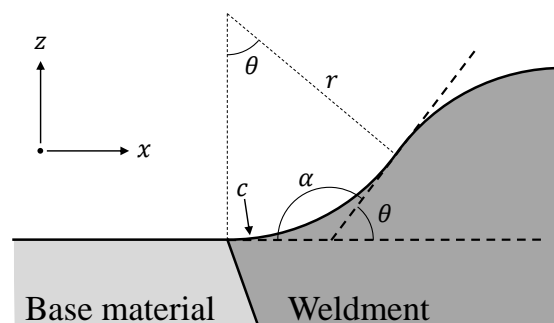


Figure 2.12. Method proposed by Stenberg et al. (2012). Adapted from Stenberg et al. (2012).

DS/EN-ISO-5817 (2023)

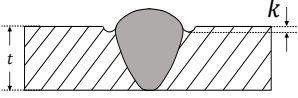
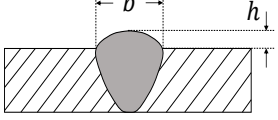
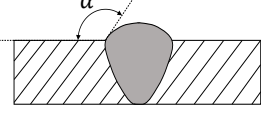
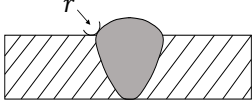
Reference No.	Designation		C63	B90	B125
5011	Continuous undercut		$h \leq 0.1 t$	Not permitted	Not permitted
5012	Intermittent undercut		$h \leq 0.1 t$, but max. 0.5 mm	$h \leq 0.05 t$, but max. 0.5 mm	Not permitted
502	Excess weld material		$h \leq 0.15 b + 1 \text{ mm}$, but max. 7 mm	$h \leq 0.1 b + 1 \text{ mm}$, but max. 5 mm	$h \leq 0.1 b + 0.2 \text{ mm}$, but max. 2 mm
505	Incorrect weld toe angle		$\alpha \geq 110^\circ$	$\alpha \geq 150^\circ$	$\alpha \geq 150^\circ$
5052	Incorrect weld toe radius		-	$r \geq 1 \text{ mm}$	$r \geq 4 \text{ mm}$

Table 2.1. External imperfections and weld classes relevant for butt weld loaded in fatigue. Note that several requirements for the 2023 version have been changed from the previous 2014 version. (DS/EN-ISO-5817, 2023)

Schubnell et al. (2019)

Schubnell et al. (2019) conducted a round-robin study of both manual and algorithmic methods for determining the weld toe radius and angle by use of laser scanning for both butt- and T-joints. The study proposes a *curvature method* due to its simplicity and reliable performance in determining the weld toe radius. The principle of the method is to use the inverse relation between the curvature κ and radius of a plane circle to determine the size of the weld toe radius as shown in Equation (2.26).

$$r = \frac{1}{\kappa} \quad (2.26)$$

To obtain continuity for the data, a polynomial is fitted allowing an analytical evaluation of the curvature. The weld toe angle is calculated by comparing the angle of a fitted line for the base material, and a fitted line for the weldment. Schubnell et al. (2019) assumes that no undercut is present.

Renken et al. (2021)

Renken et al. (2021) proposes an algorithm for evaluating the weld toe radius for a T-joint based on the osculating circle as shown in Equation (2.27). A piecewise cubic spline fit is applied to obtain a continuous analytical definition of the weld.

$$r = \left| \frac{\left(1 + \left(\frac{dz}{dx}\right)^2\right)^{3/2}}{\frac{d^2z}{dz^2}} \right| \quad (2.27)$$

Selection of Methods

In this work, the weld toe radius and angle is determined using the method recommended by Schubnell et al. (2019). Chapter 8 will expand upon the application of this method. However, none of the available literature presents methods for determining the undercut, excess weld material or width of the weld. As such, Chapter 8 will present a self-developed method for determining these remaining measurements.

2.7 Problem Statement

Based on the purpose of this report presented in Chapter 1, the methodology for quantifying the scatter of data in Sections 2.3 and 2.4, and the fatigue indicators and models to be investigated presented in Section 2.5 as well as their link to the geometrical weld features in Section 2.6, a two-part problem statement is formulated as follows:

Is it possible to reduce the scatter of fatigue data of welded butt joints in low cycle fatigue, when compared to the nominal approach, by considering the local weld geometry obtained by laser scanning?

Is it possible to establish a correlation between the fatigue performance and the geometrical weld features?

3 Experimental Methods

The experimental data for this project was conducted in the authors' 9th semester project. This chapter serves as a detailed summary of the necessary information of the experimental data from Hermansen and Sørensen (2022).

3.1 Specimens

The specimens considered are one-sided butt welds as shown in Figure 3.1. The welding was conducted according to Liftra's internal weld procedure qualification record certified by DNV GL in accordance with DNVGL-OS-C401 (2017). The weld quality, in relation to DS/EN-ISO-5817 (2023) and Table 2.1, is specified as **C**.

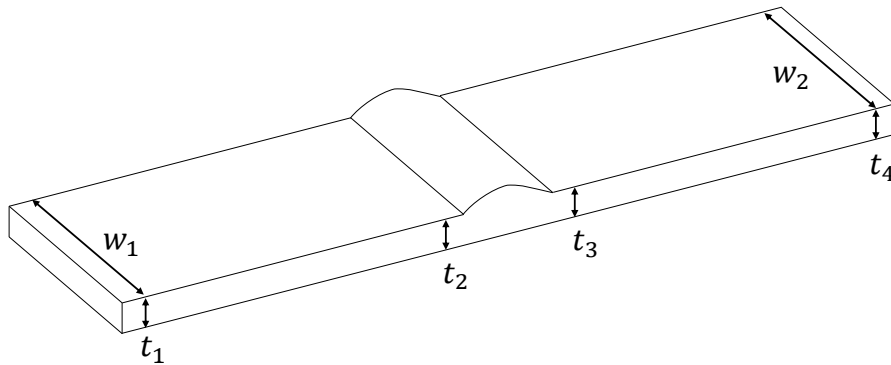


Figure 3.1. Geometrical sizes and measuring points.

No post weld treatment is specified. However, all 32 specimens in S960 are disk ground, while 17 of the 33 specimens in S690 are also disk ground. Figure 3.2 shows the result of the post weld treatment. Hermansen and Sørensen (2022, Ch. 6.2) concluded that the post weld treatment had no effect on the nominal SN curve for S690.

After welding, the specimens are cut to size using a saw and the bottom side is machined plane. The specimens are manufactured to a nominal thickness t and width w of 6 mm and 50 mm respectively. Due to both the angular and axial misalignment of the welding process, each specimen is measured at the six locations shown in Figure 3.1. Each thickness measurement is done with a micrometer with a resolution of 0.01 mm, while the width measurements are done with a caliper with a resolution of 0.05 mm.



(a) Partial grinding of S690 specimen.

(b) Grinding of entire S960 specimen.

Figure 3.2. Figures from Hermansen and Sørensen (2022).

3.2 Laser Scanning

This section will present the procedure and principle for the laser scanning acquisition of the welded specimens.

The experimental setup consists of a Wenglor MLWL153 laser line scanner mounted to a KUKA Quantec KR 120 industrial robot. The scanner works by the principle of laser triangulation and captures a single profile in its local xz -coordinate system as shown in Figure 3.3. A single profile consists of 2048 xz -points unless the points are outside the field of view. The entire 3D scan of the weld is captured by moving the robot in a linear trajectory parallel to the length of the weld. The robot moves at a constant speed and distance to the base on which the welded specimen is positioned. The laser scanner samples a profile at a fixed y -spacing, resulting in a complete 3D scan, point cloud, of the specimen as illustrated in Figure 3.3. The resulting scan file measures 64 MB, totalling 3.44 GB for all 65 specimens.

Table 3.1 shows the specifications of the laser scanner. Currently, no standardised requirements for digital measurement are available. However, the y -spacing is less than the recommended y -spacing of 0.8 mm from Renken et al. (2021). Thus the applied y -spacing is within the recommendations. As illustrated by Figure 3.3, the x -spacing is depended on the placement of the specimen within the field of view. The average x -spacing is measured at ~ 0.093 mm for all scans.

Scan specification	Axis	Measurement spacing	Working range [mm]	Resolution [mm]
Scan width	x	2048 points pr. scan profile	150-230	0.079-0.12
Scan length	y	0.1 mm	99.9	
Scan height	z	2048 points pr. scan profile	215-475	0.0096-0.022

Table 3.1. Scan specifications (Wenglor, 2023).

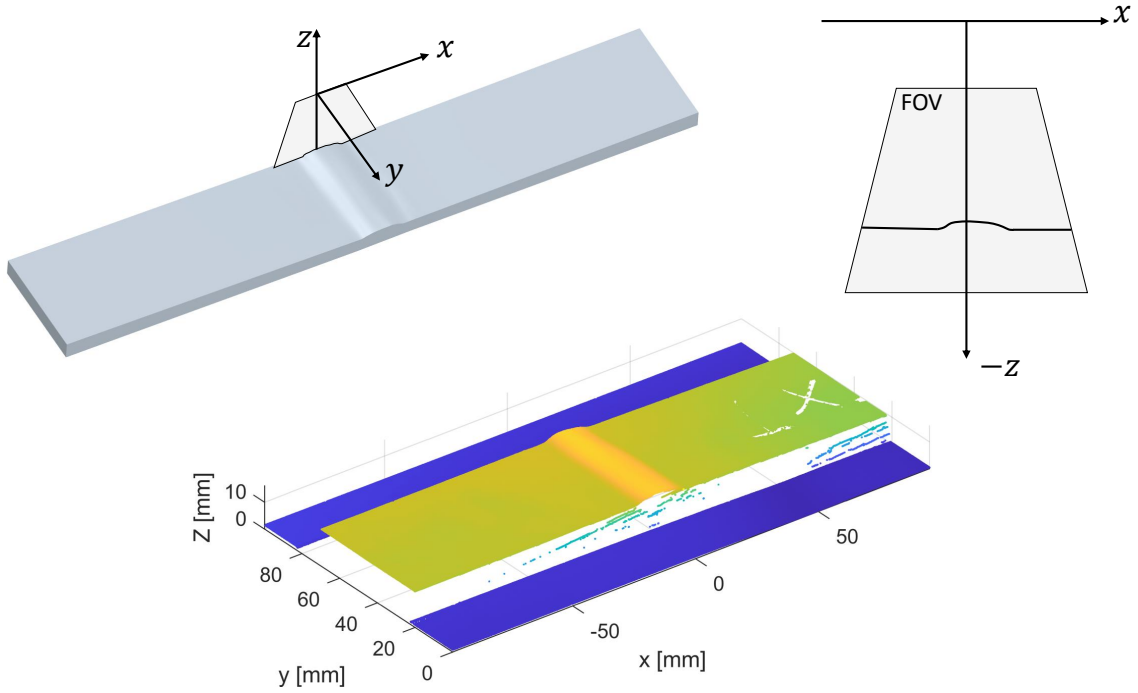


Figure 3.3. Local coordinate system of the laser scanner and the resulting point cloud.

3.3 Tensile Test

Tensile testing of standardised dog-bone test specimen made in the base materials was conducted. Each material was tested at 0° and 90° to the rolling direction with a tee-rosette strain gauge mounted. Table 3.2 shows the resulting strengths, Young's modulus and Poisson's ratio.

Both materials obtained values greater than the minimum values prescribed in DS/EN-10025-6 (2019). The strength value of S960 in the 0° rolling direction are not recorded due to failure of the test fixture.

	R.D.	R_{eL} [MPa]	R_{eH} [MPa]	S_{ut} [MPa]	E [GPa]	ν
S690QL	0°	847.1	867.8	957.7	223.0 ± 7.7	0.279 ± 0.003
	90°	843.9	856.5	958.1	196.5 ± 6.8	0.295 ± 0.003
S960QL	0°	-	-	-	248.2 ± 6.9	0.349 ± 0.003
	90°	1038.8	1039	1115.7	178.1 ± 7.0	0.255 ± 0.003

Table 3.2. Material parameters from monotonic tensile test. (Hermansen and Sørensen, 2022, Ch. 5.1)

3.4 Fatigue

Each specimen is subjected to stress-based fatigue using a Schenck 400 kN servo-hydraulic testing machine. The load is applied through a four-points bending fixture, shown in Figure 3.4, resulting in a constant moment across the entire weld. The fatigue testing is conducted at a constant stress ratio of $R = -1$, i.e. with zero mean stress. All specimen fractured due to weld toe failure. The resulting nominal stress SN curve is shown in Figure 1.1.

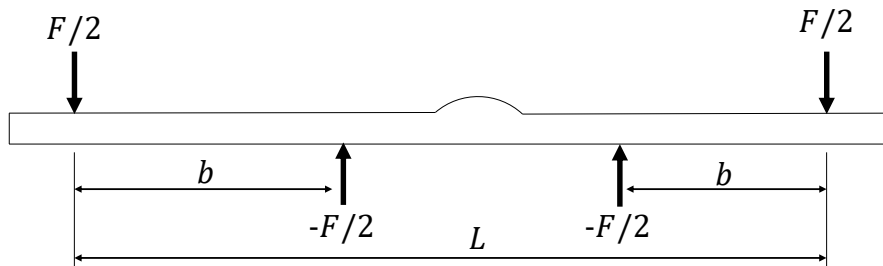


Figure 3.4. Applied load for four-point bending. $b = 65$ mm, $L = 250$ mm.

4 Processing and Construction of Solids

This chapter will describe the process of converting the discrete laser scan measurements to continuous surface with C^2 continuity and superimposing the laser scan onto a 3D solid model.

4.1 Reverse Engineering Method

For evaluating the stress state of a given laser scan, a 2D or 3D model can be considered. However, a 2D model is limited to assuming a plane-stress or strain state and does not incorporate the neighbouring geometry. In this work, the effects of neighbouring geometry will be taken into account by utilising a 3D model. The laser scans presented in Section 3.2 are thus to be converted to 3D finite element models. In order to obtain a FE model, the discrete laser scan must be reversed engineered to a C^2 continuous CAD model. Several methods have been applied for this process, as shown in the works by e.g. Hou (2007), Lang and Lener (2016), Hultgren et al. (2021), and Shojai et al. (2022).

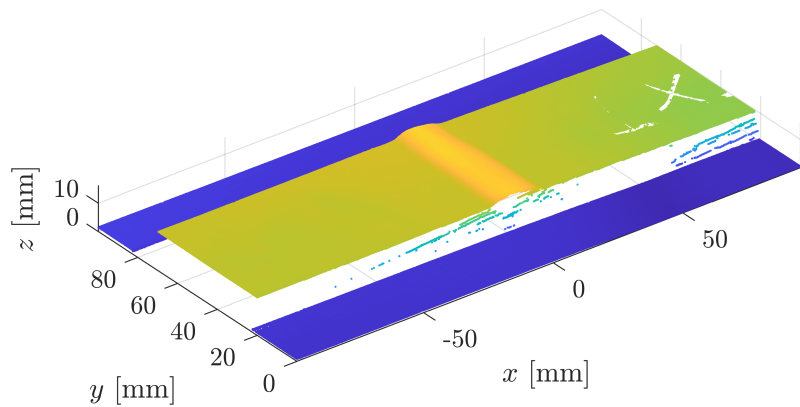
In this work, a process inspired by Lang and Lener (2016) and Shojai et al. (2022) is applied. The programs MATLAB, MeshLab, and SpaceClaim, are used to achieve the process. The process consists of the following six steps, each of which are described in the following sections.

1. Trimming
2. Repairing defects
3. Filtering
4. Triangulation of surface
5. NURBS surface
6. Closing volume

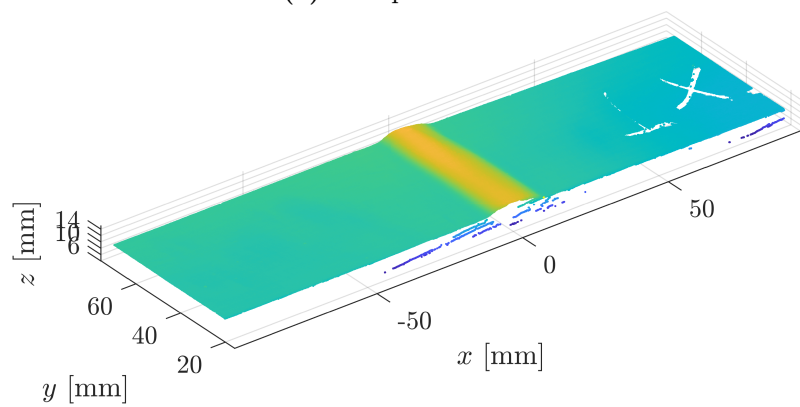
4.2 Trimming

Two types of data trimming is applied to the raw point cloud captured from the laser scanning process shown in Figure 4.1a. The base plate on which the specimens were

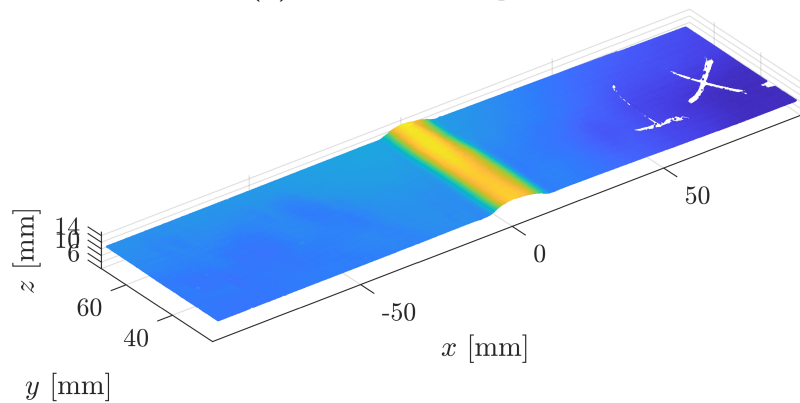
placed is removed by evaluating a fixed z -value and removing points, as illustrated in Figure 4.1b.



(a) Raw point cloud.



(b) Removal of base plate.



(c) Manual edge trimming of laser scan.

Figure 4.1. Point cloud trimming process

At the transition between the base plate and the specimen, the laser scanner is unable to accurately capture the edge of the specimen. As a result, the edges have a reduced z -value compared to the real geometries. This is most likely caused by too high of a trajectory speed of the KUKA robot. As a consequence, the outer edges of the laser scans are trimmed by a manual process in MeshLab. The criteria for the manual trimming process is to only remove laser profiles which have a reduced z -value compared its neighbouring profile. The result of an edge trimming process is shown in Figure 4.1c.

4.3 Repairing Defects

In the laser scanning process, if a point along a laser profile is not within the field of view shown in Figure 3.3, the point will be missing in the acquisition of the point cloud. This causes a profile to have less than 2048 points along the affected profile. This is illustrated in Figure 4.2, with two profiles of the same x -length. However, one profile is missing two data points, resulting in two fewer data entries.

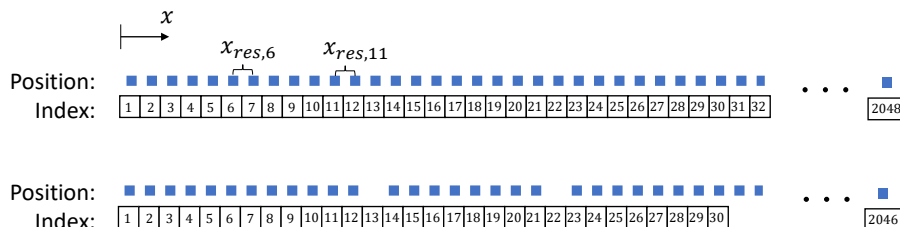


Figure 4.2. Illustrative concept of missing data. Data point 13 and 22 are missing.

The missing data points are caused by two factors. Firstly, each specimen had a unique ID number drawn on its top surface using a black marker. Due to low amount of light being reflected at the drawn on ID number, the data points are not within the field of view of the scanner. In the extreme cases, this can cause more than 100 missing data points as shown in Figure 4.1c. Secondly, localised geometrical changes, such as a sudden concavity in the surface, can cause a spike in the reflected light, hence also being located outside of the field of view.

The missing data points along a profile is required to be regenerated in order to apply a low pass filter, which will be discussed in Section 4.4. As every laser profile has a unique x -spacing, the missing data points can not be simply evaluated by evaluating the x -spacing between each points.

The missing data is reconstructed by evaluating the closest neighbouring profile that is not missing any data. This establishes an expected lower and upper bound of the positional x -data. If the start and end data of the profile is missing a data point, the point is simply reconstructed by assuming the same boundary as the neighbouring profile. By evaluating the x -spacing, potential candidates for missing points are established. If these are within the x -value of the neighbouring profile, with an applied tolerance, the point is reconstructed. The z -value of the reconstructed point is found by either extra- or interpolating the z -value of the profile itself. This process is implemented in a MATLAB script. The resulting interpolating is shown Figure 4.3 for the specimen with the worst case of missing data. For this specimen, 220 points along a single profile are missing due to the black marker.

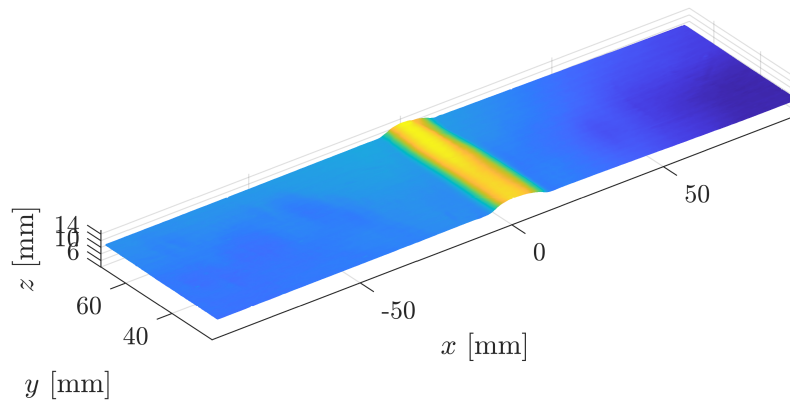


Figure 4.3. Missing data points shown in Figure 4.1 have been interpolated.

4.4 Filtering

Having reconstructed any missing data point for every scan, a noise filtering is applied. Three sources of noise is identified which can be categorised as caused by the laser or the robot's movement. Figure 4.4 shows the noise of a laser profile.

Firstly, two types of noise is caused by the laser scanner: the tolerances for the positional data supplied by the manufacture, and the user-defined exposure time. The noise due to the positional tolerances is found to follow a completely random pattern. The noise from too long of an exposure time follows a normal distribution in both the x and y direction.

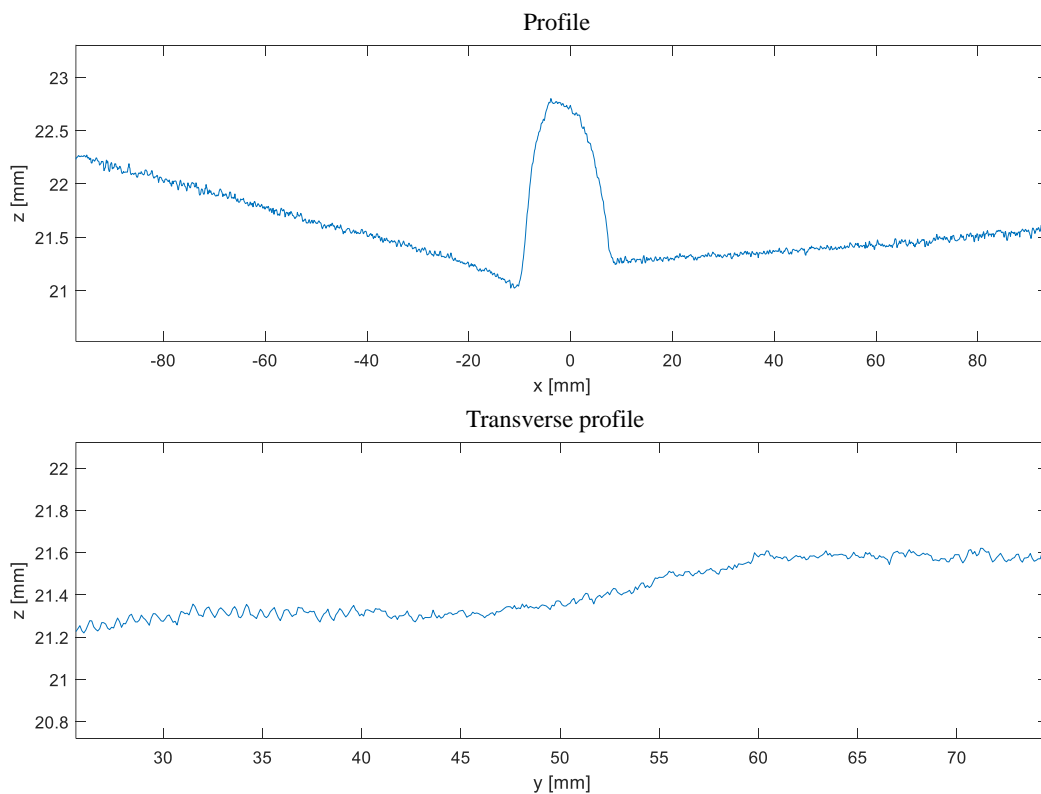


Figure 4.4. Raw laser scan data of profile and transverse profile. Note that the axes are not scaled 1:1.

Secondly, noise produced by the robot results in a sinusoidal noise wave in the direction of travel for the robot, i.e. in the y -direction. This noise is visible if a transverse profile is considered, a profile in the y -direction instead of x as shown in Figure 4.4. The construction of transverse profiles with equal lengths, is possible due to the implemented interpolation from Section 4.3. The sinusoidal noise due to the robot is only visible for the first part of the transverse profile.

To filter the laser scans, a low-pass filter is implemented in a MATLAB script. In order to quantify the cutoff frequency ω_0 , in which the low-pass filter should activate, the amplitude spectrum of the profile is desired. This is obtained through a fast Fourier transform. The resulting amplitude spectrum for a profile and transverse profile are shown in Figure 4.5.

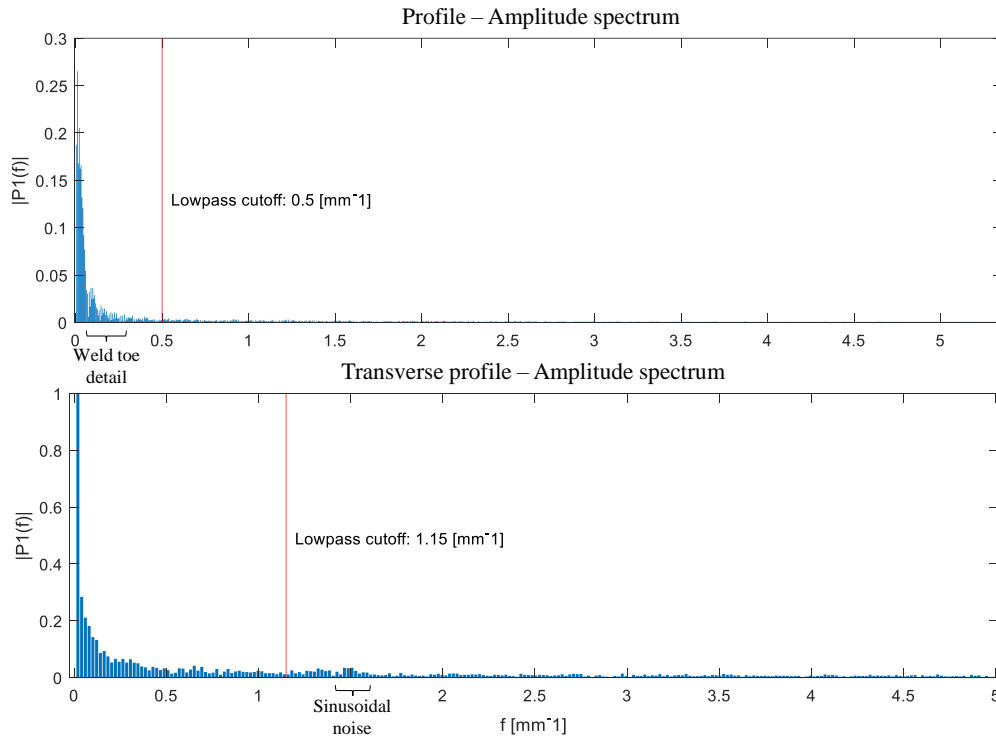


Figure 4.5. Amplitude spectrum for the profile and transverse profile shown in Figure 4.4.

For a profile, the amplitude spectrum is found to contain the weld toe detail in the range 0.05 mm^{-1} to 0.3 mm^{-1} . As such, the cutoff frequency for the filter should be greater than this upper bound as not to influence the geometrical features of the weld. Through an iterative process, a cutoff frequency of $\omega_0 = 0.5 \text{ mm}^{-1}$ is found to be adequate for all laser scans.

The transverse sinusoidal noise is found to be centred about 1.5 mm^{-1} . It should be noted that the sinusoidal noise pattern does not occur along the entire transverse profile, nor does it exist on every transverse profile. A transverse cutoff frequency of 1.15 mm^{-1} is selected for all laser scans.

The low-pass filters are constructed by the use of a fourth order Butterworth filter design

and implemented using a zero-phase filter. Figure 4.6 shows the unfiltered and filtered profile and transverse profile.

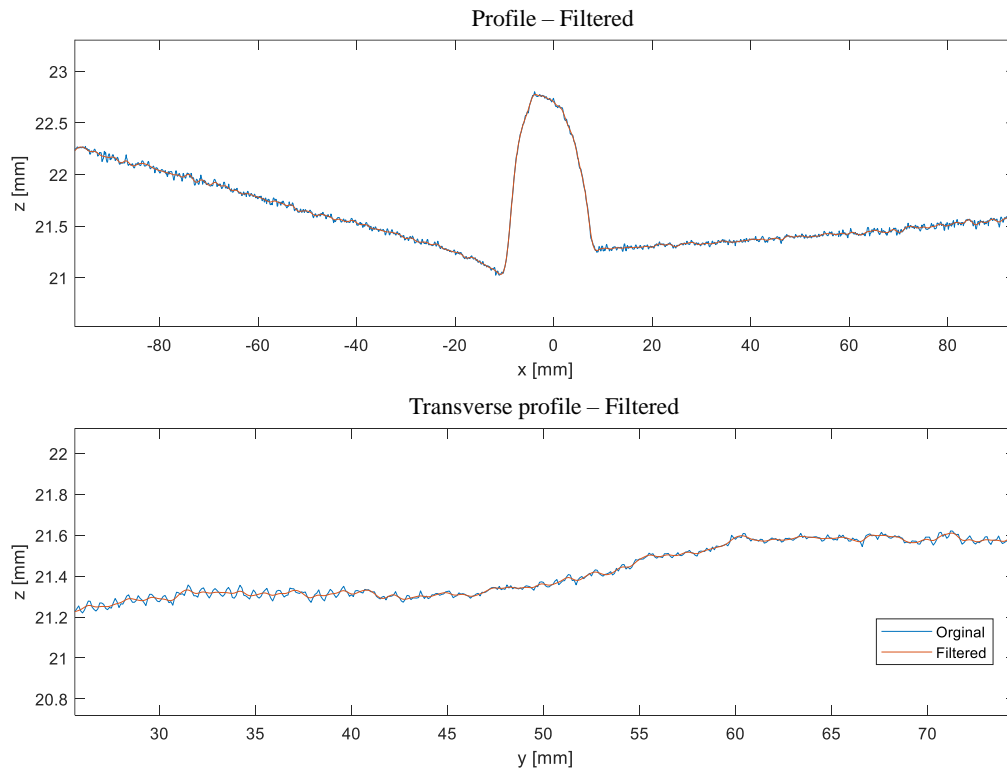


Figure 4.6. Unfiltered and filtered profile and transverse profile. Note that the axes are not scaled 1:1.

4.5 Surface Construction

With a trimmed and filtered laser scan, the remaining geometry of the weld can be constructed based on manual measurements, mentioned in Section 3.1. From these measurements, the laser scan can be superimposed on the external geometry, generating a set of discrete corner points for the specimen. To reduce the number of points, and the subsequent file size, only the weld toe is superimposed.

Weld Toe Detection

In order to obtain the laser scan which is to be superimposed, an algorithm for determining the weld toe location is developed. The gradient and curvatures of each laser profile is examined in a MATLAB script, as shown in Figure 4.7. The gradient and curvature is numerically evaluated by a central difference approach. However, to not lose any data, the first and last points are evaluated using a backward- and forward- difference approach respectively. The maximum peak of each weld toe is determined as an indicator of the location of the smallest weld toe radius. However, due to the geometrical variety along a weld profile, the curvature value can not be solely examined. Hence, the value of the gradient is examined. When the gradient approaches zeros, the location will be at the

base plate. To distinguish between each side of the weld toe, the sign of the gradient is evaluated. This results in the vertical lines in Figure 4.7 and is used for estimating the location of the weld toe.

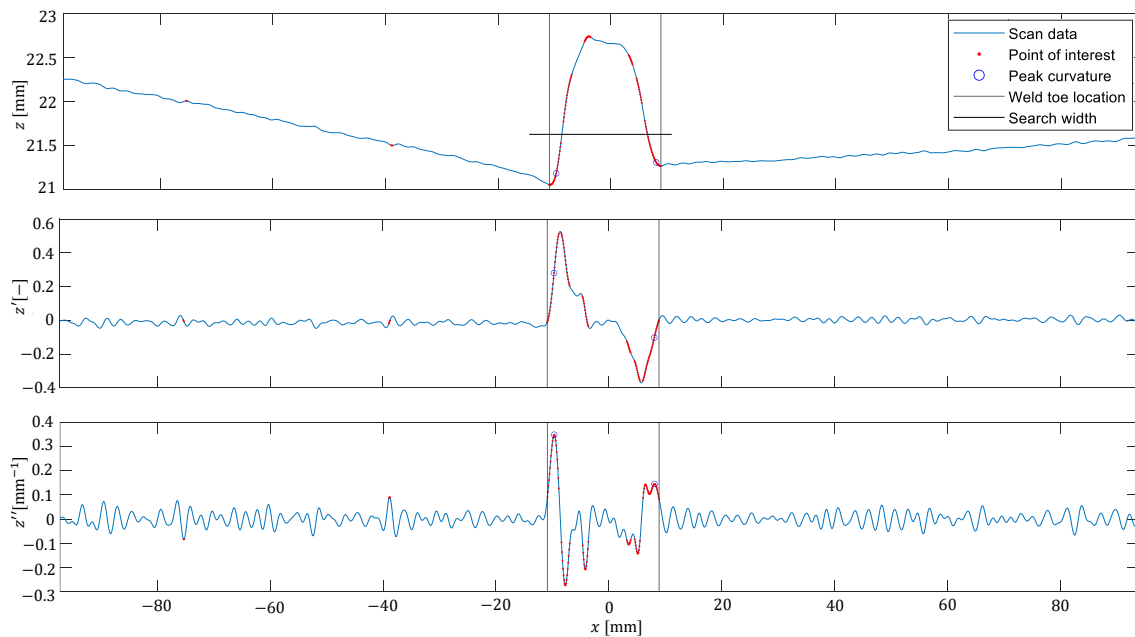


Figure 4.7. Positional, gradient, and curvature data and the resulting weld toe detection. Note that the axes for the positional data is not scaled 1:1.

Applied to an entire point cloud, the resulting weld toe detection is shown in Figure 4.8. As shown, the location of the weld toe varies along a weld. To ensure a well defined transition between the superimposed laser scan and the external measurements, the weld toe detection is extended as shown in Figure 4.9.

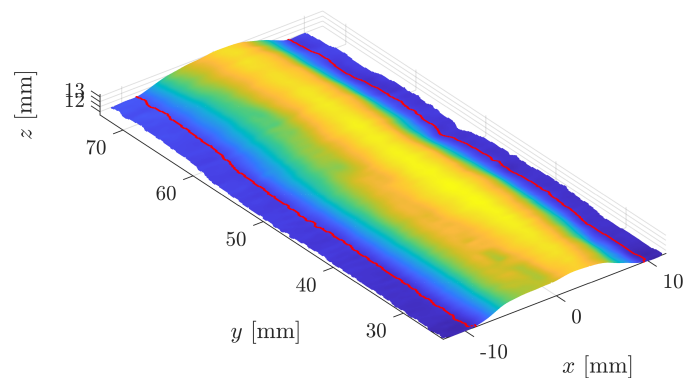


Figure 4.8. Applied weld toe detection.

Construction of Surface Model

Several methods for converting a point cloud to a solid CAD model exists through commercial means. However, the method used in this project is self-developed, and is based on two concepts. Firstly, the discrete points of the laser scans are converted to a surface by the use of triangulation and saved as a .stl file format. Secondly, a non-uniform

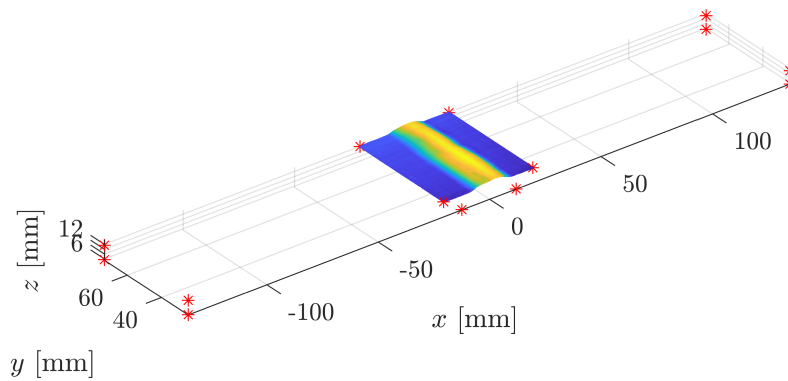


Figure 4.9. Weld toe superimposed on external measurement points.

rational basis spline (NURBS) algorithm is used to construct a CAD surface, which can be enclosed to obtain a watertight solid CAD model.

Through the conversion to .stl format, no approximations are made. The .stl file format simply describes the discrete points as a triangular surface with a normal, as shown in Figure 4.10. The triangulated surface thus has C^0 continuity.

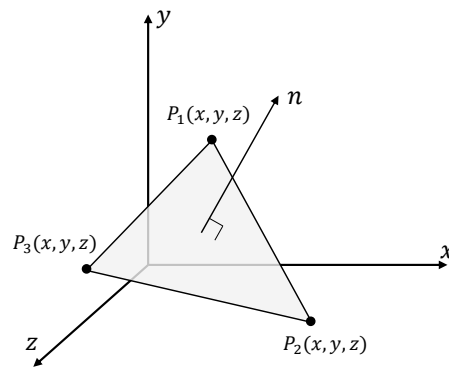


Figure 4.10. Principal for every generated surface in a .stl file.

A surface model is shown in Figure 4.11, where the difference in surface density is shown by the few faces on the base plate.

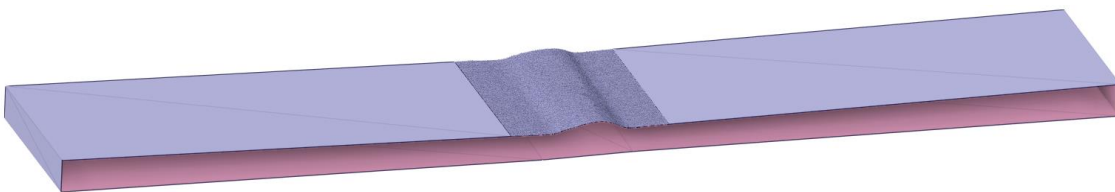


Figure 4.11. .stl based surface model. No surface model on the side of the specimen.

4.6 Solid Construction

The surface model based on the .stl conversion is only positional continuity C^0 . In order to obtain C^2 continuity a NURBS algorithm implemented in the commercial software SpaceClaim is applied. As the NURBS algorithm is just applied, the underlying theory will not be described. Different methods of calculating the NURBS are available, however the SpaceClaim documentation provides no insight into the specific methods used (ANSYS, 2023c, Ch. 11.1). Based on the output of the algorithm, it is observed, that in the case of large geometrical deviations, the algorithm switches to a principal of *best-fit spline* in order to maintain C^2 continuity, thus producing an error between the inputted .stl file and the outputted NURBS surface.

To determine the magnitude of this error and assess its acceptability, the Euclidean distance is calculated between the .stl file and the NURBS surface, resulting in a deviation plot. Two deviation plots are shown in Figure 4.12. Green represents deviations within a tolerance of ± 0.01 mm, while blue and red indicate deviations outside the tolerances. Figure 4.12a represents a common deviation plot where a single or few points at the weld toe have deviations outside the tolerance. Figure 4.12b shows a worst case deviation plot where several areas are outside the range of the tolerance.

An error of ± 0.05 mm at the fractured weld toe was determined acceptable. However, no specimens has a deviation measured greater than ± 0.03 mm at the location of the fractured weld toe.

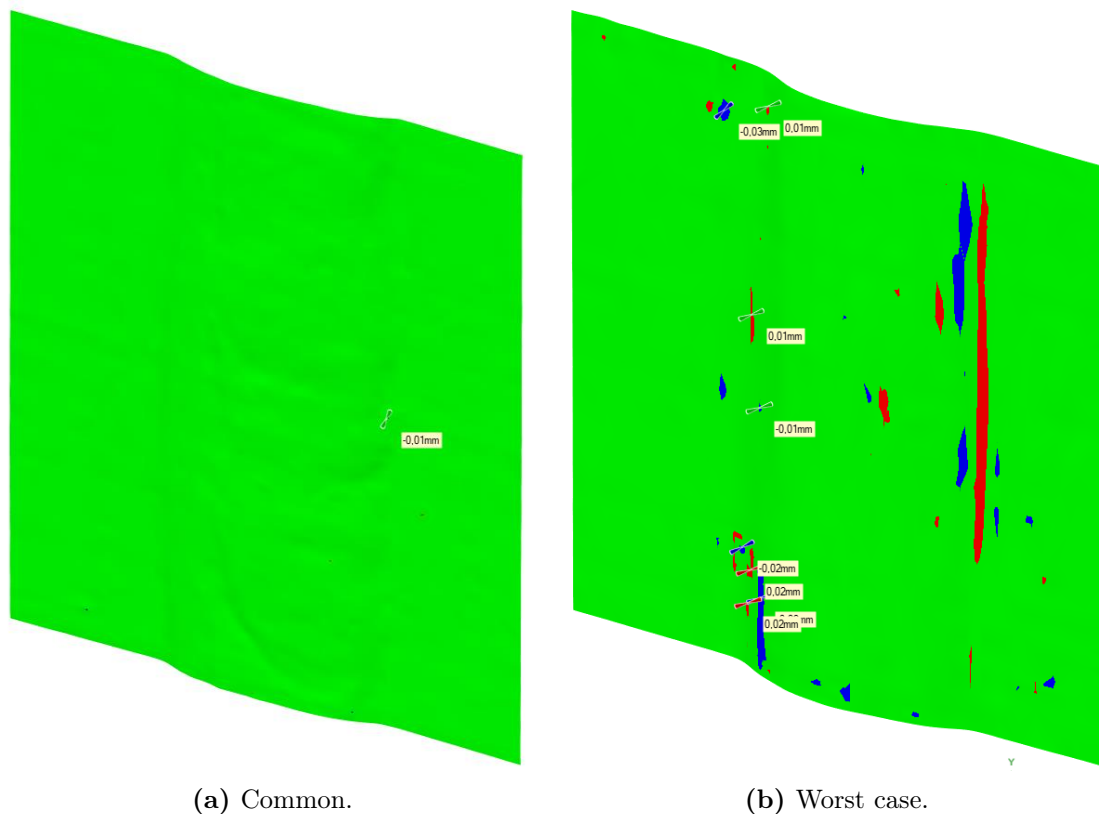


Figure 4.12. Deviation plots.

Based on the measured errors, the method for constructing NURBS surfaces is deemed acceptable. The entire surface model can thus be constructed to a solid CAD model. Figure 4.13 shows the surface model from Figure 4.11 made to a solid CAD model. The resulting file size of the CAD models varies between 2.2 MB to 12.9 MB, with an average of 6.2 MB.

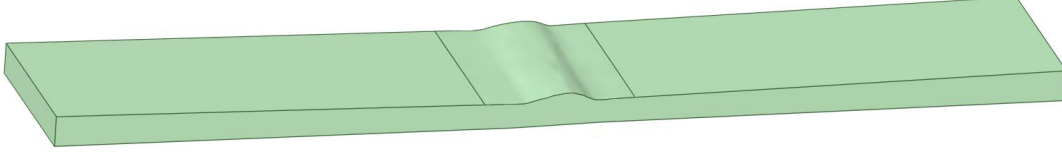


Figure 4.13. Final solid model.

4.7 Compensation of Nominal Differences

Throughout the generation of the solid model, three operations are applied which has an influence on the geometry of the specimen. Firstly, the edge of the laser scans were trimmed. As such, the width of each specimen will be reduced compared to the actual specimen. Secondly, in the process of superimposing the laser on external measured points, as shown in Figure 4.9, an approximation is applied in order to conform with geometrical boundary conditions of the bottom plane surface, causing a difference in the thickness measurement. Thirdly, the use of NURBS can for some specimens result in a deviation at the weld toe.

All solid generated models are measured in the identical locations to the external measurements, which were done with a caliper and micrometer. Hence, the error of the models nominal geometrical sizes are known. In order to compensate for the geometrical difference between the solid model and the external measurements, the applied load is corrected using Equation (4.1). Equation (4.1) is based on the assumption that the nominal bending stress should be equal for the external measurements and solid model. However, this method does not account for the deviation due to NURBS.

$$\sigma_{model} = \sigma_{measured} \tag{4.1}$$

$$F_{model} = F_{measured} \frac{w_{model} t_{model}^2}{w_{measured} t_{measured}^2}$$

5 Finite Element Modelling of Laser Scans

This chapter will detail the setup, considerations, and post-processing of the finite element model for each specimen.

5.1 Boundary Conditions and Setup

This section will describe the boundary condition and load of the four-point bending setup for the finite element model of each specimen.

Figure 3.4 showed the applied load in the four-point bending fixture. For the FE model, only the tensile loading is considered as described in Section 2.5.2. The boundary condition are based on the study conducted in Hermansen and Sørensen (2022, Appx. B). The boundary condition and load is shown in Figure 5.1 and is the following:

- A) Amplitude load in z -direction along load line.
- B) Fixed displacement of y and z along load line.
- C) Fixed displacement of x and y at the centre of the specimen.



Figure 5.1. Boundary condition and load for FE model.

The C) boundary condition is necessary to have a fully constrained model and is applied under the assumption of symmetry. As mentioned in Section 2.5.2 no reversal of the load is considered, thus only a load in the positive z -direction is considered. Due to the high

amount of plasticity for the specimens, geometrical non-linearity is applied for the FE model.

5.2 Material Model

The material model used represents a cyclic material model based on a strain-controlled fatigue test hysteresis loop. The cyclic material model is estimated based on the experimentally obtained monotonic values presented in Table 3.2 and calculated using Equations (5.1) to (5.5) as described in Zhang and Maddox (2009).

$$\sigma'_y = 0.608 S_{ut} \quad (5.1)$$

$$b = -0.1667 \log_{10} (2.1 + 917/S_{ut}) \quad (5.2)$$

$$-0.7 < c < -0.5 \quad (5.3)$$

$$n' = b/c \quad (5.4)$$

$$K' = \sigma'_y (0.002)^{-n'} \quad (5.5)$$

Both the experimental monotonic and estimated cyclic stress-strain curves are shown in Figure 5.2. Table 5.1 shows the calculated cyclic parameters. The estimated cyclic stress-strain curves uses a Young's modulus of 200 GPa and Poisson's ratio of 0.3. The material model is not intended to describe the evolution of the stress-strain hysteresis loop for fully reversed loading. Thus, the cyclic hardening effect of the material is not modelled.

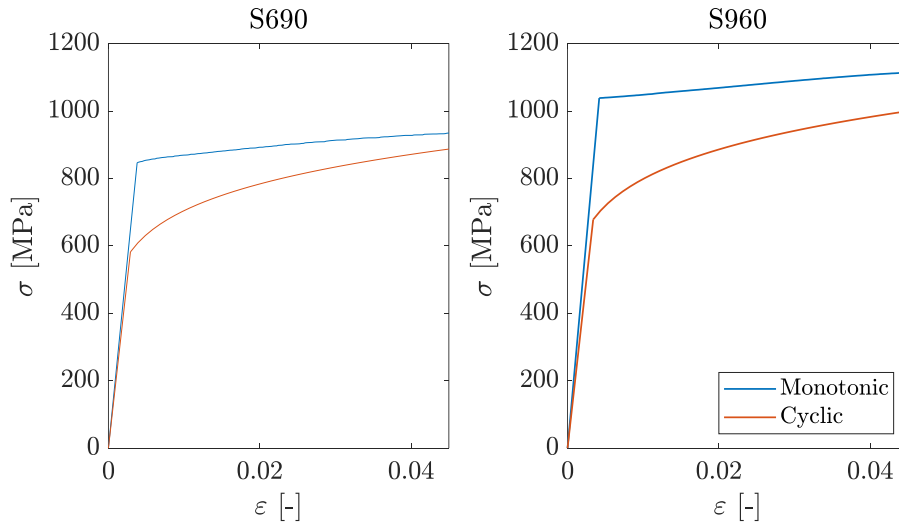


Figure 5.2. Monotonic and estimated cyclic material models.

	σ'_y [MPa]	K' [MPa]	n'
S690	582.28	1452.7	0.1471
S960	678.35	1630.7	0.1411

Table 5.1. Estimated cyclic values.

5.3 Local Mesh Convergence Study

To ensure the finite element model is able to capture the level of detail of the laser scan, two mesh convergence studies are conducted. This section will describe a local mesh convergence study, which examines the mesh at the fractured weld toe. Section 5.4 will describe a global mesh convergence.

To limit the computational time and file size, the region of mesh at the fractured weld toe is defined, similar to the approach applied in Hultgren et al. (2022). To determine the size of the mesh region, a study using an idealised weld geometry presented in Hermansen and Sørensen (2022, Ch. 5.4) is conducted. The study evaluated the distance from the weld from which the stress and strain state reached a nominal value, i.e. no stress-raising effects from the weld geometry. This distance comes to be 2.4 mm equivalent to $0.4t$. Based on this information the surface area of the stressed region around the fractured weld toe is defined by a range of ± 2.4 mm from the weld toe region detected using the algorithm presented in Section 4.5. The volume is defined by moving the surface area down into the geometry by a distance of 1 mm. The resulting fine mesh at the fractured weld toe is shown in Figure 5.3

The local mesh at the weld toe is constructed to satisfy the spacing of the laser scans. Thus, the mesh in the y -direction has a fixed spacing according to the laser scan of 0.1 mm. The convergence study is thus examining the mesh spacing along a profile, i.e. the x -direction. For all studies, the x -spacing is also applied for the mesh in the z -direction. To ensure a transition between the local and global mesh, an adaptive sizing is applied. The resulting mesh is shown in Figure 5.3.

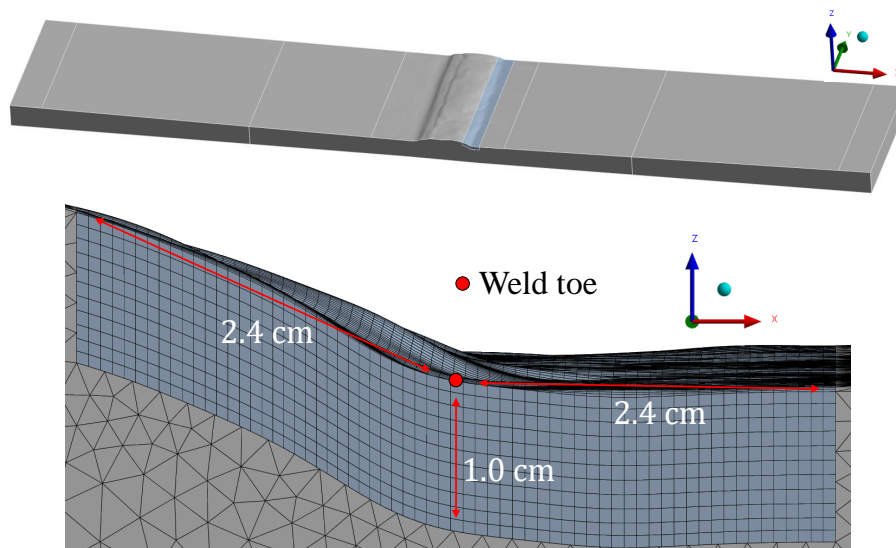


Figure 5.3. Global and local mesh at the weld toe.

The measure for the mesh convergence is the maximum equivalent stress and strain. As the models are subjected to plasticity, the change in stress can not solely be considered. Figure 5.4 and Table 5.2 show the results from the convergence study. The results indicate

that at a mesh size of 0.07 mm, the equivalent strains are less than 1%. Therefore, a local mesh size of 0.07 mm is applied to the models.

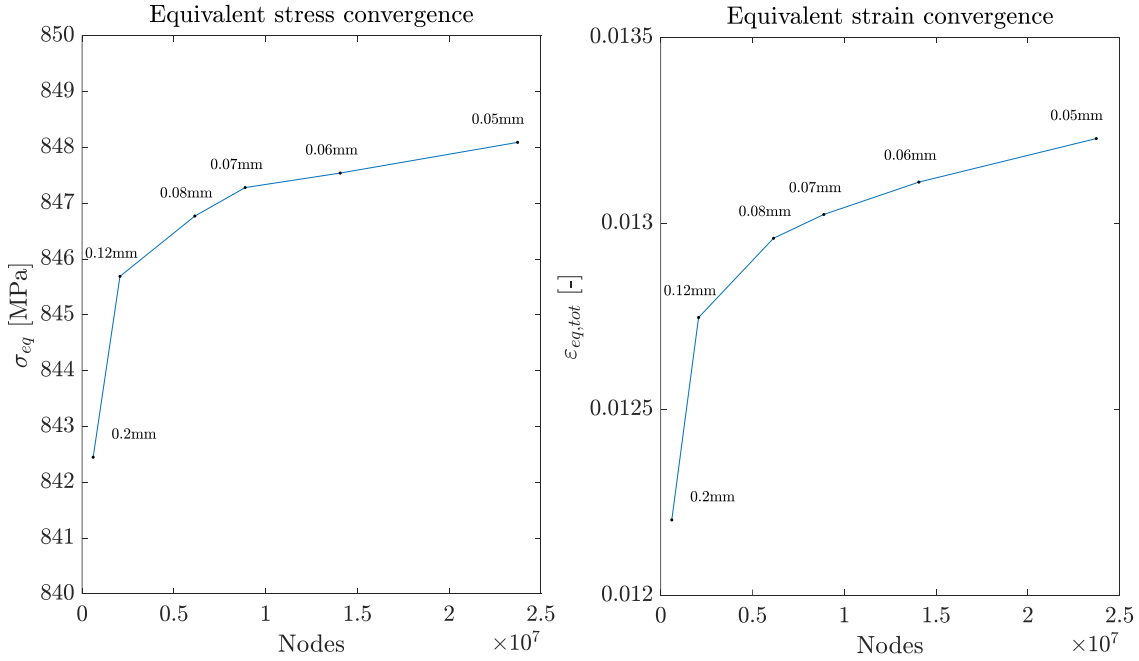


Figure 5.4. Equivalent stress and strain convergence study.

Mesh size [mm]	Nodes	Equivalent stress [MPa]	Percentage difference [%]	Equivalent strain [-]	Percentage difference [%]
0.20	6.04×10^5	842.45		12.20×10^{-3}	
0.12	2.06×10^6	845.69	0.38	12.75×10^{-3}	4.46
0.08	6.15×10^6	846.77	0.13	12.96×10^{-3}	1.67
0.07	8.89×10^6	847.28	0.06	13.02×10^{-3}	0.49
0.06	1.41×10^7	847.54	0.03	13.11×10^{-3}	0.67
0.05	2.37×10^7	848.09	0.06	13.23×10^{-3}	0.89

Table 5.2. Equivalent stress and strain convergence study.

5.4 Global Mesh Convergence Study

Due to the high loading and the applied cyclic material model, the nominal stress at the base material will cause the base material to experience plasticity. As a consequence, the structural stiffness of the model will also change. To ensure that this effect is captured, a mesh convergence study is conducted for the global mesh. This is necessary, as the change in the element tangent stiffness depends on whether the Gauss point of the element experiences stresses greater than the yield strength. If the first surface element does not have Gauss point which captures the plasticity, the element tangent stiffness will not change. Thus, a mesh convergence study is required for the global mesh of the base material.

The mesh convergence study is based on an idealised 2D plane stress weld, shown in Figure 5.5, with a nominal thickness of 6 mm and yield strength of 690 MPa. To examine

the effects of increasing plasticity, both the applied load and the size of the global mesh are considered. Based on Equation (5.6), an analytical expression for the plastic depth in the thickness direction can be evaluated and compared to the placement of the Gauss points. It is thus possible to evaluate the number of Gauss points necessary for the structural response of the base material to have converged for the weld toe.

$$\sigma = \frac{M y}{I} \quad (5.6)$$

To measure the number of Gauss point within the plastic zone, a set of elements through the thickness are evaluated, as illustrated in Figure 5.5 by the red dots which are the Gauss points.

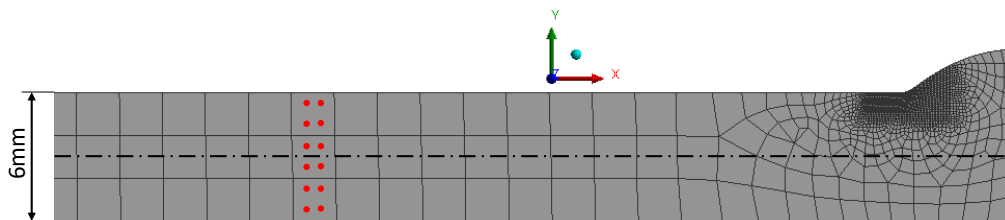


Figure 5.5. Sectional cut of profile view of idealised weld profile. Red dot represent the Gauss points through the thickness.

Figure 5.6 and Table 5.3 shows the result from the mesh convergence study. It is shown that at 29% cross sectional yielding, at least 4 Gauss points, two on either side of the neutral axis, is needed to capture the structural effects of the base material for the strain at the weld toe to converge. However, at 42% cross sectional yielding, 8 Gauss points are needed, i.e. an entire element on either side of the neutral axis must be within the plastic zone.

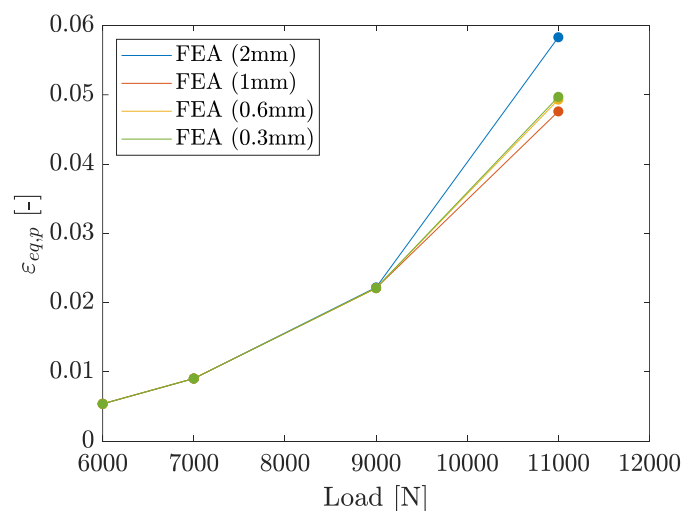


Figure 5.6. Global mesh convergence study.

It can thus be concluded that the global mesh at the base material, which is subjected to loading, must have at least an entire element within the plastic zone on either side of the neutral axis. It should be noted that the quadrilaterals are used for the study, but the global

mesh of the welded specimens will be modelled using tetrahedron to easily conform to the adaptive sizing in the transition to the finer mesh at the weld toe. However, tetrahedron are simply collapsed quadrilaterals (ANSYS, 2023b, Ch. 12.2). Thus, the location of the Gauss points from the surface will be the same. The final mesh is shown in Figure 5.3.

Applied load	F [N]	6000	7000	9000	11000
Analytical	Distance from surface to plastic zone [mm]	-	0.27	0.87	1.26
	Cross sectional yielding [%]	0	9	29	42
FEA (2mm)	No. of Gauss points within plastic zone	0	0	4	4
	Max plastic strain [-]	5.40E-03	9.05E-03	2.22E-02	5.83E-02
FEA (1mm)	No. of Gauss points within plastic zone	0	0	8	8
	Max plastic strain [-]	5.40E-03	9.05E-03	2.21E-02	4.76E-02
FEA (0.6mm)	No. of Gauss points within plastic zone	0	4	12	16
	Max plastic strain [-]	5.40E-03	9.06E-03	2.21E-02	4.93E-02
FEA (0.3mm)	No. of Gauss points within plastic zone	0	8	24	32
	Max plastic strain [-]	5.40E-03	9.05E-03	2.21E-02	4.97E-02

Table 5.3. Analytical calculation for expected size of plastic zone. No. of Gauss points for the element highlighted in Figure 5.5 and the maximum equivalent plastic strain for each load and mesh size.

5.5 Post-processing of Finite Element Analysis

With the finite element models of all laser scanned specimens set up as presented in Sections 5.1 to 5.4 the simulations of all specimens are executed.

Run Time

In general the run time of each FEM is strongly influenced by the loading. An increase in loading also yields an increase in run time as the amount of plasticity causing the non-linearity to increase, requiring more iterations for convergence. The models are executed on a consumer-grade AMD Ryzen 7 5700x (4.8 GHz) processor with 8 logical cores and 32 GB RAM. The computational time varied from 24 min to 4.4 hours with an average run time of 52 min. In writing and exporting the data, the time is roughly doubled. The resulting simulations occupy a total of 315.1 GB of which 19.9 GB are exported result files.

Exporting Nodal Results

The results are exported for further processing. The exported nodal results are obtained by defining named selections in ANSYS Mechanical that contain all area (surface) and all volume nodes of the weld toe as shown in Figure 5.7. With this, all nodes belonging to both the defined area and volume are known and results can be exported.

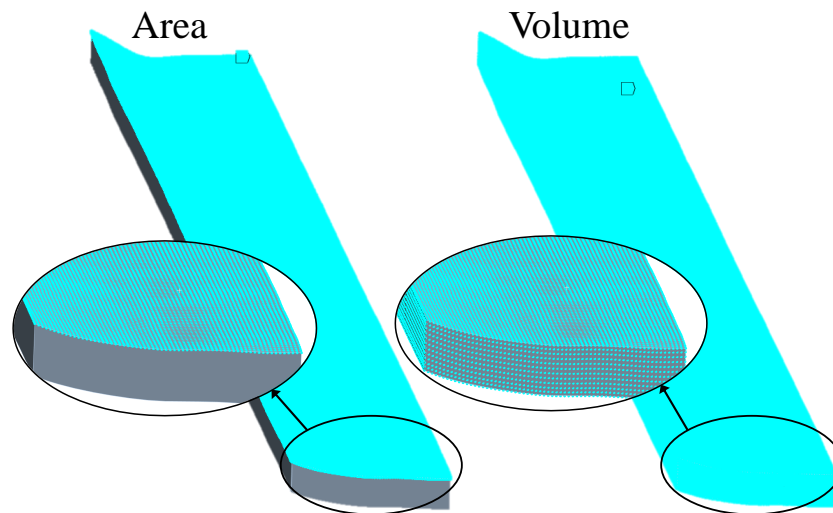


Figure 5.7. Exported area (surface) and volume nodes.

All nodal values in the area and volume are exported, including their location, displacement, stress tensor, elastic strain tensor, and plastic strain tensor. The results are imported into MATLAB for post-processing. This is shown for a single specimen in Figure 5.8, where the equivalent stress from both ANSYS and MATLAB are shown.

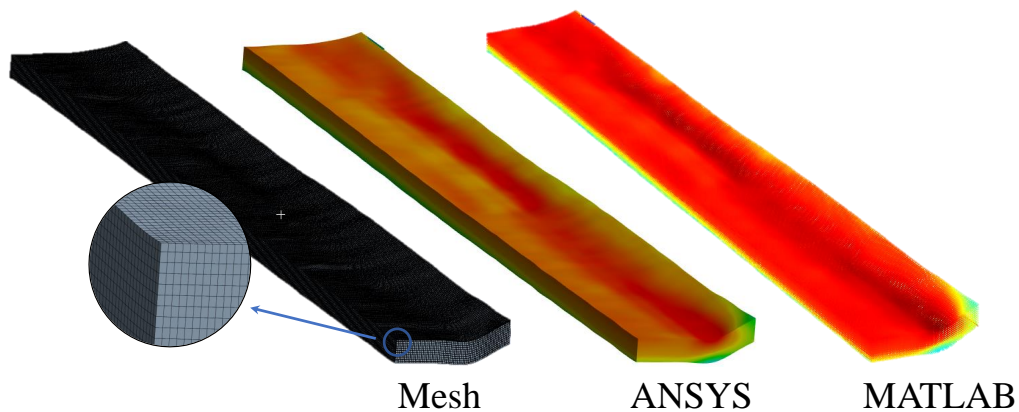


Figure 5.8. Nodal results imported in MATLAB and equivalent stress from both ANSYS and MATLAB.

Nodal Values of Area and Volume

The fatigue indicators, presented in Section 2.5, are computed on a nodal basis. In order to apply the highly stressed volume and -area models, it is required that the area and volume associated with the node is also known. This is implemented by considering the area and volume of a given element and dividing its value by the number of corner nodes as illustrated in Figure 5.9. A node neighbouring several elements will have the sum of the associated element's nodal volume. Using the same approach, the area of each node is computed by considering nodes belonging to an element face.

Only the elements at the weld toe where the mesh is refined are exported, thus the elements

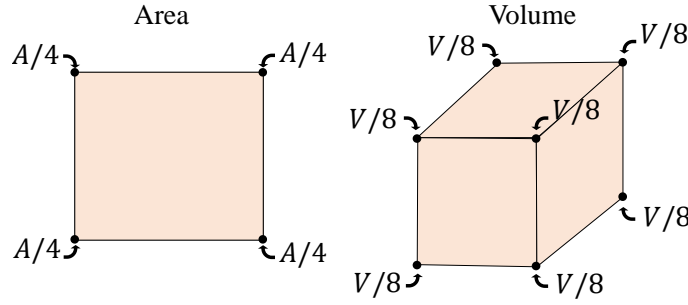


Figure 5.9. Element area and volume divided into nodal area and volume.

have a low shape distortion. Hence allowing for this method of distributing the element area and volume. For a general case, including highly distorted elements, a numerical integration is required.

Nonlocal Models

With the area and volume nodal values known, the fatigue performance based on both the local (peak) and nonlocal models can be evaluated. The peak values are simply the maximum nodal value of the fatigue indicator. For some fatigue indicators the maximum nodal value is located on the surface of the specimen while for other indicators the maximum is located in the volume. To ensure comparability of results, all peak values are recorded on the surface of each specimen. This means that some specimens may potentially have larger values in the volume, which are not included.

The highly stressed regions are computed as presented in Section 2.5.1. The reference volume V_0 and area A_0 are computed based on the mean specimen volume and -area respectively.

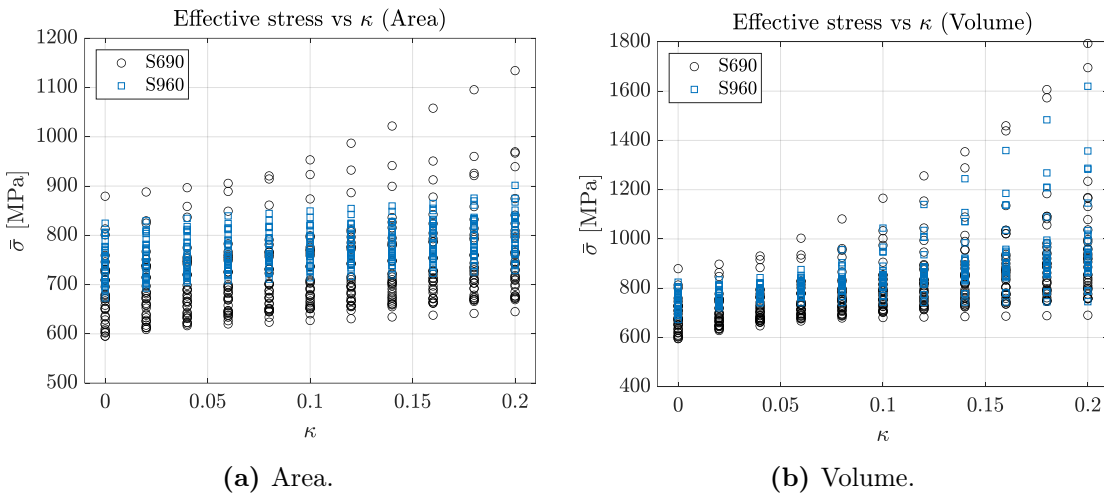


Figure 5.10. Varying κ and computation of effective stress $\bar{\sigma}$ values.

For all fatigue indicators the nodes with values above 90% of the peak value are found and their total area and volume recorded. The κ exponent is varied to minimise the COV. This is done separately for area and volume. In the following, results are presented

for the effective stress, but the procedure is identical for other fatigue indicators. The effective stress $\bar{\sigma}$ is computed based on Equation (2.23) and shown for varying κ values in Figure 5.10. The corresponding COV is shown for different value of κ in Figure 5.11. Note that the coarse sampling of κ is for visual purposes.

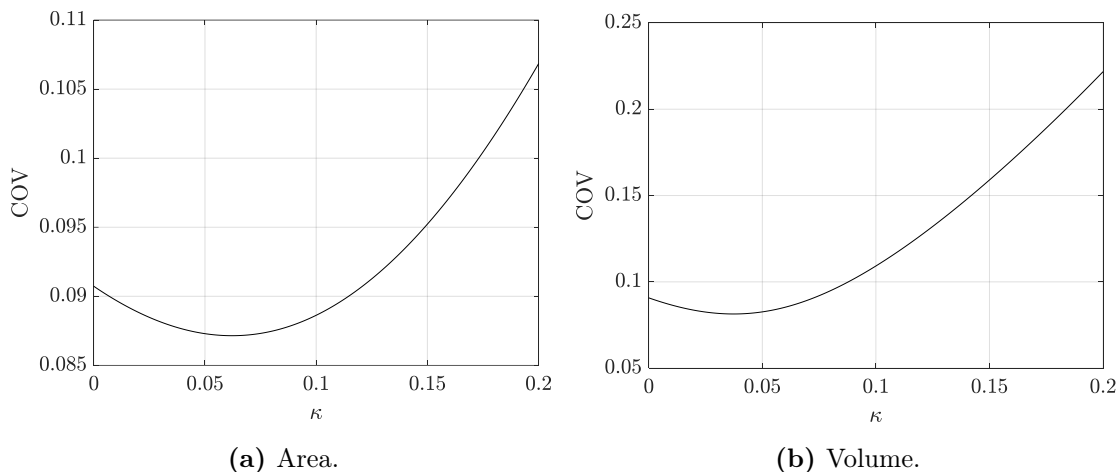


Figure 5.11. Variation of COV with varying κ .

A perk of the nonlocal model considered, is that the phenomena of the *size effect* is apparent (Kuguel, 1960a). Larger sized specimens will experience a decrease in fatigue strength as the stressed volume is increased (Stephens et al., 2001, Ch. 4.4.2). If written in terms of the effective stress, then an increase of the effective stress is expected as the stressed volume is increased. This exact trend is captured for the specimens as shown in Figure 5.12.

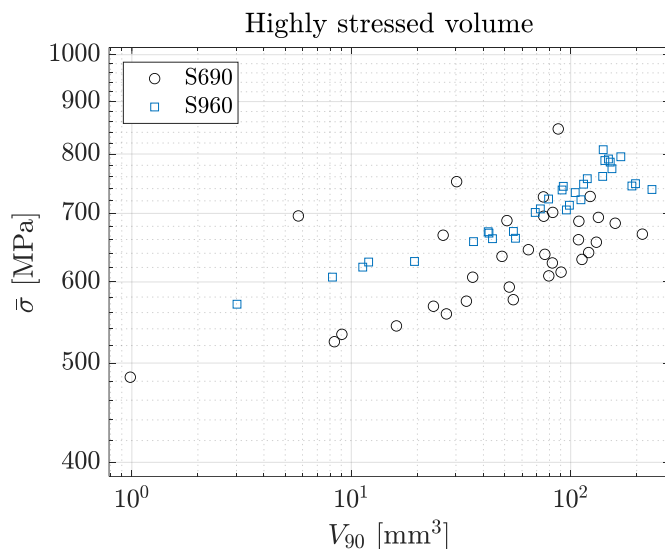


Figure 5.12. Effective stress against the highly stressed volume.

Similarly to the presented procedure, the remaining fatigue indicators are treated using the highly stressed volume and -area approach to account for the effect of the local weld geometry on the fatigue strength.

Nominal Stress and Strain

The nominal true stress and strain are calculated at a specific point on the lower surface of the xz -symmetry plane within the region of constant moment on the side of fracture, as illustrated in Figure 5.13. This calculation yields a clearly defined nominal true stress free of the geometrical influence from the weld. The nominal stress shown in Figure 1.1 is calculated by the means described here.

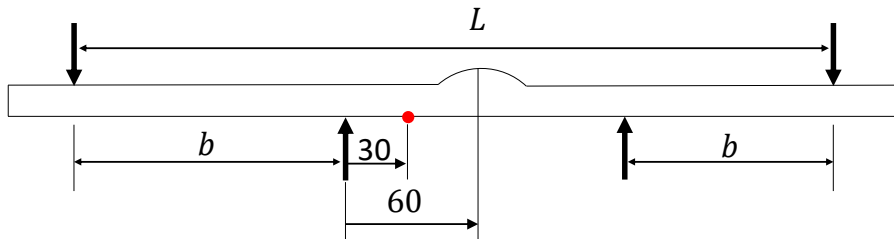


Figure 5.13. Location of nominal measurement. Units in mm. $b = 65$ mm, $L = 250$ mm.

6 Results of Uncertainty Study

This chapter establishes a baseline for comparison for the investigated fatigue indicators and produce the results from the finite element- and statistical analysis.

6.1 Baseline

In order to evaluate each method individually, it is beneficial to form a baseline of comparison for the fatigue indicators. In the following, a baseline based on the nominal stress and nominal strain are used to evaluate the quality of each method. The nominal stress is considered due to its common usage as mentioned in Section 2.1, while the nominal strain is considered due to the non-linear material behaviour of the model. For a method to be considered acceptable it should be able to reduce the scatter and uncertainty of the fatigue results compared to the nominal approaches.

Metric and Measurement of Uncertainty Table

The metrics and measurements of uncertainty used to compare each fatigue indicator and model are presented in Table 6.1. Table 6.1 serves as a summary for the reader for each variable. All variables within **Basquin Eq.** relates to the measures of the Basquin equation. **Normal Dist.** are the associated uncertainty from applying a normal distribution. Variables with **Weibull Dist.** relates to the measure of the Weibull distribution and its associated uncertainty measures. Refer to Sections 2.1, 2.3 and 2.4 for detailed explanation of each variable and uncertainty measurement.

		Explanation	Reference	
Basquin	Eq.	A	Slope of the fitted Basquin equation.	Eq. (2.1)
		B	Intersection with life time axis.	Eq. (2.1)
		R^2	Goodness-of-fit for the Basquin equation.	Eq. (2.11)
Normal	Dist.	T_N	Scatter index evaluated using normal distribution.	Eq. (2.9)
		std	Standard deviation for normal distribution.	Eq. (2.10)
		std_{comb}	Shifted standard deviation.	Fig. 2.8
Weibull	Dist.	β	Fitted Weibull slope.	Eqs. (2.3), (2.4), & (2.6)
		λ	Fitted Weibull characteristic life.	Eqs. (2.3), (2.4), & (2.6)
		R^2	Goodness-of-fit for the Weibull distribution fit.	Eq. (2.11)
		T_N	Scatter index evaluated using Weibull distribution.	Eq. (2.9)
		std	Standard deviation for Weibull distribution.	Eq. (2.10)
		std_{comb}	Shifted standard deviation.	Fig. 2.8

Table 6.1. Metrics used to evaluate quality of fatigue indicator.

Based on the fatigue data from S690 and S960, several different approaches can be taken in how the data sets are linked, as discussed in Section 2.3.3. These approaches are repeated in Figure 6.1.

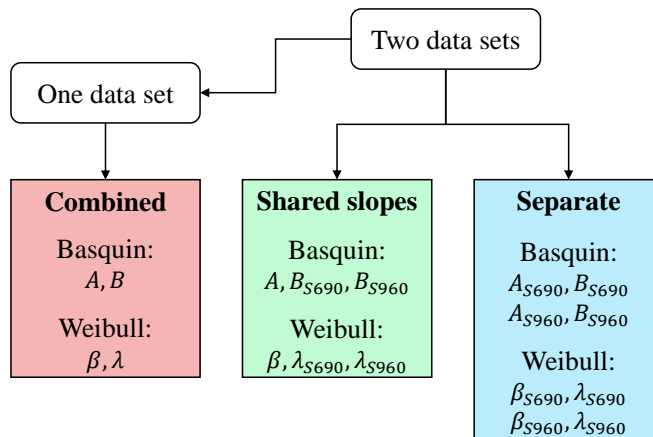


Figure 6.1. Approach for data handling and resulting Basquin and Weibull parameters.

To emphasise the different approaches of data handling, each of the three approaches are computed for the nominal stress and strain. The results of this are shown in Table 6.2. Refer to Table 6.1 for description of each column.

Baseline - Nominal stress and strain													
		Basquin Eq.			Normal Dist.			Weibull Dist.					
		A	B	R^2	T_N	std	std_{comb}	β	λ	R^2	T_N	std	std_{comb}
S690 & S960	σ_{nom}	-7.37	23.91	0.4	20.66	0.51		7.17	3.4	0.96	21.62	0.52	
	ε_{nom}	-2.89	-3.59	0.72	7.82	0.35		11.62	3.53	0.98	7.65	0.35	
S690	σ_{nom}	-11.76	35.76	0.85	4.94	0.27	0.3	11.24	2.82	0.93	5.35	0.29	0.35
	ε_{nom}	-2.87	-3.68	0.81	6.03	0.3	0.33	11.23	3.41	0.92	7.64	0.35	0.36
S960	σ_{nom}	-11.76	36.72	0.67	7.26	0.34		11.24	3.83	0.97	9.8	0.39	
	ε_{nom}	-2.87	-3.42	0.65	7.77	0.35		11.23	3.67	0.98	8.89	0.38	
S690	σ_{nom}	-11.75	35.74	0.85	4.94	0.27	0.3	12.98	3.14	0.94	5.11	0.28	0.33
	ε_{nom}	-2.8	-3.51	0.81	6.01	0.3	0.33	13.24	3.34	0.96	5.5	0.3	0.34
S960	σ_{nom}	-11.78	36.77	0.67	7.26	0.34		10.71	3.42	0.97	8.42	0.37	
	ε_{nom}	-3.02	-3.78	0.65	7.73	0.35		11.45	3.68	0.98	8.6	0.37	

Table 6.2. Nominal stress and strain.

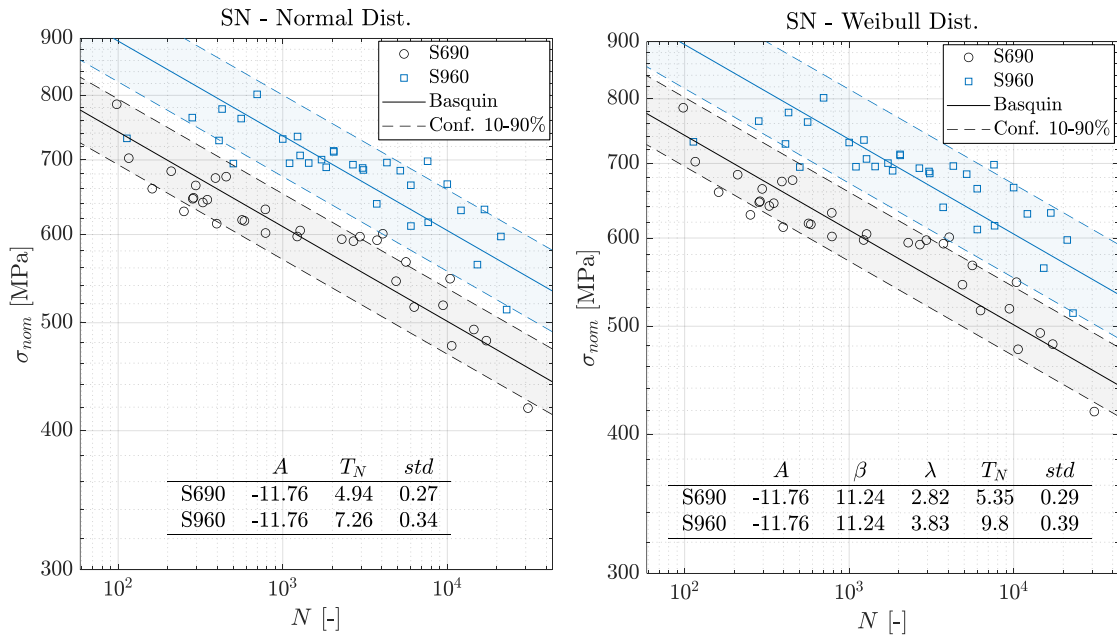
Nominal Baseline

The comparison of results from Table 6.2 is to be conducted column-wise for either the normal or Weibull distribution. A comparison of results between the normal and Weibull distribution does not provide insight into which distribution most accurately details the data.

When initially looking at the nominal stress results in Table 6.2, it is seen that the uncertainty is considerably high when S690 and S960 is evaluated as a single data set in accordance with Hobbacher (2016, Ch. 3.2). When considering the method of shared slopes instead, the uncertainty is lower. The corresponding plots are presented in Figures 6.2a, 6.2b and 6.2e for a normal distribution and a Weibull distribution respectively.

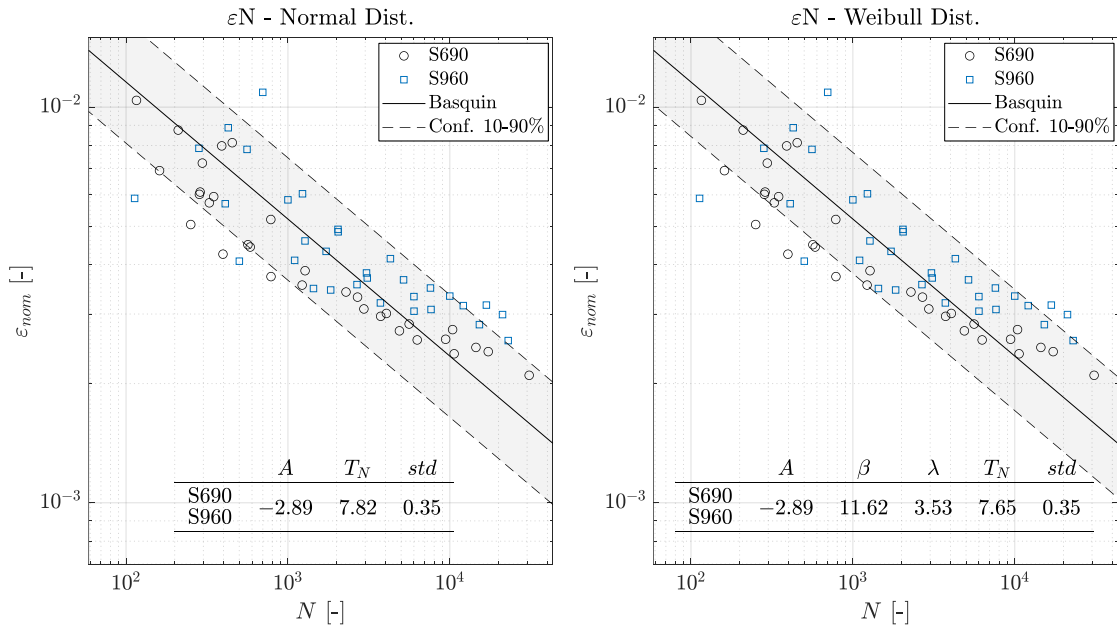
When considering the nominal strain in Table 6.2, improved results, in comparison to the nominal stress, are obtained when S690 and S960 data are combined to a single data set. This is also observed in Figures 6.2c, 6.2d and 6.2f, for the normal- and Weibull distribution respectively.

The nominal baseline is thus established based on Table 6.2. As highlighted, the resulting measures depend on the data handling approach applied.



(a) Nominal stress with normal distribution.

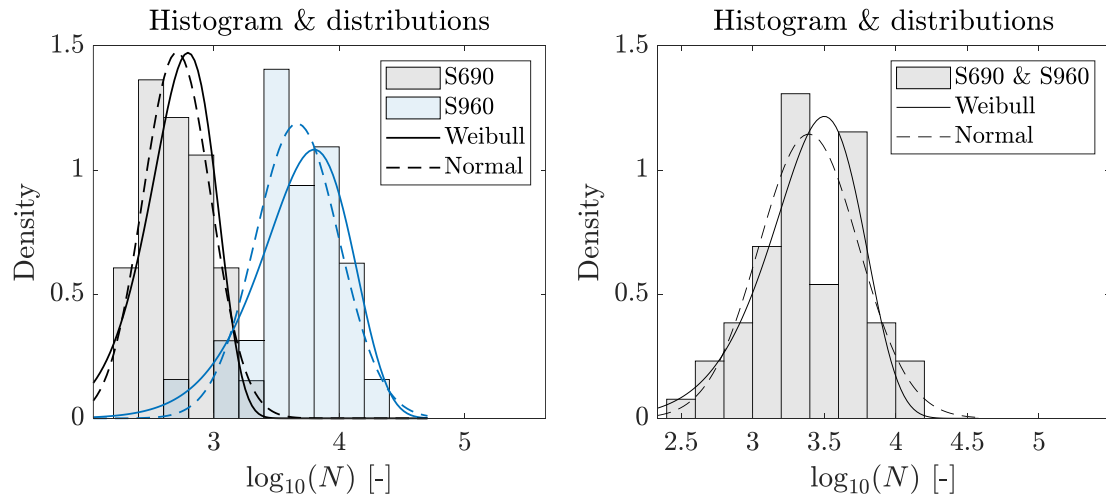
(b) Nominal stress with Weibull distribution.



(c) Nominal strain with normal distribution.

(d) Nominal strain with Weibull distribution.

Figure 6.2. Nominal stress and strain with confidence limits computed with normal and Weibull distribution.



(e) Histogram for nominal stress.

(f) Histogram for nominal strain.

Figure 6.2. Nominal stress and strain histograms.

6.2 Uncertainty Results of Fatigue Indicators

In this section the results for the investigated fatigue indicators from Section 2.5 are presented. The results are presented in tables according to the flow chart in Figure 6.1. As such, each of the fatigue indicators are treated for three different data handling approaches. In the tables, P is used to indicate a peak value of the indicator. A and V are used to indicate, that a nonlocal model of respectively area and volume has been used.

In Table 6.3 the results of the approach of a single data set is presented. In Tables 6.4 and 6.5 the results of the approach of shared Basquin and Weibull slopes are presented. Lastly, in Tables 6.6 and 6.7 the approach of separate data sets are presented. For all tables, the corresponding results of using the nominal stress and strain are additionally also shown.

Similar to Table 6.2, the comparison of results is to be conducted column-wise for either the normal or Weibull distribution and not between each distribution.

		Combined Data Set									
		Basquin Eq.			Normal Dist.		Weibull Dist.				
		A	B	R^2	T_N	std	β	λ	R^2	T_N	std
σ_{nom}		-7.37	23.91	0.4	20.66	0.51	7.17	3.4	0.96	21.62	0.52
ε_{nom}		-2.89	-3.59	0.72	7.82	0.35	11.62	3.53	0.98	7.65	0.35
σ_{eq}	P	-10.42	32.95	0.39	20.84	0.51	7.25	3.43	0.96	21.45	0.52
	A	-9.59	30.46	0.42	19.57	0.5	7.31	3.41	0.96	20.75	0.52
	V	-9.3	29.52	0.5	15.63	0.47	7.92	3.42	0.96	16.85	0.48
σ_{AMP}	P	-10.6	33.97	0.54	13.96	0.45	8.39	3.39	0.98	14.22	0.45
	A	-9.84	31.53	0.51	15.2	0.46	8.05	3.38	0.97	15.59	0.47
	V	-8.3	26.87	0.64	10.31	0.4	9.06	3.27	0.97	10.81	0.41
τ_{max}	P	-10.74	31.09	0.52	14.92	0.46	8.13	3.38	0.97	15.24	0.47
	A	-9.28	27.05	0.5	15.7	0.47	7.94	3.38	0.97	16.19	0.48
	V	-8.46	24.65	0.57	12.85	0.43	8.47	3.35	0.98	13.43	0.44
$\varepsilon_{eq,tot}$	P	-2.6	-2.33	0.81	5.41	0.29	13.98	3.39	0.98	5.15	0.29
	A	-2.49	-3.01	0.72	7.72	0.35	10.82	3.54	0.92	8.86	0.38
	V	-2.49	-3.59	0.73	7.51	0.34	10.93	3.51	0.93	8.55	0.37
ε_{AMP}	P	-2.68	-2.49	0.81	5.4	0.29	14.03	3.38	0.98	5.11	0.28
	A	-2.79	-3.36	0.81	5.44	0.29	13.86	3.53	0.94	5.59	0.3
	V	-2.77	-3.71	0.81	5.45	0.29	13.77	3.49	0.95	5.55	0.3
γ_{max}	P	-2.42	-1.77	0.83	5.1	0.28	14.48	3.39	0.98	4.89	0.28
	A	-2.53	-2.78	0.85	4.6	0.26	15.56	3.49	0.97	4.59	0.27
	V	-2.5	-3.22	0.85	4.55	0.26	15.71	3.51	0.96	4.57	0.27
Y	P	-5.21	3.43	0.39	20.84	0.51	7.25	3.43	0.96	21.45	0.52
	A	-5.21	3.43	0.39	20.85	0.51	7.24	3.42	0.96	21.47	0.52
	V	-5.17	3.35	0.4	20.53	0.51	7.2	3.4	0.96	21.29	0.52
w	P	-3.07	3.78	0.59	12.1	0.42	9.37	3.49	0.97	11.78	0.42
	A	-1.57	3.94	0.48	16.7	0.48	8.16	3.5	0.99	16.55	0.48
	V	-1.62	4.2	0.49	16.29	0.47	8.29	3.48	0.99	15.73	0.47

Table 6.3. Combined data sets for S690 and S960. The best performing fatigue indicator is indicated.

		Shared Slopes - S690											
		Basquin Eq.			Normal Dist.			Weibull Dist.					
		A	B	R^2	T_N	std	std_{comb}	β	λ	R^2	T_N	std	std_{comb}
σ_{nom}		-11.76	35.76	0.85	4.94	0.27	0.3	11.24	2.82	0.93	5.35	0.29	0.35
ε_{nom}		-2.87	-3.68	0.81	6.03	0.3	0.33	11.23	3.41	0.92	7.64	0.35	0.36
σ_{eq}	P	-16.96	51.1	0.79	6.7	0.32	0.3	11.06	2.87	0.89	5.65	0.3	0.36
	A	-15.78	47.52	0.87	4.51	0.26	0.25	13.13	2.8	0.93	4.22	0.25	0.3
	V	-13.6	41.24	0.9	3.84	0.23	0.22	15.02	2.88	0.93	3.67	0.23	0.27
σ_{AMP}	P	-13.57	42.21	0.82	5.74	0.3	0.29	11.85	2.97	0.95	5.38	0.29	0.33
	A	-13.91	42.8	0.87	4.41	0.25	0.24	13.63	2.86	0.87	4.12	0.25	0.29
	V	-10.1	31.65	0.9	3.68	0.22	0.21	15.13	2.83	0.96	3.56	0.22	0.25
τ_{max}	P	-14.55	40.58	0.85	5.16	0.28	0.27	12.52	2.91	0.94	4.78	0.27	0.31
	A	-13.26	36.81	0.86	4.71	0.26	0.25	13.23	2.86	0.91	4.29	0.25	0.3
	V	-10.99	30.67	0.87	4.62	0.26	0.24	13.53	2.88	0.94	4.22	0.25	0.29
$\varepsilon_{eq,tot}$	P	-2.58	-2.3	0.81	6.29	0.31	0.29	12.41	3.39	0.91	6.29	0.32	0.32
	A	-2.46	-3.05	0.73	8.68	0.37	0.33	10.17	3.44	0.9	9.48	0.39	0.4
	V	-2.47	-3.66	0.75	8.1	0.35	0.32	10.42	3.4	0.9	8.77	0.37	0.39
ε_{AMP}	P	-2.66	-2.46	0.8	6.31	0.31	0.29	12.4	3.39	0.91	6.28	0.32	0.32
	A	-2.75	-3.35	0.8	6.43	0.32	0.28	12.58	3.46	0.88	6.38	0.32	0.33
	V	-2.73	-3.71	0.81	6.25	0.31	0.27	12.65	3.41	0.88	6.14	0.32	0.32
γ_{max}	P	-2.41	-1.75	0.82	5.87	0.3	0.28	12.85	3.4	0.92	5.95	0.31	0.31
	A	-2.49	-2.76	0.85	5.06	0.27	0.25	14.25	3.44	0.92	5.12	0.28	0.29
	V	-2.47	-3.21	0.86	4.88	0.27	0.25	14.52	3.45	0.92	5	0.28	0.29
Y	P	-8.48	3.07	0.79	6.7	0.32	0.3	11.06	2.87	0.89	5.65	0.3	0.36
	A	-8.52	3.06	0.8	6.54	0.32	0.29	11.15	2.85	0.89	5.53	0.3	0.35
	V	-8.64	2.92	0.83	5.66	0.29	0.27	11.85	2.78	0.88	4.82	0.27	0.33
w	P	-3.09	3.63	0.64	12.08	0.42	0.39	9.25	3.35	0.92	10.99	0.41	0.43
	A	-1.53	3.87	0.54	16.95	0.48	0.48	7.53	3.48	0.98	20.25	0.51	0.52
	V	-1.58	4.12	0.55	16.16	0.47	0.47	7.59	3.47	0.97	19.62	0.51	0.51

Table 6.4. Separate data sets for S690 with shared Basquin and Weibull slopes. The best performing fatigue indicator is indicated.

Shared Slopes - S960											
		Basquin Eq.			Normal Dist.		Weibull Dist.				
		A	B	R^2	T_N	std	β	λ	R^2	T_N	std
σ_{nom}		-11.76	36.72	0.67	7.26	0.34	11.24	3.83	0.97	9.8	0.39
ε_{nom}		-2.87	-3.42	0.65	7.77	0.35	11.23	3.67	0.98	8.89	0.38
σ_{eq}	P	-16.96	52.08	0.79	4.86	0.27	11.06	3.89	0.91	10.49	0.41
	A	-15.78	48.54	0.82	4.35	0.25	13.13	3.86	0.93	7.25	0.34
	V	-13.6	42.15	0.86	3.66	0.22	15.02	3.82	0.94	5.63	0.3
σ_{AMP}	P	-13.57	42.95	0.78	5.03	0.27	11.85	3.73	0.95	8.28	0.37
	A	-13.91	43.67	0.84	3.89	0.23	13.63	3.75	0.94	6.43	0.32
	V	-10.1	32.35	0.87	3.39	0.21	15.13	3.55	0.96	4.91	0.28
τ_{max}	P	-14.55	41.39	0.81	4.58	0.26	12.52	3.75	0.95	7.49	0.35
	A	-13.26	37.69	0.84	3.95	0.23	13.23	3.76	0.92	6.8	0.33
	V	-10.99	31.45	0.86	3.65	0.22	13.53	3.68	0.92	6.28	0.32
$\varepsilon_{eq,tot}$	P	-2.58	-2.25	0.8	4.62	0.26	12.41	3.43	0.97	6.43	0.32
	A	-2.46	-2.83	0.76	5.48	0.29	10.17	3.68	0.87	11.09	0.41
	V	-2.47	-3.42	0.77	5.27	0.28	10.42	3.66	0.86	10.39	0.4
ε_{AMP}	P	-2.66	-2.41	0.8	4.59	0.26	12.4	3.43	0.96	6.43	0.32
	A	-2.75	-3.18	0.85	3.87	0.23	12.58	3.64	0.9	7	0.34
	V	-2.73	-3.52	0.85	3.86	0.23	12.65	3.61	0.91	6.82	0.33
γ_{max}	P	-2.41	-1.71	0.81	4.43	0.25	12.85	3.43	0.97	6.04	0.31
	A	-2.49	-2.62	0.86	3.71	0.22	14.25	3.59	0.93	5.5	0.3
	V	-2.47	-3.06	0.85	3.74	0.22	14.52	3.61	0.93	5.39	0.29
Y	P	-8.48	4.05	0.79	4.86	0.27	11.06	3.89	0.91	10.49	0.41
	A	-8.52	4.05	0.8	4.75	0.26	11.15	3.88	0.91	10.26	0.4
	V	-8.64	3.95	0.83	4.12	0.24	11.85	3.85	0.89	8.83	0.38
w	P	-3.09	3.95	0.61	8.62	0.36	9.25	3.67	0.97	13.75	0.45
	A	-1.53	3.98	0.34	16.5	0.47	7.53	3.58	0.98	22.04	0.53
	V	-1.58	4.23	0.34	16.55	0.48	7.59	3.56	0.97	21.21	0.52

Table 6.5. Separate data sets for S960 with shared Basquin and Weibull slopes. The best performing fatigue indicator is indicated.

Separate Data Sets - S690													
Basquin Eq.				Normal Dist.			Weibull Dist.						
		A	B	R^2	T_N	std	std_{comb}	β	λ	R^2	T_N	std	std_{comb}
σ_{nom}		-11.75	35.74	0.85	4.94	0.27	0.3	12.98	3.14	0.94	5.11	0.28	0.33
ε_{nom}		-2.8	-3.51	0.81	6.01	0.3	0.33	13.24	3.34	0.96	5.5	0.3	0.34
σ_{eq}	P	-15.13	45.91	0.8	6.35	0.31	0.27	11.87	3.26	0.96	6.32	0.32	0.28
	A	-14.75	44.61	0.87	4.4	0.25	0.24	14.73	3.16	0.98	4.28	0.25	0.26
	V	-13.27	40.31	0.9	3.82	0.23	0.22	16.06	3.14	0.96	3.79	0.23	0.24
σ_{AMP}	P	-12.5	39.15	0.83	5.57	0.29	0.27	12.82	3.27	0.99	5.58	0.3	0.29
	A	-13	40.22	0.88	4.3	0.25	0.23	15.77	3.25	0.98	4.06	0.24	0.24
	V	-9.95	31.23	0.9	3.67	0.22	0.21	16.45	3.16	0.98	3.69	0.23	0.23
τ_{max}	P	-13.47	37.8	0.85	5.01	0.27	0.26	13.55	3.21	0.98	4.95	0.28	0.27
	A	-12.39	34.6	0.87	4.6	0.26	0.24	14.61	3.24	0.98	4.5	0.26	0.25
	V	-10.62	29.75	0.87	4.59	0.26	0.24	14.38	3.25	0.97	4.63	0.27	0.25
$\varepsilon_{eq,tot}$	P	-2.32	-1.76	0.82	5.99	0.3	0.27	12.27	3.25	0.97	5.92	0.31	0.28
	A	-2.26	-2.55	0.74	8.48	0.36	0.32	9.44	3.48	0.91	11.43	0.42	0.36
	V	-2.26	-3.09	0.75	7.89	0.35	0.31	9.82	3.47	0.92	10.42	0.4	0.35
ε_{AMP}	P	-2.39	-1.9	0.81	6.01	0.3	0.27	12.39	3.25	0.97	5.84	0.31	0.28
	A	-2.48	-2.71	0.81	6.15	0.31	0.26	12.01	3.42	0.95	6.77	0.33	0.28
	V	-2.46	-3.03	0.82	5.96	0.3	0.25	12.42	3.43	0.95	6.43	0.32	0.27
γ_{max}	P	-2.19	-1.31	0.83	5.63	0.29	0.26	12.59	3.24	0.97	5.64	0.3	0.27
	A	-2.29	-2.29	0.86	4.89	0.27	0.24	14.01	3.43	0.96	5.25	0.29	0.25
	V	-2.27	-2.71	0.86	4.71	0.26	0.24	14.29	3.43	0.95	5.08	0.28	0.25
Y	P	-7.56	3.07	0.8	6.35	0.31	0.27	11.87	3.26	0.96	6.32	0.32	0.28
	A	-7.61	3.06	0.81	6.2	0.31	0.27	11.97	3.25	0.96	6.2	0.32	0.28
	V	-7.81	2.94	0.84	5.39	0.29	0.25	13.26	3.24	0.98	5.21	0.29	0.26
w	P	-2.63	3.55	0.66	11.25	0.41	0.34	9.1	3.38	0.94	11.6	0.42	0.35
	A	-1.41	3.81	0.54	16.74	0.48	0.47	8.06	3.4	0.99	15.78	0.47	0.48
	V	-1.48	4.05	0.56	16.01	0.47	0.47	8.24	3.37	0.99	14.57	0.46	0.47

Table 6.6. Separate data sets for S690. The best performing fatigue indicator is indicated.

Separate Data Sets - S960											
		Basquin Eq.			Normal Dist.		Weibull Dist.				
		A	B	R^2	T_N	std	β	λ	R^2	T_N	std
σ_{nom}		-11.78	36.77	0.67	7.26	0.34	10.71	3.42	0.97	8.42	0.37
ε_{nom}		-3.02	-3.78	0.65	7.73	0.35	11.45	3.68	0.98	8.6	0.37
σ_{eq}	P	-23.01	69.46	0.85	3.82	0.23	17.31	3.5	0.97	3.98	0.24
	A	-18.29	55.73	0.83	4.08	0.24	15.07	3.38	0.97	4.58	0.27
	V	-14.19	43.84	0.86	3.63	0.22	16.36	3.36	0.97	4.06	0.24
σ_{AMP}	P	-16.42	51.27	0.8	4.59	0.26	14.31	3.43	0.98	5.07	0.28
	A	-16.02	49.8	0.86	3.64	0.22	17.61	3.44	0.98	3.8	0.23
	V	-10.35	33.06	0.88	3.38	0.21	17.96	3.39	0.99	3.63	0.23
τ_{max}	P	-17.31	48.6	0.83	4.21	0.24	15.3	3.42	0.97	4.57	0.27
	A	-15.26	42.87	0.86	3.69	0.22	17.27	3.45	0.98	3.91	0.24
	V	-11.66	33.15	0.86	3.6	0.22	17.34	3.43	0.97	3.86	0.24
$\varepsilon_{eq,tot}$	P	-3.38	-4	0.85	3.8	0.23	17.3	3.49	0.97	3.97	0.24
	A	-2.95	-4.06	0.78	5.08	0.28	15.39	3.61	0.96	4.91	0.28
	V	-3	-4.87	0.79	4.82	0.27	15.43	3.6	0.92	4.88	0.28
ε_{AMP}	P	-3.47	-4.19	0.85	3.78	0.23	17.29	3.49	0.97	3.97	0.24
	A	-3.49	-4.95	0.89	3.21	0.2	21.05	3.55	0.96	3.18	0.2
	V	-3.48	-5.43	0.89	3.17	0.2	21.82	3.54	0.95	3.05	0.2
γ_{max}	P	-3.03	-3.03	0.85	3.81	0.23	16.95	3.47	0.97	4.04	0.24
	A	-2.99	-3.83	0.88	3.3	0.2	20.26	3.54	0.94	3.31	0.21
	V	-2.95	-4.32	0.88	3.34	0.2	20.79	3.55	0.94	3.24	0.21
Y	P	-11.51	4.29	0.85	3.82	0.23	17.32	3.5	0.97	3.97	0.24
	A	-11.48	4.28	0.85	3.77	0.22	17.52	3.5	0.97	3.91	0.24
	V	-11.05	4.11	0.87	3.42	0.21	18.86	3.44	0.96	3.49	0.22
w	P	-6.25	4.52	0.82	4.34	0.25	16.91	3.57	0.98	4.22	0.25
	A	-2.15	4.22	0.37	15.44	0.46	8.13	3.53	0.97	17.14	0.49
	V	-2.1	4.51	0.36	15.8	0.47	8.22	3.53	0.97	16.73	0.48

Table 6.7. Separate data sets for S960. The best performing fatigue indicator is indicated.

7 Discussion of Results

In this chapter a discussion of the results presented in Section 6.2 is provided with focus on identifying the best performing fatigue indicators when considering local and nonlocal models for reducing the uncertainty. A well performing fatigue indicator is to be expressed through a low scatter index and standard deviation for the specific indicator, which is direct measure of the quality of the predictor. Additionally, for the Basquin method the coefficient of determination also expresses the quality of the model, while the β parameter in the Weibull model also increases with increasing quality.

Firstly, a comparison between mainly the stress and strain indicators is presented for each of the three approaches presented in Figure 6.1. This is done to evaluate whether or not the inspected method is expected to provide good results. Next, a comparison between each of the three approaches is shown with focus on the difference between the local and nonlocal models evaluating the potential benefit of adapting a nonlocal model. Lastly, a recommendation of the best performing fatigue indicator and model is provided.

7.1 Evaluation of Data Handling Approach

When considering the three different approaches for handling the S690 and S960 fatigue data, presented in Figure 6.1, a study of the results of the approaches is now presented. The focus in the following comparison is on the difference between the different approaches and is not concerned with the potential improvement or reduction in fatigue data scatter when considering local and nonlocal models.

Combined Data Set

When combining the data sets, material differences are purposely ignored in the model, which is the recommended approach for high-cycle fatigue as prescribed by Hobbacher (2016). However, for low-cycle fatigue the material difference is substantially more important as indicated by Table 6.3. The stress based fatigue indicators all exhibit poor predictive capabilities, indicated by large scatter indices and standard deviations, and low R^2 and β for the Basquin equation and Weibull distribution respectively. The energy-based criteria of Lemaitre and strain energy density similarly model the data quite poorly. In contrast to this, the strain indicators all show considerably better predictive aptitude, with several of the indicators showing reduction in the order of three in scatter index in

comparison to their stress counterpart. This applies to the equivalent, maximum principal, and maximum shear strain criteria indicating that this approach of combining weld fatigue data sets irrespective of material may be applicable if strains are considered.

Shared Slopes

Moving to the approach of identical slopes for which results are presented in Tables 6.4 and 6.5, the stress indicators can be seen to be quite capable in reducing the uncertainty of the fatigue data. This is to be expected as the difference in material is now explicitly included in the modelling. The results clearly show the beneficial effect that this has on the stress-based methods which now show an improvement compared to the strain methods. Lemaitre's criterion now also exhibits good predictive capabilities on par with that of the stress.

This approach highlights the effects of the considering different distributions. If the stress criteria are considered, S960 yields lower uncertainty for a normal distribution than for a Weibull distribution. If S690 is considered, the Weibull distribution produces lower uncertainty than the normal distribution. If the strain criteria are considered, the opposite is observed. The strain energy density still yields no better performance than the nominal indicators.

Separate Data Sets

Lastly, when considering the data sets completely separate, the results of which are provided in Tables 6.6 and 6.7, all indicators are expected to provide the best possible reduction in scatter as no assumptions between the data sets are enforced. This is also seen as this approach produces the lowest uncertainty for S960. However, the difference in uncertainty for S690 is still comparable to a shared slope approach. The predictive capabilities of the strain energy density is still poor.

Overall, it seems that the approach of complete data separation warrants the best possible reduction in scatter, and has proved to be substantially better than the corresponding nominal approaches. This indicates that a reduction of the associated fatigue scatter for butt welded joints can be achieved by incorporating the effects of the weld geometry.

7.2 Evaluation of Local and Nonlocal Models

In the following focus is now on the effects of including a nonlocal model in comparison to only looking at the local fatigue indicator and whether improvements can be observed. Based on the principles introduced by Kuguel (1960a) the expected effect is that both the highly stressed area and volume are better at modelling fatigue failure in comparison to the peak value as the size of the region that is heavily loaded is included in the model. This is especially potent when the weld geometry is included as local stress raisers give rise to considerable regions of high stress.

Initial offset is taken in Tables 6.6 and 6.7. This is done to purely evaluate the effect of transitioning from a local to a nonlocal model, without the added influence from combining the data sets of S690 and S960.

Immediately it is seen, that the effects of the nonlocal models are not consistent from indicator to indicator. For some indicators the quality improves when moving from the peak value to area and volume values, and for other indicator the behaviour degrades.

For the stress fatigue indicators the principles of the highly stressed regions seem to be coherent with the obtained results in that an improvement in predictive capabilities is observed when the nonlocal models are utilised. Furthermore, the volume consistently performs better than the area, which is logical as the inclusion of stress gradients in the thickness direction is included. For the strain-based indicators, the resulting effects are split when looking at different indicators. The total strain performance worsens when transitioning to nonlocal modelling, and for the other strain criteria the improvements are less potent than that of the stress indicators. Lastly, for the energy-based criteria the Lemaitre criterion shows minute improvements for the area and volume models, while the strain energy density worsens considerably.

These trend continue when also considering the results for the approach of shared slopes shown in Tables 6.4 and 6.5, and the total combination of data shown in Table 6.3. However, the effects of the restrictions on the Basquin and Weibull slope are also included in the results so the exact cause-effect is unknown.

7.3 Recommendation for Scatter Reduction

Lastly, a recommendation for the most effective fatigue indicator and model at reducing scatter is provided for each of the three data handling approaches of the fatigue data sets of S690 and S960 shown in Figure 6.1.

Combined Data Set

For the combined data set shown in Table 6.3, the maximum shear strain criterion applied using the highly strained volume model provides the least amount of scatter in the fatigue data. The corresponding plots are shown in Figure 7.1 for the confidence intervals provided by the Weibull distribution. Figure 7.1a shows the nominal strain and Figure 7.1b shows reduced uncertainty when changing fatigue indicator. Figure 7.1c shows the histogram of fatigue data and the fitted normal- and Weibull distributions. Figure 7.1d shows a comparison between the predicted lifetime using the Basquin fit, and empirically observed lifetime.

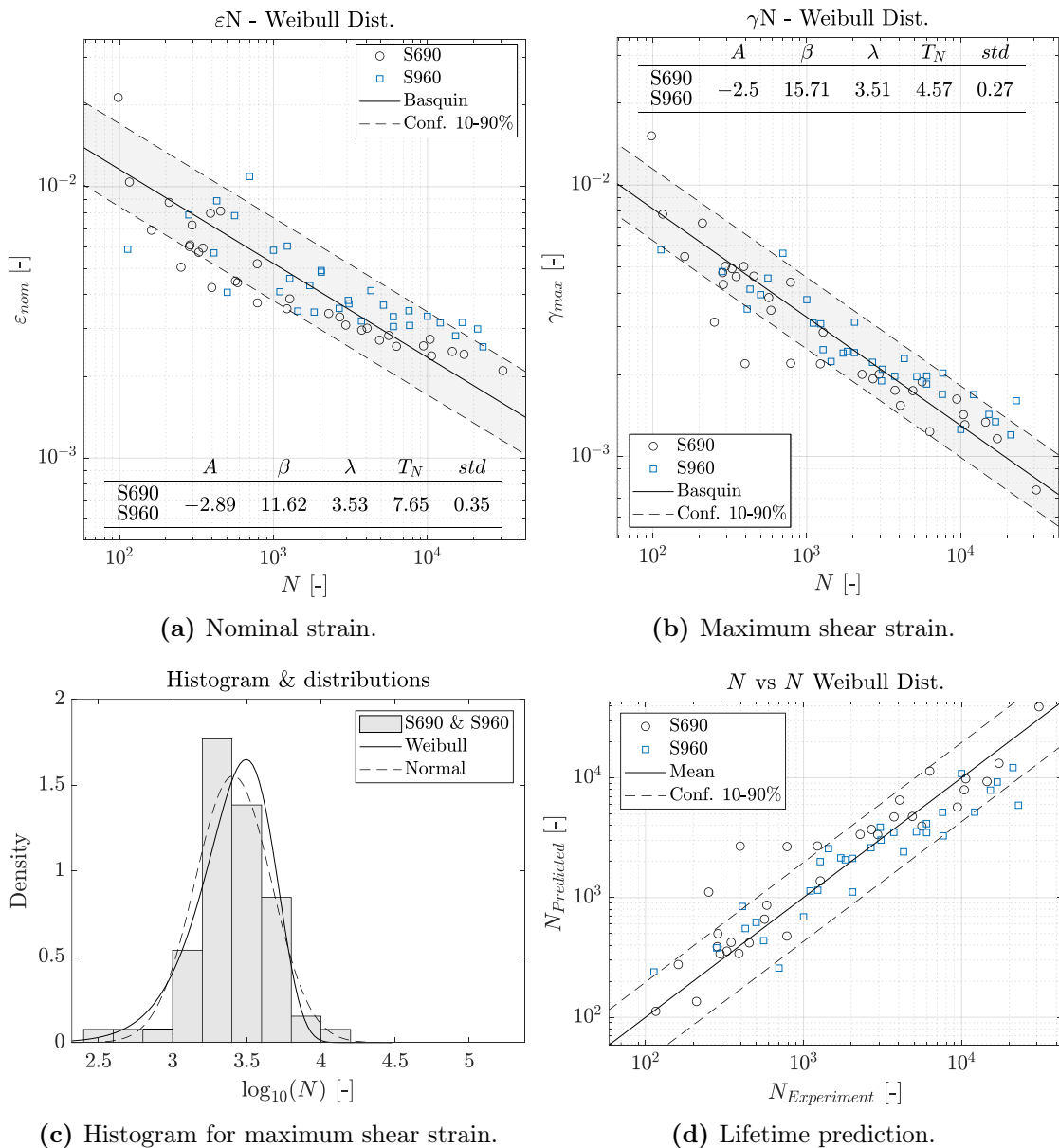


Figure 7.1. Combined fatigue data of maximum shear strain with highly strained volume.

Shared Slopes

When looking at the approach of combining the data sets using shared slopes, the best performing fatigue indicator is the maximum principal stress for a highly stressed volume. Again the model of using a highly stressed volume reduces the scatter considerably in comparison to using the peak values. This emphasises the effect of including the weld geometry. The nominal stress results are shown in Figure 7.2a, while the improved results shown in Figures 7.2b to 7.2d.

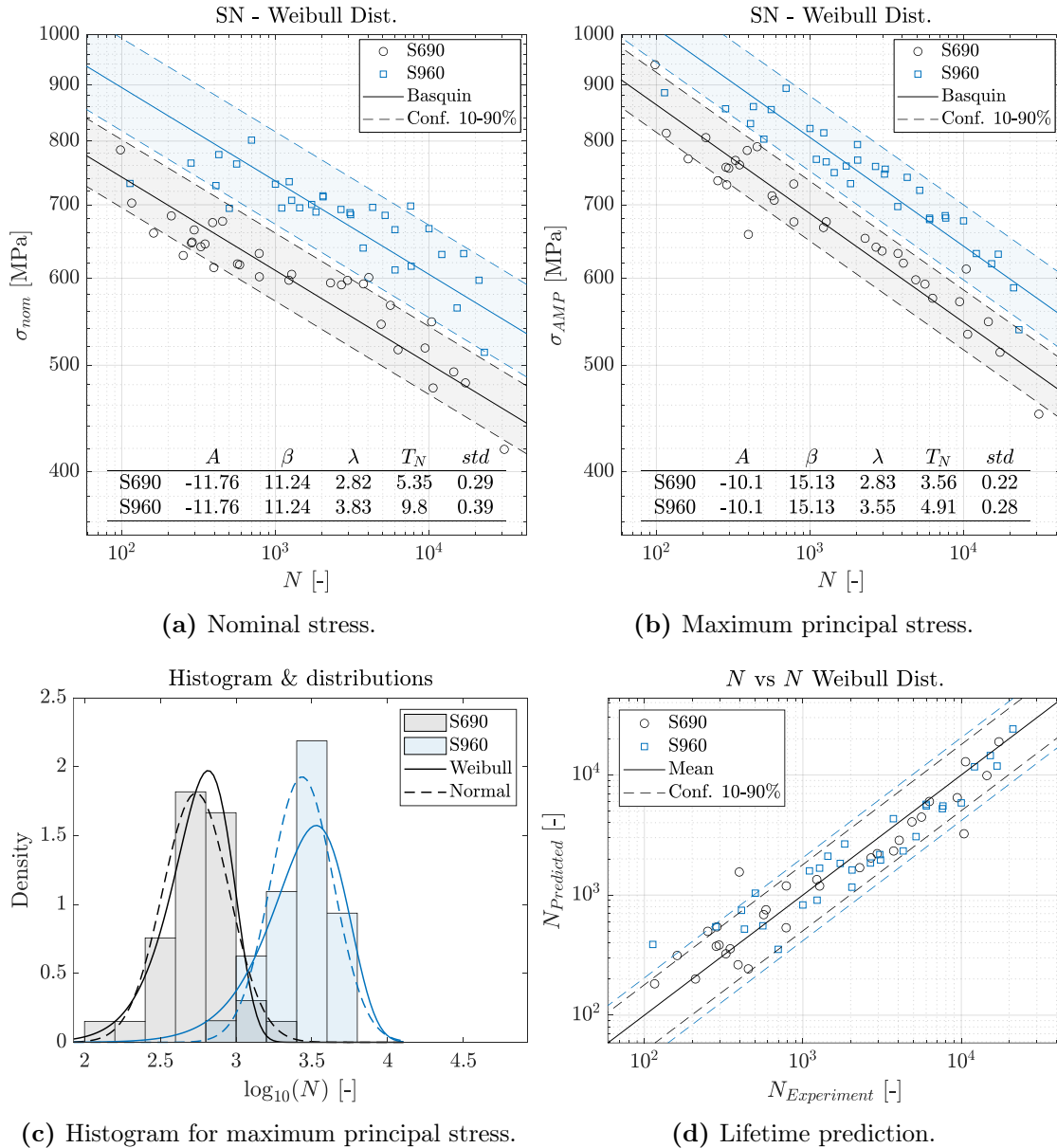


Figure 7.2. Shared slopes fatigue data of maximum principal stress with highly stressed volume.

Separate Data Sets

Lastly, when considering the approach of separating the fatigue data completely, the best fatigue indicator for only the S690 data is the highly stressed volume of the maximum principal stress. When looking at only the S960 data the maximum principal strain with the highly strained volume model provides the least amount of scatter. If the data sets must be evaluated using the same fatigue indicator then the maximum principal stress provides the best compromise. Plots of the maximum principal stress using the highly stressed volume model are shown in Figure 7.3.

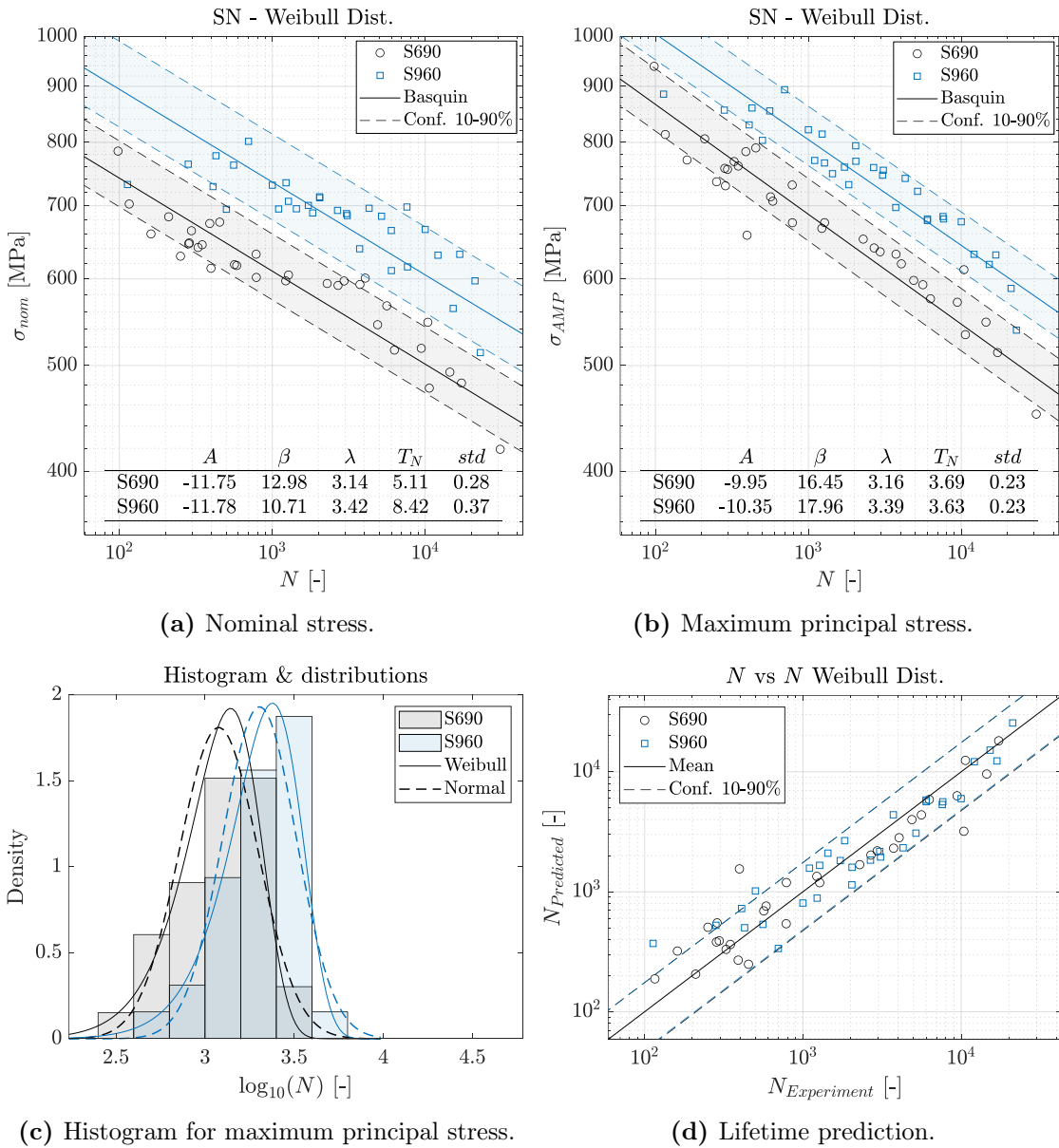


Figure 7.3. Completely separate fatigue data for maximum principal stress using a highly stressed volume model.

Final Remarks

Conclusively, it has been shown in the preceding, that fatigue data of butt welded joints in S690 and S960 can be reduced by modelling the local weld geometry obtained by laser scanning. The fatigue indicator that reduces scatter most is the maximum principal stress using a highly stressed model. For a Weibull distribution, a scatter index of 3.69 and 3.63 is obtained, while the nominal stress approach resulted in higher values of 5.11 and 8.42, respectively. This corresponds to a reduction of 27.8% and 56.9% for S690 and S960 respectively. The standard deviations are reduced by respectively 17.9% and 37.8% for the two data sets respectively.

8 Geometrical Weld Measurements

Having established a method of reducing the uncertainty for fatigue data, the following chapter will detail the methods used for determining the geometrical weld features of the butt weld presented in Section 2.6 and show the resulting distribution of geometrical feature.

8.1 Determination of Geometrical Features

To determine the geometrical features, the location of the weld toe is needed. This is obtained by the weld toe detection method described in Section 4.5 and shown in Figures 4.7 and 4.8.

8.1.1 Weld Toe Radius

As mentioned in Section 2.6, the method for obtaining the radius r is based on the *curvature method* proposed by Schubnell et al. (2019). The basis for this method, is the inverse relation between the curvature κ and radius for a circle. This is shown in Equation (8.1), where T is the tangent vector and c is the arc length.

$$\kappa = \frac{1}{r} = \left\| \frac{\partial T}{\partial c} \right\| \quad (8.1)$$

By including the information of the normal vector n the directional information can be expressed as shown in Equation (8.2).

$$\kappa = n \cdot \frac{\partial T}{\partial c} \quad (8.2)$$

Schubnell et al. (2019) applies this principle analytically by use of spline fitting between data points from the laser scanning process to obtain a piecewise differentiable function for the entire laser scan. However, in this work the method is implemented numerically.

The arc length dc is obtained by Equation (8.3) from the x - and z -data for a given laser profile. As all calculations are evaluated numerically, all gradients are calculated using a central difference approximation¹.

$$dc = \sqrt{\Delta x^2 + \Delta z^2} \quad (8.3)$$

¹The first and last point are evaluated using a backward- and forward difference approach as to not lose any data.

The components of the tangent vector are obtained by differentiating the positional data w.r.t. to the arc length as shown in Equations (8.4) and (8.5).

$$T_x = \frac{dx}{dc} \quad (8.4)$$

$$T_z = \frac{dz}{dc} \quad (8.5)$$

The curvature can thus be calculated using Equation (8.6).

$$\kappa = \sqrt{\left(\frac{dT_x}{dc}\right)^2 + \left(\frac{dT_z}{dc}\right)^2} \quad (8.6)$$

The sign of the curvature can be recovered by evaluating the sign of the cross product between the tangent derivative and normal vector using Equations (8.7) to (8.9).

$$n_x = -T_z \quad (8.7)$$

$$n_z = T_x \quad (8.8)$$

$$\kappa_{sign} = \text{sign} \left(n_x \frac{dT_x}{dc} + n_z \frac{dT_z}{dc} \right) \quad (8.9)$$

By recovering the sign of the curvature, the weld toe radius can be evaluated for only concave positional data, i.e. positive curvature, as shown in Equation (8.10).

$$r_i = \frac{1}{\kappa_i}, \quad \text{if } \kappa_{sign,i} = 1 \quad (8.10)$$

In the study by Renken et al. (2021), it was concluded that a resolution of 0.8 mm, for the xz -points, is necessary to capture representative results of the geometry. As shown in Section 3.2, the experimental setup is well within the recommendations by Renken et al. (2021). However, a piecewise spline interpolation is applied to the laser scans. The evaluation of curvature, and subsequently the radius, is still done numerically. The spline is evaluated at 50 intermediate points between each laser scan point, effectively reducing the x -resolution from 0.093 mm to 1.86×10^{-3} mm.

To automate the selection of the smallest radius at the weld toe, the weld toe detection method from Section 4.5 is applied. The detection method is able to distinguish between the left and right side of the weld toe, and give a set of point which are potential candidates for the smallest radius. By searching for the minimum radius within the region found by the detection method, the weld toe radius is determined. The resulting automated process is shown in Figure 8.1. This figure also highlights the difficulty in automating the selection process of the smallest radius, as it is possible that the smallest radius does not necessarily occur at the weld toe transition, but can occur on top of the weld.

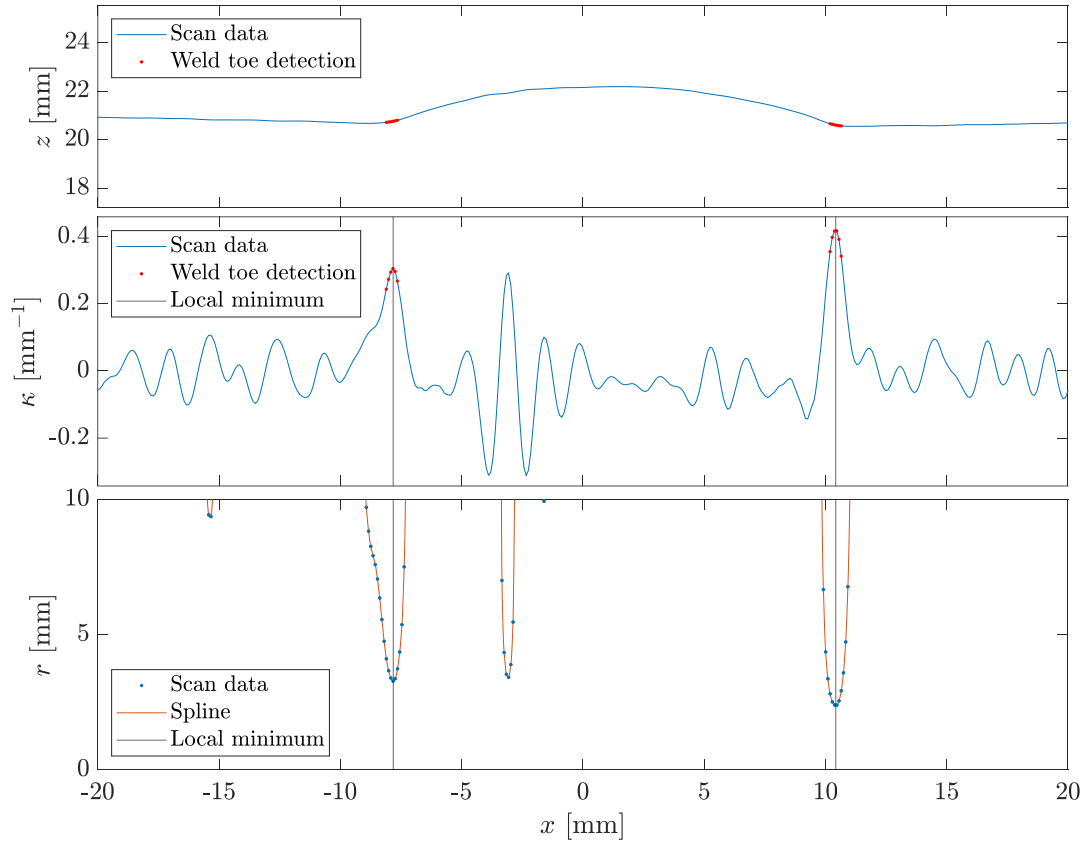


Figure 8.1. Positional, curvature, and radius data for a single laser profile. Note that the axes for the positional data is 1:1.

8.1.2 Weld Toe Angle

As mentioned in Section 2.6, the method for obtaining the weld toe angle α is based on the recommendations proposed by Schubnell et al. (2019), in which the weld toe angle is calculated based on the angle formed between a line in the base material and a line following the weldment.

Schubnell et al. (2019) determines the line for the base material, by simply fitting a line for the base material. The line for the weld is determined by evaluating the tangent at which the weld toe radius ends. However, in this work, the line for the weld will not be determined based on the tangent of the weld toe radius, but instead by the use of the weld toe detection method from Section 4.5. The principle behind finding the angle between two straight lines is still applied.

Based on the weld toe detection method from Section 4.5, the laser scan can be separated into base material and weldment. To ensure that the change in geometry at the weld toe transition, i.e. the undercut and weld toe radius, does not influence the fitting procedure, a fixed number of data points are excluded. This is highlighted in Figure 8.2 where the clearly visible undercut is not included in the fitting procedure.

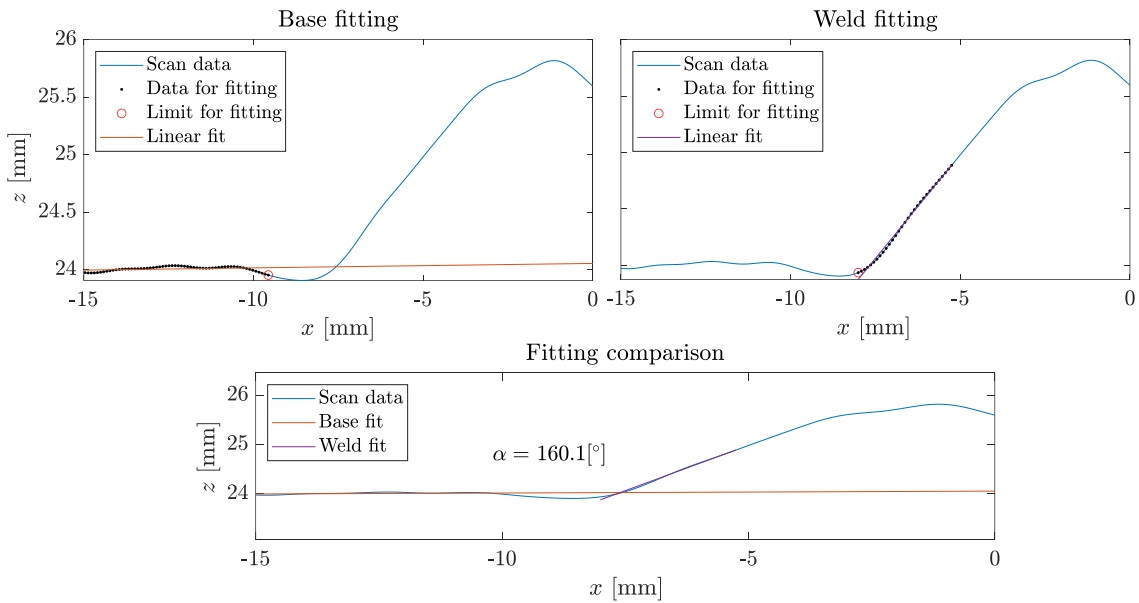


Figure 8.2. Fitting for base material and weld. Note that the axes for the comparison is 1:1.

8.1.3 Undercut

The undercut k is determined by evaluating the difference between the line fit for the base material and the scan data. The interval along the scan data evaluated is the interval excluded in the fitting procedure for the weld toe angle. The base fitting and the calculated undercut is shown in Figure 8.3.

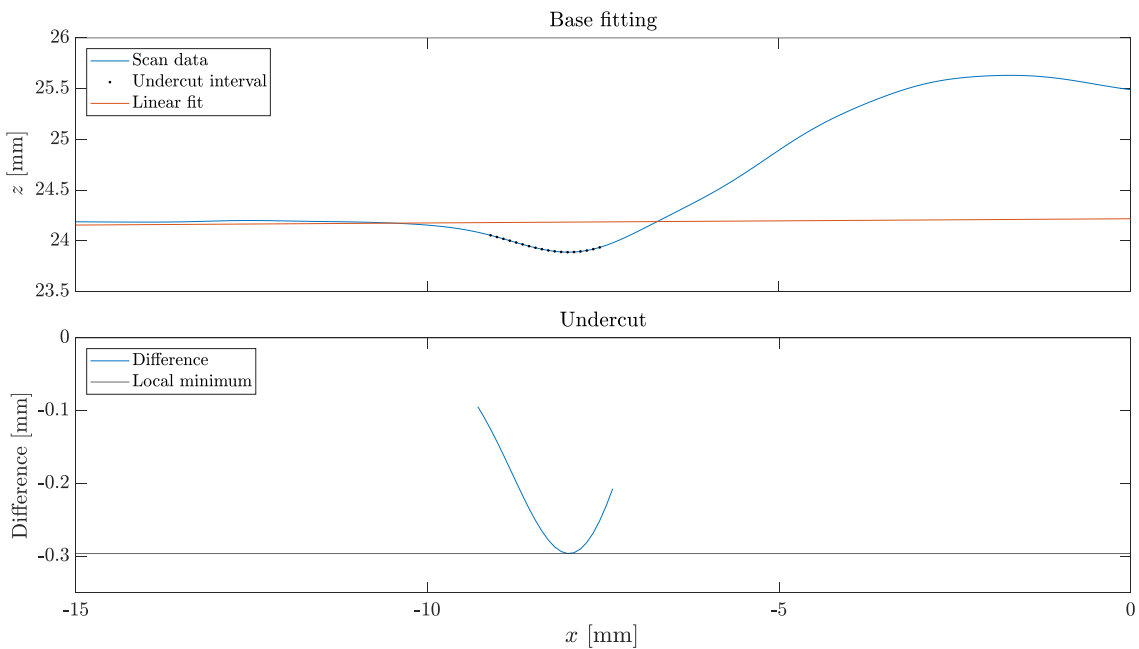


Figure 8.3. Linear fit of base material and calculation of undercut.

8.1.4 Excess Weld Material

Excess weld material h is calculated by evaluating the difference in height between the weld and base material. The height of the base material is evaluated at the location of the weld toe detection as illustrated in Figure 8.4. The excess weld is calculated as the difference between the maximum height and the average of height at each weld toe location as shown in Equation (8.11).

$$h = h_{max} - \left(\frac{h_1 + h_2}{2} \right) \quad (8.11)$$

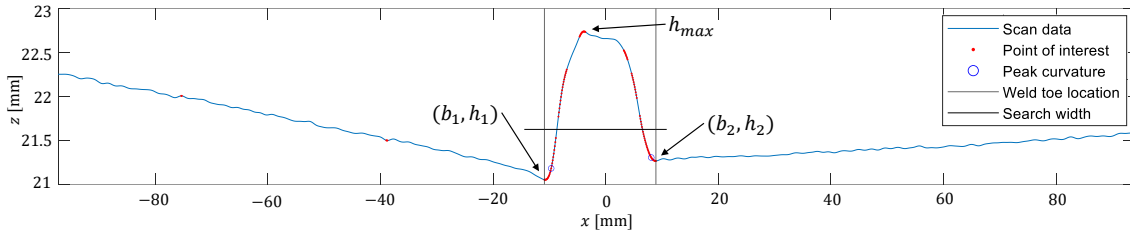


Figure 8.4. Excess weld height and weld width based on the weld detection method.

8.1.5 Weld Width

The width of the weld b is evaluated at the same location as the excess weld height illustrated in Figure 8.4. The width is simply evaluated as the difference between the x -location at each weld toe.

$$b = b_2 - b_1 \quad (8.12)$$

Both the excess weld material and width of the weld are evaluated using the weld detection method from Section 4.5, i.e. where the gradient is zero. This location is different from the location of the weld toe radius, i.e. at maximum curvature. No standard definition of the location at which these geometrical features are to be evaluated is known to the authors².

²DS/EN-ISO-17637 (2016), which specifies the manual inspection of welded joints, provides no insight to the location of where the measurements are to be conducted.

8.2 Distribution of Weld Features

Due to time constraints, no validation of the methods employed has been conducted. Ideally, predetermined idealised geometries would be constructed from which the methods for determining the geometrical features could be compared.

To ensure that the resulting geometrical weld features are representative of the laser scans, a manual inspection is conducted for each specimen. A total of 65 specimens are examined totalling 28 870 laser profiles. For each specimen, the laser scans containing the extreme values of the weld toe radius, angle, and undercut are examined and verified through visual inspection similar to Figures 8.1 to 8.3. Additionally, the weld toe detection, shown in Figure 4.8, for the entire laser scan of each specimen is visually inspected.

The resulting distribution of the geometrical features are shown in Figure 8.5. As mentioned in Section 3.1, all S960 specimens are ground, while roughly half of the S690 specimens are also ground. The effect of the post weld treatment is evident in the increased weld toe radius for S960. The differences in distributions of respectively the weld toe angle, excess weld material, and weld width are suspected to be due to the different welding procedure qualification records for each material. The distributions of undercut are quite similar and can most likely be attributed to the craftsmanship of the welder.

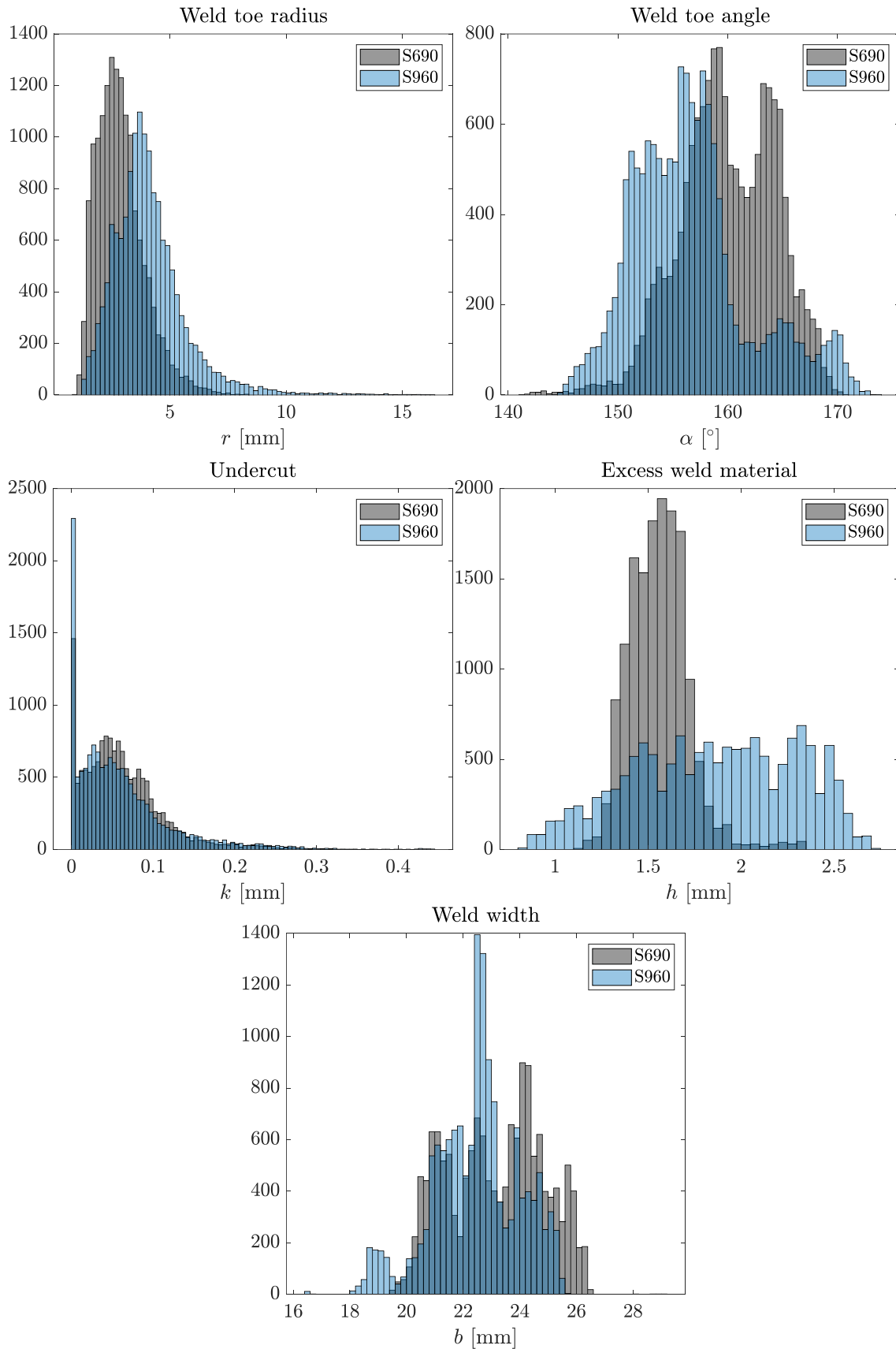


Figure 8.5. Distribution of geometrical weld features for all specimens.

9 Correlation of Strength and Geometry

In this chapter a possible correlation between the geometrical weld features found in Section 8.1 and the best performing fatigue indicator, the maximum principal stress, found in Section 7.1 is investigated. If a significant correlation can be established between the fatigue indicator and one or more of the geometrical features, this may enable the quantification of weld quality based on said features. This can potentially form the basis of a non-destructive testing methodology based on laser scanning of manufactured welds to determine the fatigue strength.

In order to correlate the fatigue lifetime and the geometrical weld features, it is required that the variation for each geometrical feature can be reduced to a single representative quantity for a given specimen, e.g. a single weld toe radius measurement for each specimen. However, it is difficult to define a method with which this reduction to a single representative value may be carried out in practice. Instead, the variation of the geometrical features and the resulting local stress level is investigated.

9.1 Local Variation

When the weld geometry is of good quality, it is anticipated that there will be a connection between the local weld geometry and the local stress level, characterised by a relatively low stress magnification, and vice versa for poor weld quality. An investigation into the influence of the geometrical weld features on the local stress is carried out to validate whether or not this is the case. The local stress is evaluated as the maximum principal stress for each laser profile normalised w.r.t. the nominal stress of the given specimen. The variation of the geometrical weld features along the weld seam, i.e. over the length of the weld, are found using the procedures presented in Section 8.1.

In Figure 9.1 the results of two scanned specimens are shown. The variation in the local stress is shown along with the variations of the weld features. Initially scan No. 70 is inspected. When looking at points of interest (POI) 1 and 2, the expected behaviour between the stress and the weld toe radius r is observed. When the weld toe radius is reduced to a small value, an increase in the local stress is observed. Similarly, when the weld toe radius spikes to a large value, the stress reduces in value. When looking at the

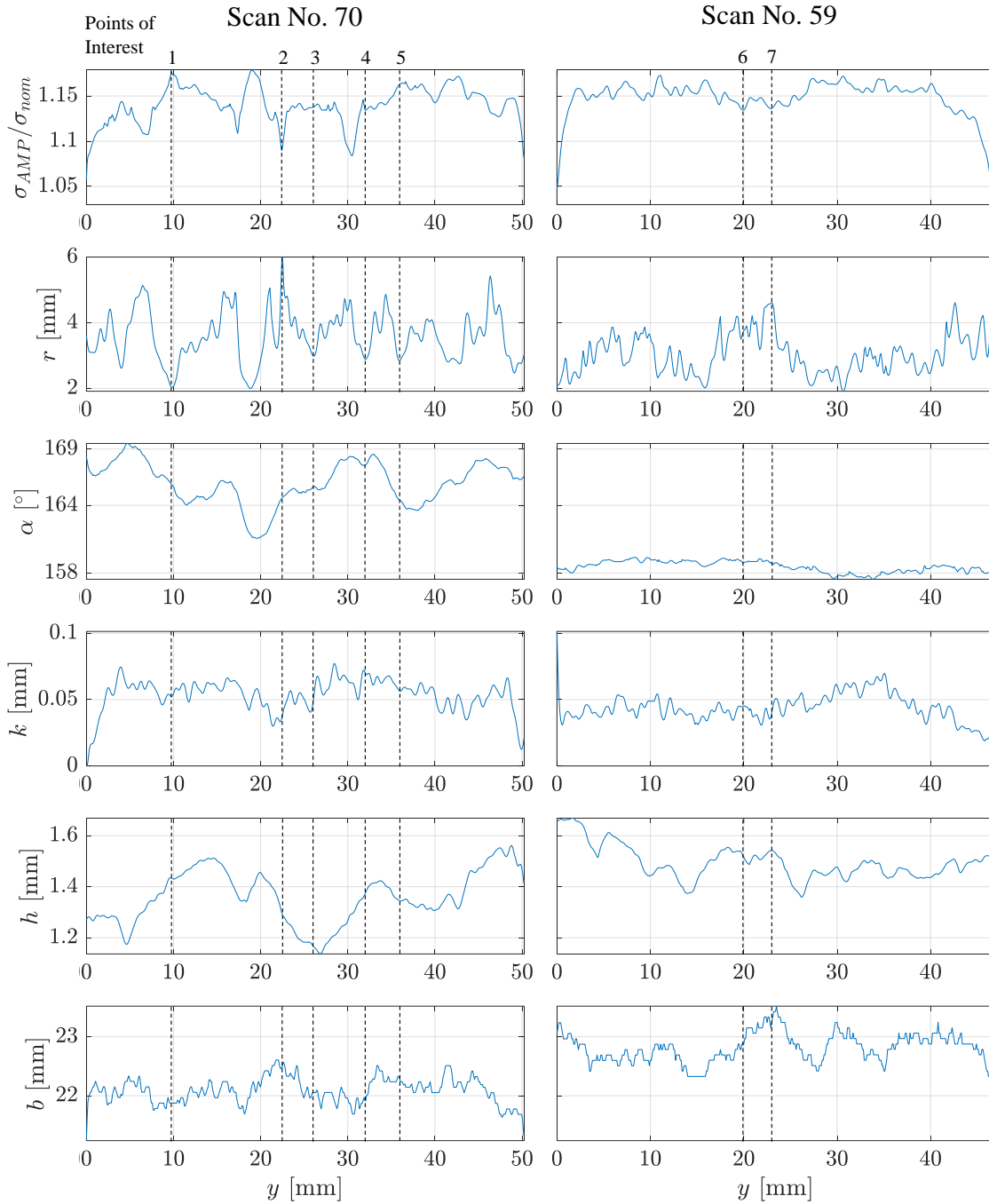


Figure 9.1. Comparison of variations of normalised maximum principal stress and geometrical weld features.

other weld features, their specific impact of the local stress is less clear as they do not show sharply changing values at POI 1 and 2.

For POI 3, 4, and 5 a similar weld toe radius can be observed. However, when inspecting the stress at these three points, POI 5 clearly has a higher value. At POI 5 the weld toe angle α is also seen to be the smallest out of the three. Again the remaining geometrical features are harder to link to direct influences on the local stress due to incoherence.

Lastly, when looking at scan No. 59, a somewhat constant level of local stress is seen

over the length of the weld, however the geometrical features vary considerably. When inspecting POI 6 and 7, the local stress is at the lowest level, however the weld toe radius is different at the two locations. The weld toe angle, undercut, and excess weld material is at similar values at the two POI, with the weld width being slightly larger for POI 7.

Based on the shown variations it has been demonstrated that no single weld feature governs the local stress level. The weld toe radius seems to be most strongly linked to the state of stress in comparison to the other weld features.

9.2 Comparison of Local Stress and Geometrical Features

In this section, the local stress is compared to the local weld features for all specimens investigated. The resulting plots are shown in Figure 9.2, where the difference in colour represents different specimens¹. For all specimens, data points that lie within 2 mm of the edges of the specimens are not included as to reduce the influence of the plane stress state at the edges.

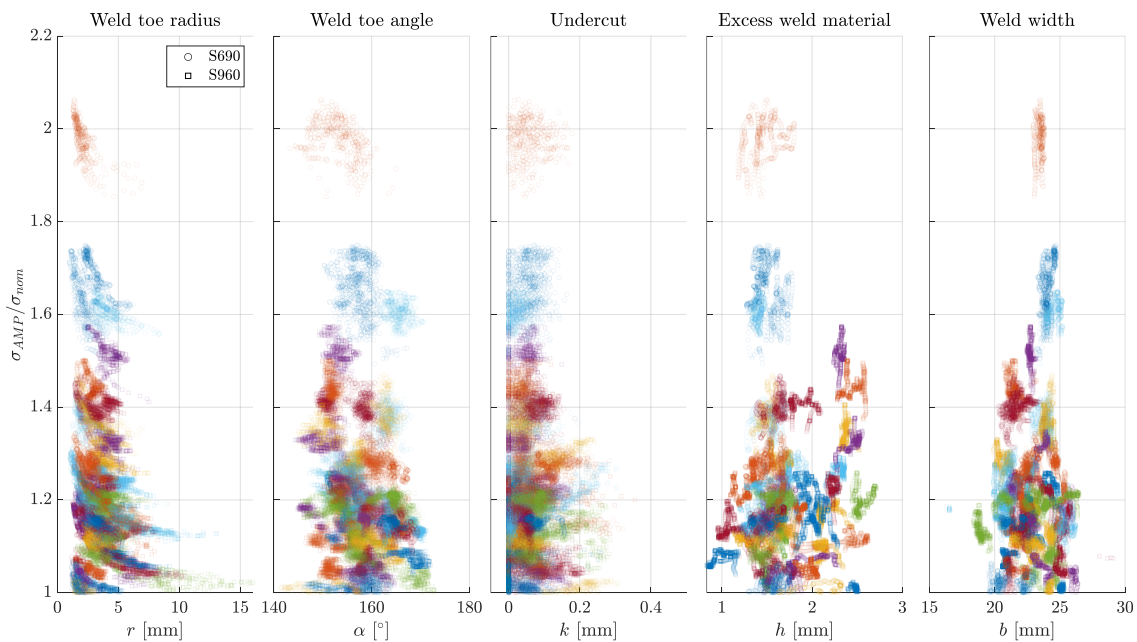


Figure 9.2. Normalised stress along the weld compared to magnitude of local weld geometry features.

When inspecting Figure 9.2, any correlation between the local stress and the geometrical weld features is to be seen as diagonal lines in the plots indicating either improvement or deterioration of the fatigue strength w.r.t. the features. If the data points are pooled together or if they form horizontal or vertical lines no dependence between weld feature and the local stress can be established. The weld toe radius clearly has an effect on the level of the local stress. For decreasing weld toe radius, an exponential increase in the

¹Note, due to the amount of specimen, several colours are repeated for different specimens. However, the data associated with a given specimen is clustered.

local stress is observed, which is in accordance with expected behaviour. This is observed for almost all specimens.

With the weld toe angle the behaviour is less clear as the data points are pooled together in spheres. The dependence of the angle on the stress is unambiguous. For some specimens, an increase in undercut is reflected with an increase in the local stress. However, several specimens also show an indifference in stress level with varying undercut magnitude.

The remaining features of excess weld height and weld width show no clear correlation to the maximum principal stress with maximum values of stress not bearing any relation to diagonal patterns in the features.

Final Remarks

In general, the maximum principal stress correlates consistently with the weld toe radius for the investigated butt welds. The direct influence of the remaining features on the stress can not be derived from Figure 9.2. The fatigue strength, and subsequent fatigue life, is not only dictated by a single point but influenced by its surrounding geometry. This is also implicitly seen in the fatigue indicator study, where uncertainty is reduced by considering a nonlocal volume model.

The exponential relation between the weld toe radius and local stress level, would indicate that by increasing the weld toe radius, such as through post-weld treatment, the local stress level can be reduced, potentially improving the fatigue performance.

10 Conclusion

The purpose of this work was to investigate the influence of including the weld geometry on uncertainty in fatigue assessment and investigate the relationship between geometrical features and fatigue performance. This work considered 33 butt welds in S690 and 32 butt welds in S960, all of which have been loaded in low cycle fatigue. Each specimen has been laser scanned, allowing for the construction of a finite element model that incorporates the actual weld geometry.

Several different fatigue indicators have been investigated to examine their performance in reducing fatigue uncertainty. These indicators have been combined with a nonlocal model to incorporate the stress distribution at the weld. The performance of a fatigue indicator's capability to reduce uncertainty is assessed by applying a Weibull distribution based on the weakest-link theory.

Among the fatigue indicators investigated, a highly stressed volume nonlocal model with the maximum principal stress yielded the lowest uncertainty. It achieved a scatter index of 3.69 for S690 and 3.63 for S960, while the nominal stress approach resulted in higher values of 5.11 and 8.42, respectively. These findings highlight the significant influence of weld geometry on the uncertainty associated with fatigue assessment of butt welded joints.

Investigations into the influence of geometrical features on the fatigue performance have established a relationship between the local stress and weld toe radius, revealing an exponential stress-raising effect as the weld toe radius decreases. However, the influence of other geometrical weld features on the local stress can not be explicitly distinguished, as no clear correlation is observed between the variation of these features and the corresponding local stress.

The findings of this work demonstrate that including weld geometry in fatigue assessment reduces uncertainty and reveals a relationship between weld toe radius and the local stress in butt welded joints.

11 Future Work

In the following, a listing of the immediate areas in which continued research should be carried out is presented.

Expansion of Weld Fatigue Data

The data sets considered in this work was limited to butt welds in high strength steels in low cycle fatigue. In order to quantify the application of the methods, data which expands on the types of weld, steel, and number of cycles should be investigated.

Fatigue Indicators and Nonlocal Models

A limited number of fatigue indicators was investigated in this work. Further investigation of more fatigue indicators is necessary to quantify their applicability, such as the approaches by Findley (1959), Sonsino (1995), Carpinteri et al. (2009), and Susmel (2009, Ch. 3). This can further be expanded to different nonlocal models, such as the stress gradient approach, stress averaging approach, and critical distance approaches (Fricke and Maddox, 2008, Ch. 2.1).

Idealised Weld Geometry

Niederwanger et al. (2020) investigated the reduction of scatter in fatigue for laser scanned cruciform joints compared to idealised weld geometries and found no improvement when considering the laser scanned geometry. However, a study on the uncertainty compared to nominal stress, as conducted in this work and by Hultgren et al. (2022), was not performed. Thus, a comparison between the scanned- and idealised weld geometry as well as the nominal approach, would establish any necessity of modelling the local weld geometry for obtaining reliable fatigue results.

Validation of Code for Geometrical Features

As mentioned in Section 8.2 the implemented method for determining the geometrical weld features has not been validated. As such, the uncertainty of the methods applied is not known. Ideally, both a numerical and experimental investigation of known welds should be examined. A numerical study can both provide insight into the accuracy with which the geometrical features can be determined, but also the effects of applying low pass filtering. An experimental study, in which the measurements of a known physical weld geometry

are made, can be troublesome due to variations in the weld geometry. However, a study comparing manual measurements and digitally obtained measurements, can provide insight into the pros and cons of each method.

Bibliography

- ANSYS, 2023a.** ANSYS. *Mechanical User's Guide*, 2023a.
- ANSYS, 2023b.** ANSYS. *Theory Reference*, 2023b.
- ANSYS, 2023c.** ANSYS. *Discovery SpaceClaim*, 2023c.
- Bruder et al., 2008.** T. Bruder, K. Störzel and J. Baumgartner. *Fatigue assessment of seam welds of automotive components by local stress approaches*. *Materialwissenschaft und Werkstofftechnik*, 39, 2008. <https://doi.org/10.1002/mawe.200800354>.
- Caiza and Ummenhofer, 2011.** Paul D. T. Caiza and Thomas Ummenhofer. *General probability weighted moments for the three-parameter Weibull Distribution and their application in S–N curves modelling*. *International Journal of Fatigue*, 33, 2011. <https://doi.org/10.1016/j.ijfatigue.2011.06.009>.
- Carpinteri et al., 2009.** Andrea Carpinteri, Andrea Spagnoli and Sabrina Vantadori. *Multiaxial fatigue life estimation in welded joints using the critical plane approach*. *International Journal of Fatigue*, 31, 2009. <https://doi.org/10.1016/j.ijfatigue.2008.03.024>.
- DNVGL-OS-C401, 2017.** DNVGL-OS-C401. *Fabrication and testing of offshore structures*. Det Norske Veritas A/S, DNVGL, july 2017 edition, 2017.
- DNVGL-RP-C203, 2016.** DNVGL-RP-C203. *Fatigue design of offshore steel structures*. Det Norske Veritas A/S, DNVGL, april 2016 edition, 2016.
- DS/EN-10025-6, 2019.** DS/EN-10025-6. *Hot rolled products of structural steels – Part 6: Technical delivery conditions for flat products of high yield strength structural steels in the quenched and tempered condition*. DS, København, august 2019 edition, 2019.
- DS/EN-ISO-17637, 2016.** DS/EN-ISO-17637. *Non-destructive testing of welds – Visual testing of fusion-welded joints*. DS, Copenhagen, 3 edition, 2016.
- DS/EN-ISO-5817, 2023.** DS/EN-ISO-5817. *Welding — Fusion-welded joints in steel, nickel, titanium and their alloys (beam welding excluded) — Quality levels for imperfections*. DS, Copenhagen, 4 edition, 2023.
- ECCS, 2018.** ECCS. *Background information on fatigue design rules*. European Convention for Constructional Steelwork, 2 edition, 2018. ISBN 978-92-9147-141-6.

- Findley, 1959.** W. N. Findley. *A Theory for the Effect of Mean Stress on Fatigue of Metals Under Combined Torsion and Axial Load or Bending*. Journal of Engineering for Industry, 81, 1959. <https://doi.org/10.1115/1.4008327>.
- Fricke and Maddox, 2008.** Wolfgang Fricke and S. J. Maddox. *Guideline for the Fatigue Assessment by Notch Stress Analysis for Welded Structures*. International Institute of Welding, 2008.
- Hermansen and Sørensen, 2022.** Ole Hermansen and Rasmus Sørensen. *Investigation of Low Cycle Fatigue Lifetime Assessment in Butt Weld of High Strength Steels*, 2022. [https://projekter.aau.dk/projekter/da/studentthesis/investigation-of-low-cycle-fatigue-lifetime-assessment-in-butt-weld-of-high-strength-steels\(d5db07a8-2fa9-4209-9593-e7ed1d411769\).html](https://projekter.aau.dk/projekter/da/studentthesis/investigation-of-low-cycle-fatigue-lifetime-assessment-in-butt-weld-of-high-strength-steels(d5db07a8-2fa9-4209-9593-e7ed1d411769).html).
- Hobbacher, 2016.** A.F. Hobbacher. *Recommendations for Fatigue Design of Welded Joints and Components*. Springer, 2016. ISBN 978-3-319-23756-5. <https://doi.org/10.1007/978-3-319-23757-2>.
- Hou, 2007.** Chien-Yuan Hou. *Fatigue analysis of welded joints with the aid of real three-dimensional weld toe geometry*. International Journal of Fatigue, 29, 2007. <https://doi.org/10.1016/j.ijfatigue.2006.06.007>.
- Hultgren et al., 2021.** Gustav Hultgren, Leo Myrén, Zuheir Barsoum and Rami Mansour. *Digital Scanning of Welds and Influence of Sampling Resolution on the Predicted Fatigue Performance: Modelling, Experiment and Simulation*. Metals, 822, 2021. <https://doi.org/10.3390/met11050822>.
- Hultgren et al., 2022.** Gustav Hultgren, Rami Mansour and Zuheir Barsoum. *Fatigue strength assessment of welded joints incorporating the variability in local weld geometry using a probabilistic framework*. International Journal of Fatigue, 167, 2022. <https://doi.org/10.1016/j.ijfatigue.2022.107364>.
- Härkegård and Halleraker, 2010.** G. Härkegård and G. Halleraker. *Assessment of methods for prediction of notch and size effects at the fatigue limit based on test data by Böhm and Magin*. International Journal of Fatigue, 32, 2010. <https://doi.org/10.1016/j.ijfatigue.2010.03.011>.
- Kaffenberger and Vormwald, 2012.** Matthias Kaffenberger and Michael Vormwald. *Considering size effects in the notch stress concept for fatigue assessment of welded joints*. Computational Materials Science, 64, 2012. <https://doi.org/10.1016/j.commatsci.2012.02.047>.
- Kuguel, 1960a.** Roberto Kuguel. *The highly stressed volume of the material as a fundamental parameter in the fatigue strength of metal members*. University of Illinois, 1960a. ISSN 0073-5264.

- Kuguel, 1960b.** Roberto Kuguel. *The relation between the theoretical stress concentration factor, K_t , and the fatigue notch factor, K_f , according to the highly stressed volume approach.* University of Illinois, 1960b. ISSN 0073-5264.
- Lang and Lener, 2016.** Robert Lang and Gerhard Lener. *Application and comparison of deterministic and stochastic methods for the evaluation of welded components' fatigue lifetime based on real notch stresses.* International Journal of Fatigue, 93, 2016. <https://doi.org/10.1016/j.ijfatigue.2016.08.023>.
- Lemaitre, 1996.** Jean Lemaitre. *A Course on Damage Mechanics.* Springer, 2nd edition, 1996. ISBN 978-3-642-18255-6.
- Li et al., 2018.** P. Li, D.H. Warner, J.W. Pegues, M.D. Roach, N. Shamsaei and N. Phan d. *Investigation of the mechanisms by which hot isostatic pressing improves the fatigue performance of powder bed fused Ti-6Al-4V.* International Journal of Fatigue, 120, 2018. <https://doi.org/10.1016/j.ijfatigue.2018.10.015>.
- Niederwanger et al., 2020.** A. Niederwanger, D.H. Warner and G. Lener. *The utility of laser scanning welds for improving fatigue assessment.* International Journal of Fatigue, 140, 2020. <https://doi.org/10.1016/j.ijfatigue.2020.105810>.
- Niemi, 2003.** Erkki Niemi. *Structural Hot-Spot Stress Approach to Fatigue Analysis of Welded Components.* International Institute of Welding, Lappeenranta, 2003. ISBN 9789811055676.
- O'Connor and Kleyner, 2012.** Patrick D. T. O'Connor and Andre Kleyner. *Practical Reliability Engineering.* John Wiley & Sons, fifth edition, 2012. ISBN 9780470979822.
- Renken et al., 2021.** Finn Renken, Rüdiger Ulrich Franz von Bock und Polach, Jan Schubnell, Matthias Jung, Markus Oswald, Klemens Rother, Sören Ehlers and Moritz Braun. *An algorithm for statistical evaluation of weld toe geometries using laser triangulation.* International Journal of Fatigue, 149, 2021. <https://doi.org/10.1016/j.ijfatigue.2021.106293>.
- Rinne, 2009.** Horst Rinne. *The Weibull Distribution: A Handbook.* Taylor & Francis, 2009. ISBN 978-1-4200-8743-7.
- Ross, 2004.** Sheldon M. Ross. *Introduction to Probability and Statistics for Engineers and Scientists.* Elsevier Academic Press, 2004. ISBN 0-12-598057-4.
- Schork et al., 2018.** B. Schork, P. Kucharczyk, M. Madia, U. Zerbst, J. Hensel, J. Bernhard, D. Tchuindjang, M. Kaffenberger and M. Oechsner. *The effect of the local and global weld geometry as well as material defects on crack initiation and fatigue strength.* Engineering Fracture Mechanics, 198, 2018. <https://doi.org/10.1016/j.engfracmech.2017.07.001>.

- Schubnell et al., 2019.** Jan Schubnell, Matthias Jung, Chanh Hieu Le, Majid Farajian, Moritz Braun, Sören Ehlers, Wolfgang Fricke, Martin Garcia, Alain Nussbaumer and Jörg Baumgartner. *Influence of the optical measurement technique and evaluation approach on the determination of local weld geometry parameters for different weld types*. *Welding in the World*, 64, 2019. <https://doi.org/10.1007/s40194-019-00830-0>.
- Shojai et al., 2022.** Sulaiman Shojai, Peter Schaumann, Moritz Braun and Sören Ehlers. *Influence of pitting corrosion on the fatigue strength of offshore steel structures based on 3D surface scans*. *International Journal of Fatigue*, 164, 2022. <https://doi.org/10.1016/j.ijfatigue.2022.107128>.
- Sinclair and Dolan, 1953.** G. M. Sinclair and T. J. Dolan. *Effect of Stress Amplitude on Statistical Variability in Fatigue Life of 75S-T6 Aluminum Alloy*. *Trans. ASME*, 75, 1953. <https://doi.org/10.1115/1.4015460>.
- Sonsino, 1995.** C. M. Sonsino. *Multiaxial fatigue of welded joints under inphase and out-of-phase local strains and stresses*. *International Journal of Fatigue*, 17, 1995. [https://doi.org/10.1016/0142-1123\(95\)93051-3](https://doi.org/10.1016/0142-1123(95)93051-3).
- Sonsino and Fischer, 2005.** C. M. Sonsino and G. Fischer. *Local Assessment Concepts for the Structural Durability of Complex Loaded Components*. *Materialwissenschaft und Werkstofftechnik*, 36, 2005. <https://doi.org/10.1002/mawe.200500932>.
- Stenberg et al., 2018.** T. Stenberg, Z. Barsoum, J. Hedlund and J. Josefsson. *Development of a computational fatigue model for evaluation of weld quality*. *Welding in the World*, 63, 2018. <https://doi.org/10.1007/s40194-019-00777-2>.
- Stenberg et al., 2012.** Thomas Stenberg, Eric Lindgren and Zuheir Barsoum. *Development of an algorithm for quality inspection of welded structures*. *Journal of Engineering Manufacture*, 226, 2012. <https://doi.org/10.1177/0954405412439138>.
- Stephens et al., 2001.** Ralph I. Stephens, Ali Fatemi, Robert. R Stephens and Henry O. Fuchs. *Metal Fatigue in Engineering*. John Wiley & Sons, Inc., New York, 2 edition, 2001. ISBN 0-471-51059-9.
- Susmel, 2009.** Luca Susmel. *Multiaxial notch fatigue*. Woodhead Publishing in Materials, 2009. ISBN 978-1-84569-582-8.
- Wallin, 1984.** Kim Wallin. *The scatter in K_{IC} -results*. *Engineering Fracture Mechanics*, 19, 1984. [https://doi.org/10.1016/0013-7944\(84\)90153-X](https://doi.org/10.1016/0013-7944(84)90153-X).
- Weibull, 1951.** Waloddi Weibull. *A Statistical Distribution Function of Wide Applicability*. *Journal of Applied Mechanics*, 1951. <https://doi.org/10.1115/1.4010337>.
- Weibull, 1961.** Waloddi Weibull. *Fatigue Testing and Analysis of Results*. Pergamon Press, 1961. ISBN 978-0-08-009397-0. <https://doi.org/10.1016/C2013-0-01661-1>.

Wenglor, 2023. Wenglor. *MLWL153*. https://www.wenglor.com/medias/__secure__?mediaPK=8799866322974&attachment=true, 2023.

Zhang and Maddox, 2009. Yan-Hui Zhang and Stephen J. Maddox. *Fatigue life prediction for toe ground welded joints*. *International Journal of Fatigue*, 31, 2009. <https://doi.org/10.1016/j.ijfatigue.2009.01.003>.

